



University of Kerbala
College of Science
Department of Physics

**Fabrication of Glucose Biosensor Using ZnO
Nanostructure Coated By Silver Nanoparticles**

A Thesis

Submitted to the Council of the College of Science, University of Kerbala, in
Partial Fulfillment of the Requirements for the Degree of Master of Science in
Physics

By

Asaad Sabbar Yasir

Supervised by

Prof. Dr. Noor J. Ridha

2022 A.D.

1444 A.H.

بِسْمِ اللَّهِ الرَّحْمَنِ الرَّحِيمِ

وَنُنزِّلُ مِنَ الْقُرْآنِ مَا هُوَ شِفَاءٌ وَرَحْمَةٌ
لِّلْمُؤْمِنِينَ وَلَا يَزِيدُ الظَّالِمِينَ إِلَّا خَسَارًا

صدق الله العلي العظيم

Supervisors Certification

We certify that the preparation of this thesis, entitled "**Fabrication of Glucose Biosensor Using ZnO Nanostructure Coated by Silver Nanoparticles**" was made under our supervision by (Asaad Sabbar Yasir) at the Department of physics, College of the Science, University of Kerbala as partial fulfillment of the requirements for the degree of Master in Physics Science.

Signature:



Name: Dr. Noor J. Ridha

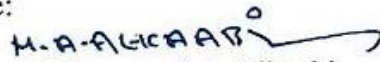
Title: Professor

Address: Department of physics, College of Sciences, University of Kerbala

Date: 4 / 12 / 2022

In view of the available recommendations, I forward this thesis for debate by the examination committee.

Signature:



Name: Dr. Mohammed A. Alkaabi

Title: Assistant Professor

Head of the Department of Physics, College of Science

Date: 4 / 12 / 2022

Examination Committee Certification

We certify that we have read this thesis, entitled " **Fabrication of Glucose Biosensor Using ZnO Nanostructure Coated by Silver Nanoparticles** " and as an examining committee, examined the student " **Asaad Sabbar Yasir** " on its contents, and that in our opinion it is adequate for the partial fulfillment of the requirements for the degree of Master of Science in Physics.


Signature 

Name: Dr. Rajaa A. Madloul

Title: Professor

Address: Department of physics, College of Sciences, University of Kerbala (Chairman)

Date: 29/12/2022

Signature: 


Name: Dr. Aref Saleh Baron

Title: Professor

Address: Department of physics, College of Sciences, University of Kufaa

(Member)

Date: 29/12/2022

Signature: 


Name: Dr. Noor J. Ridha

Title: Professor

Address: Department of physics, College of Sciences, University of Kerbala

(Supervisor)

Date: 29/12/2022


Signature: 

Name: Dr. Jasem Hanoon Hashim Al-Awadi

Title: Assistant Professor

Dean of the College of Sciences, University of Kerbala

Date: 29/12/2022

Signature: 

Name: Dr. Nibras Mousa Umran

Title: Assistant Professor

Address: Department of physics, College of Sciences, University of Kerbala

(Member)

Date: 29/12/2022

Dedication

To...

My Father (soul) and My Mother...

My Brothers, Sisters and Everyone who supported me...

My Sons and daughters Marwa, Zainab, Noor Al-
Wilaya, Mohammed...

Acknowledgments

First and foremost I want to thank my supervisor Dr Noor J. Ridha. She has been supportive since the days I began working. I deeply appreciate all her dedication of time and ideas. The joyful and enthusiastic attitude she has for our research was contagious and inspirational for me, even during the hard times in my M.Sc. pursuit.

I would like to thank the University of Karbala - College of science for their support. Also, I am deeply thankful to all members of the physics department and all my colleagues for their help in supporting me to accomplish my dissertation.

Great thanks to my family especially my mother, my brothers, sisters, my sons, and daughters for their patience and support and also to all my friends and to all the lovely people who helped me, directly or indirectly to complete this work.

ASAAD

Abstract

Research sciences and medical societies have recently shifted into using cost-effective biosensors to test food & water contaminants, control human biologic processes, assess precise health diagnosis, and more. Researchers and medical practitioners need safe and cheaper means of performing their research, ensuring public safety, and delivering customized health options to patients. One such solution can be easily carried out by using biosensors. The dip coating system was developed to prepare the thin film of ZnO were successfully deposited on indium tin oxide (ITO) substrates. The effects of the dipping cycles were investigated. Dipping processes were applied several times one up to three at concentrations of 0.1 M zinc acetate to obtain homogeneous thin films. In this work, Ag NPs coated ZnO has been prepared using the hydrothermal method to be used as a glucose biosensor. The preparation method includes three steps, seed, growth and coating. The first step was to coat the substrate with a seed layer. The second step was to grow ZnO NRs with concentration 0.050 M of zinc nitrate. Finally, 0.001 M of AgNO₃ to obtain Ag NPs were coated on the ZnO nanorods. Investigations structural, compositional, surface morphologies, optical, electrical resistance, and cyclic voltammetry properties were conducted to determine the effects of the preparation condition and coating the ZnO NRs by Ag NPs on these properties. As well as, the catalytic properties of glucose oxidase (GOx) and the functionality of the glucose sensor were taking place. The XRD results showed that the prepared samples have a good crystallinity and a high purity. Additionally, the structure of ZnO is hexagonal wurtzite. The crystal size was in the nanoscale size with the range of 20-50 nm. As for the examination by FESEM, it was found that homogeneous layers formed when increasing the dipping times of the prepared thin films. The UV-Vis spectroscopy and electrical properties showed that the prepared films were transparent with reduced energy gap and surface resistance by increasing the thickness due to the doping with Ag NPs. The results show that the cyclic voltammetry properties were improved by coating the ZnO NRs by 0.001 M of Ag NPs for sample S₉. The scanning rate was 50 mV s⁻¹ and the voltage range was -

1.00 to 1.00 V, and the concentration of glucose was from 0 – 500 μM . The investigations proved that the sensitivity of the sensor was about $350.1 \mu\text{AmM}^{-1}\text{cm}^{-2}$, the limit of detection (LOD) was $38.1 \mu\text{M}$ and the response time was 7 sec. Nevertheless, there is a linear increment of current toward a varied range of glucose concentrations.

Table of contents

Chapter: 1

1.1 Introduction	2
1.1.1 Synthesis of nanosubstancec and classifications	3
1.1.2 Background of Sensors and Nanomaterials	4
1.1.3 Blood sugar	5
1.2 Literature Review	6
1.3 Thesis objectives	11
1.4 Organization of the thesis.....	11

Chapter: 2

2.1 Introduction	13
2.2 Fundamental properties of ZnO	13
2.3 Crystal structure and chemical binding.....	14
2.3.1 ZnO structure	14
2.3.2 Electrical properties	15
2.3.3 Optical properties	16
2.4 Ag doping ZnO for enhancement sensing performance	17
2.5 Preparation methods	18
2.5.1 Dip coating method.....	20
2.6 Sensing applications depend on ZnO and transition metals doped ZnO nanostructures	21
2.6.1 Sensors and their applications depend on ZnO NRs.....	22
2.6.2 Biosensors and their applications based on ZnO NRs	23
2.7 Glucose Biosensor	24
2.7.1 Components of biosensors	26

Chapter: 3

3.1 Introduction	29
3.2 Manufactured devices.....	29
3.2.1 Dip coating design and fabrication	29

3.2.2 Manufacturing the muffle furnace	31
3.3 Materials and methods.....	32
3.4 Preparation method.....	32
3.4.1 Preparing seed layer – Cleaning methods	32
3.4.2 Preparation and deposition of seed solution	33
3.4.3 Synthesis of ZnO NRs.....	34
3.4.4 Coated ZnO NRs by Ag NPs	35
3.5 Preparation glucose biosensor	35
3.6 Characterization methods	35
3.6.1 X-ray diffraction.....	35
3.6.2 Field emission scanning electron microscope (FESEM)	37
3.6.3 UV-visible spectroscopy	38
3.6.4 I-V properties Four-point probe (FPP) method single configuration technique	39
3.6.5 Electrochemical measurements.....	40

Chapter: 4

4.1 Structural properties	45
4.1.1 ZnO Seed layer.....	45
4.1.2 ZnO NRs	46
4.1.3 ZnO NRs coated with Ag NPs	48
4.2 Morphological properties	52
4.2.1 ZnO Seed layer.....	52
4.2.2 ZnO NRs	57
4.2.3 ZnO NRs coated with Ag NPg.....	62
4.3 Optical properties	67
4.3.1 ZnO Seed layer.....	67
4.3.2 ZnO NRs	69
4.3.3 ZnO NRs coated with Ag NPs	71
4.4 Electrical properties.....	73
4.4.1 ZnO Seed laye	73

4.4.2 ZnO NRs	75
4.4.3 ZnO NRs coated with Ag NPs	76
4.5 Cyclic voltammetry properties	78
4.5.1 ZnO NRs	78
4.5.2 ZnO NRs coated with Ag NPs	81
4.6 Conclusion	86
4.7 Future work	87
References.....	88

List of tables

Chapter: 3

Table 3-1. Samples ID used in this thesis.	43
---	----

Chapter: 4

Table 4-1. Illustrate all parameters calculated from XRD data for samples S ₁ , S ₂ , and S ₃	46
---	----

Table 4-2. Illustrate all parameters calculated from XRD data for samples S ₄ , S ₅ , and S ₆	48
---	----

Table 4-3. Illustrate all parameters calculated from XRD data for sample S ₇ , S ₈ and S ₉	51
--	----

Table 4-4. Four Point Probe Method sheet resistance for samples S ₁ , S ₂ , and S ₃ with varying dipping cycles	74
---	----

Table 4-5. Four point probe method sheet resistance for samples S ₄ , S ₅ , and S ₆ with varying dipping cycles.	76
--	----

Table 4-6. Comparison of FPP method sheet resistance for ZnO NRs samples of varying dipping cycles and coated by Ag NPs.....	77
--	----

Table 4-7. Varying in data obtained from cyclic voltammetry data for samples S ₄ , S ₅ , and S ₆	81
--	----

Table 4-8 varying in data obtained from cyclic voltammetry data for S ₄ , S ₅ , S ₆ , S ₇ , S ₈ , and S ₉	85
--	----

List of Figures

Chapter: 1

Figure 1-1 Approaches Top – down and bottom – up for synthesis nanomaterials [6].	4
Figure 1-2. Sensor system [9].....	5
Figure 1-3. Blood sugar, the normal and excessive the amount [15].....	6

Chapter: 2

Figure 2-1. ZnO structures a) rocksalt b) zinc blend c) wurtzite [42]. .	14
Figure 2-2. Biosensor elements and mechanisem[96].	27

Chapter: 3

Figure 3-1. Schematic diagram of designed dip coating system.....	30
Figure 3-2. a) The developed sample holder, b) copper nut and T8 guide lead screw 300 mm.	31
Figure 3-3. Manufacturing muffle furnace.....	32
Figure 3-4. Schematic diagram of the sample preparation procedure. ..	34
Figure 3-5. Four-point probe method for rectangular sample [116].	40
Figure 3-6. Cyclic voltammetry system and mechanism of working electrode.....	42

Chapter: 4

Figure 4-1. XRD patterns and slandered JCPDS data.....	45
Figure 4-2. XRD patterns and slandered JCPDS data for S ₄ , S ₅ , and S ₆	47
Figure 4-3. XRD diffraction pattern for S ₇ , S ₈ , and S ₉ compared with JPCDS cards.	50

Figure 4-4. ZnO and Ag ratio in the XRD analysis depending on Ag - JCPDS 01-072-0607 and ZnO - JCPDS 96-901-1663 for samples S ₇ , S ₈ , and S ₉	52
Figure 4-5a. Cross-section of sample S ₁	53
Figure 4-5b. Cross-section of sample S ₂	53
Figure 4-5c. Cross-section of sample S ₃	54
Figure 4-5d. The surface morphology of samples S ₁	55
Figure 4-5e. The surface morphology of samples S ₂	55
Figure 4-5f. The surface morphology of samples S ₃	56
Figure 4-5g, h, i. Size distribution of particles diameter of samples S ₁ , S ₂ , and S ₃ respectively.....	56
Figure 4-6. Mapping and EDS composition of samples S ₄ , S ₅ , and S ₆ ..	57
Figure 4-7a. The cross section of sample S ₄	58
Figure 4-7b. The cross section of sample S ₅	58
Figure 4-7c. The cross section of sample S ₆	59
Figure 4-7d. Top view of homogenous distribution of sample S ₄	59
Figure 4-7e. Top view of homogenous distribution of sample S ₅	60
Figure 4-7f. Top view of homogenous distribution of sample S ₆	60
Figure 4-7g, h, i. The size distribution of particles diameter of..... S ₄ , S ₅ , S ₆ respectively.....	61
Figure 4-8. Mapping and EDS composition of samples S ₄ , S ₅ , and S ₆ ..	61
Figure 4-9 a. The cross-section of sample S ₇	62
Figure 4-9 b. The cross-section of sample S ₈	62
Figure 4-9 c. The cross-section of sample S ₉	63
Figure 4-9d. Top view of homogenous distribution of sample S ₇	64

Figure 4-9e. Top view of homogenous distribution of sample S ₈	64
Figure 4-9f. Top view of homogenous distribution of sample S ₉	65
Figure 4-9g, h, i. The size distribution of nanorods diameter of sample S ₇ , S ₈ and S ₉ respectively.....	65
Figure 4-10. Mapping, and EDS composition for ZnO NRs coated by Ag NPs for samples S ₇ , S ₈ and S ₉	66
Figure 4-11 Photographs of transparent thin films seed layer	67
S ₁ , S ₂ , and S ₃	67
Figure 4-12. Energy gap of samples a) S ₁ , b) S ₂ , c) and S ₃	68
Figure 4-13. UV – Vis characterization of the prepared ZnO thin films for	69
S ₁ , S ₂ , and S ₃	69
Figure 4-14. Photographs of transparent ZnO NRs thin films	69
S ₄ , S ₅ and S ₆	69
Figure 4-15. UV – Vis characterization of the prepared ZnO NRs thin films for.....	70
S ₄ , S ₅ , and S ₆	70
Figure 4-16. Energy gap for S ₄ , S ₅ , and S ₆	71
Figure 4-17. Photographs of transparent thin films ZnO NRs coated by Ag NPs for S ₇ , S ₈ , and S ₉	71
Figure 4-18. Optical Properties for ZnO NRs coated by Ag NPs for samples S ₇ , S ₈ , and S ₉	72
Figure 4-19. Energy gap for ZnO NRs coated by Ag NPs for samples S ₇ , S ₈ , and S ₉	73
Figure 4-20. I-V characterization for S ₁ , S ₂ , and S ₃	74
Figure 4-21. I-V characterization of S ₄ , S ₅ , and S ₆	75

Figure 4-22. I-V characterization for S ₇ , S ₈ , and S ₉	77
Figure 4-23a. Cyclic voltammograms of the ZnO NRs coated by Ag NPs in the presence of glucose of 0 mM- 5 mM in PBS with a scan rate of 50 mV s ⁻¹ of sample S ₄	79
Figure 4-23b. Cyclic voltammograms of the ZnO NRs coated by Ag NPs in the presence of glucose of 0 mM- 5 mM in PBS with a scan rate of 50 mV s ⁻¹ of sample S ₅	79
Figure 4-23c. Cyclic voltammograms of the ZnO NRs coated by Ag NPs in the presence of glucose of 0 mM- 5 mM in PBS with a scan rate of 50 mV s ⁻¹ of sample S ₆	80
Figure 4-24. Increments of current as a function of glucose concentration for samples S ₄ , S ₅ , and S ₆	80
Figure 4-25a. Cyclic voltammograms of the ZnO NRs coated by Ag NPs in the presence of glucose in 0 mM- 5 mM in PBS with a scan rate of 50 mV s ⁻¹ of sample S ₇	82
Figure 4-25b. Cyclic voltammograms of the ZnO NRs coated by Ag NPs in the presence of glucose of 0 mM- 5 mM in PBS with a scan rate of 50 mV s ⁻¹ of sample S ₈	83
Figure 4-25c. Cyclic voltammograms of the ZnO NRs coated by Ag NPs in the presence of glucose of 0 μM- 500 μM PBS with a scan rate of 50 mV s ⁻¹ of sample S ₉	83
Figure 4-26. Increments of current as a function of glucose concentration of samples S ₇ , S ₈ , and S ₉	84

List of abbreviations

Symbol	Description
α	absorption coefficient cm^{-1}
A	absorbance
Al	aluminum
AR	aspect ratio
ALD	atomic layer deposition
BSE	back-scattered electrons
E_o	cell potential under standard conditions
E	cell potential
β -cells	cells in the pancreas
Cal Tech	California institute of technology
CL	cathodoluminescence
D	crystal size nm
CBD	chemical bath deposition
CVD	chemical vapor deposition
CS	chitosan
CB	conduction band
CGM	continuous glucose monitoring
Cu	copper
DM	diabetes mellitus
$\beta_d = \frac{1}{2}$	direct band gap semiconductors value
DI water	die ionized water

CuO/ZnO-DSDSHNM	dumbbell-shaped double-shelled hollow nanoporous CuO/ZnO microstructures
DET	direct electron transfer
EMF	electromotive force V
k	extinction coefficient
EDS	energy-dispersive X-ray spectroscopy
EGFETs	extended gate field effect transistor
FESEM	field emission scanning electron microscope
FPP	four- point probe
e	fundamental charge of electrons
FWHM	full width at half maximum radians
GCE	glassy carbon electrode
GOx	glucose oxidase
GCSP	glucose oxidase on chitosan submicron particles
Au	gold
g	gravitational constant 9.81 m s^{-2}
HMT	hexamethylenetetramine
HNRs	hybrid nanorods
R	ideal gas constant
ITO	indium tin oxide
IoT	internet of things
Φ_i	incident radiant flux
i	intensity of light passing through the sample
$h\nu$	incident photon energy
i_o	intensity of light before passing through the sample
i/i_o	transmittance
I %	the degree of inhibition

I_0	the glucose response in the absence of the inhibitor
I	the glucose response in the presence of the inhibitor
$^{\circ}\text{K}$	$^{\circ}$ kelvin
Lac	laccase
LED	light emitting diode
LOD	limit of detection mM or μM
Mg	magnesium
MeV	mega electron volt
MOCVD	metalorganic CVD
μm	micrometer
MWCNT	multiwall carbon nanotube
SWCNTs	single-wall carbon nanotubes
μM	micromole
mV	millivolt
MBE	molecular beam epitaxy
MO	metal oxide
nm	nanometer
n	number of electrons transferred during the reaction
Nps	nanoparticles
NRs	nanorods
NIR	near infrared
1D	one-dimension
[Ox]	oxidized concentration
PBS	phosphate buffered saline
PECVD	plasma enhanced CVD
h	Plank's constant
ρ	Resistivity ($\Omega\cdot\text{m}$)
[Red]	reduced concentration

rGO	reduced graphene oxide
R_s	resistance
Φ_t	radiant flux
ZnO-g-Ru-C ₃ N ₄	ruthenium-doped carbon nitride modified with a zinc oxide rod
s_s	sample size
SE	secondary electrons
σ	standard error of the regression line
R_{SS}	sheet resistance
Ag	silver
AgNO ₃	silver nitrate
γ	surface tension of liquid
TPs	tetrapods
TM	transition metals
t	thickness of the thin film nm
3D	three-dimension
TCO	transparent conducting oxide
2D	two-dimension
T1DM	type 1 diabetes mellitus
T2DM	type 2 diabetes mellitus
UV	ultraviolet
VB	valence band
η	viscosity of the liquid kg m ⁻¹ s ⁻¹ or Pa.s ⁻¹
λ	wavelength °A
XRD	X-ray diffraction
YSI	Y yellow spring instrument company
0D	zero-dimension
ZnO	zinc oxide

Chapter 1:

Introduction and Literature Review

1.1 Introduction

Nanotechnology is the synthesis, characterization and application of materials that are their size in the nanoscales regime. Nanomaterials exhibited novel properties that differ dramatically from those of atoms or bulk materials [1]. Furthermore, when materials reach the nanoscale regime, a high surface area to volume ratio will be displayed. Therefore, surface reaction with the neighboring will be increased, making nanomaterials great applicants for a wide range of sensing applications. As a result, nanomaterials have provided the opportunity for new strategies and technologies [2].

Richard Feynman emphasized the importance of nanotechnology in his talk at an international event of the American Physical Society at California institute of technology (Cal Tech) 1959 entitled "There is plenty of room at the bottom" [3] . Nanotechnology is now acknowledged as a breakthrough subject of science and technology, with applications in a variety of fields, inclusive of environmental, medicinal, and biomedical applications. Furthermore, the novel applications of nanomaterials exhibited very fast reactions, cheap, extended life time, ease of use for untrained persons, and high efficiency for the device. As well as, new ways for the detection and treatment of diseases, comprehensive environmental monitoring, and energy-saving alternatives were developed to provide a better lifestyle. In this context, the growth of new technologies for synthesizing nanomaterials has cleared the approach for the creation of novel nanostructure-based electronics which becomes a feature of our contemporary world. The ability to generate nanostructured materials with modified structure, size, and shape, as well as improved properties, opens up a lot of possibilities for building nanotechnology-based technologies [4].

1.1.1 Synthesis of nanosubstance and classifications

The capability to control the morphologies of the surface and the structure of nanomaterials increasingly idealized semiconductor structures like quantum wells as a result, wires, and dots. As well, the quantum mechanics models of a particle in a box indicate that electron states of these nanostructures have a radically different densities. Nanostructures can be divided into zero dimension (0D), one dimension (1D), two dimension (2D), and three dimension (3D) based on their elementary dimensions (X, Y, and Z) in space (3D). 0D nanostructures are nanoparticles (NPs) or quantum dots, (1D) are nanorods (NRs), nanowires (NWs), nanofibres, nanobelts, and nanotubes (NTs), 2D nanomaterials are nanosheets, nanowalls, and nanoplates, and 3D nanomaterials are nanoflowers and other complex structures like nanotetrapods [5].

The regulation of particle size is a major focus of research in the nanotechnology domains. In order to control the morphology and composition of nanomaterials, several preparation methods could be followed. These methods could be classified generally into two methods; top _ down and bottom _ up methods. The bottom-up approach is a technique for creating nanomaterials from atoms or molecules. The top - down methodology, is a method of breaking down larger materials into smaller particles. These two approaches are depicted in a schematic diagram, as shown in figure 1-1 [6].

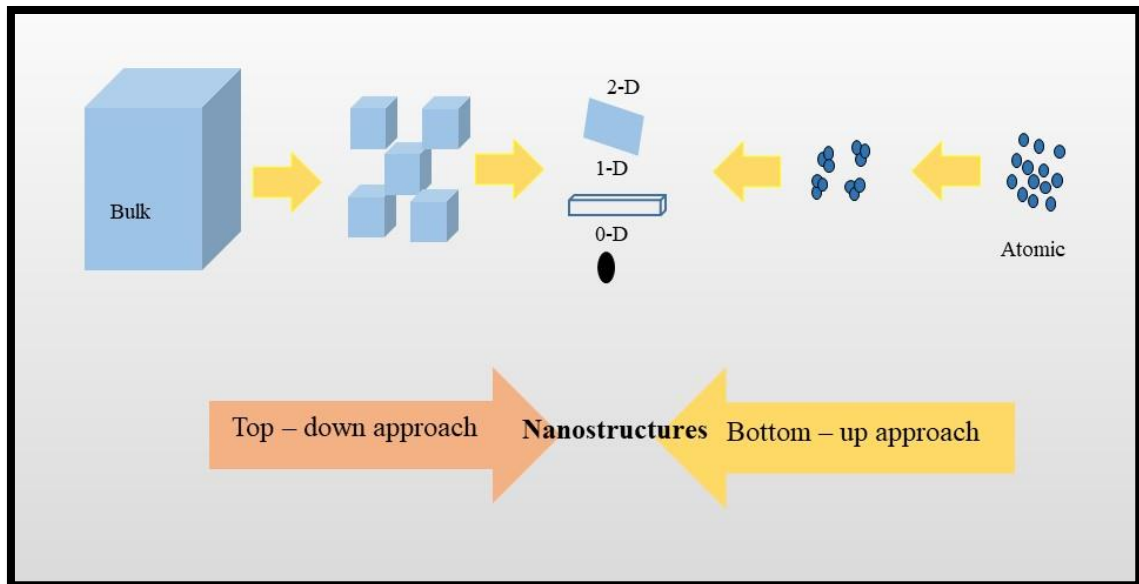


Figure 1-1 Approaches Top – down and bottom – up for synthesis nanomaterials [6].

1.1.2 Background of Sensors and Nanomaterials

The sensor is apparatus which detects the changes in physical circumstances, chemical amounts, or biological specimen and responds with a calculable signal to a specific input [7]. As well as, the physical packaging and external connections of a sensing element make up the physical configuration of a sensor [8]. The sensor system's schematic diagram is displayed in figure 1-2 [9].

Chapter One: Introduction and Literature Review

Nanostructured materials have several attractive properties for sensing applications. The capability of modifying the size, structure, and behavior of semiconductor nanostructures belongs to quantum confinement effects. Moreover, nanostructured substances have exceptional electrical, optical, thermal, catalytic, and mechanical capabilities, allowing for the construction of nanomaterial-based sensors and the development of innovative sensing systems [10]. By changing the materials to nanosize regime, the ratio of surface area to volume was increased, which in turn boosted the interactions amidst the materials and their surrounds. This phenomenon resulted in the sensor's higher sensitivity, improved limit of detection (LOD), rapid responses, the ability to measure low concentrations of samples with cheaper cost, ease of use for untrained users, high efficiency, and a low power consumption [11].

1.1.3 Blood sugar

Diabetes mellitus (DM) refers to a cluster of metabolic diseases characterized by chronic hyperglycemia. The cause is either a disruption in

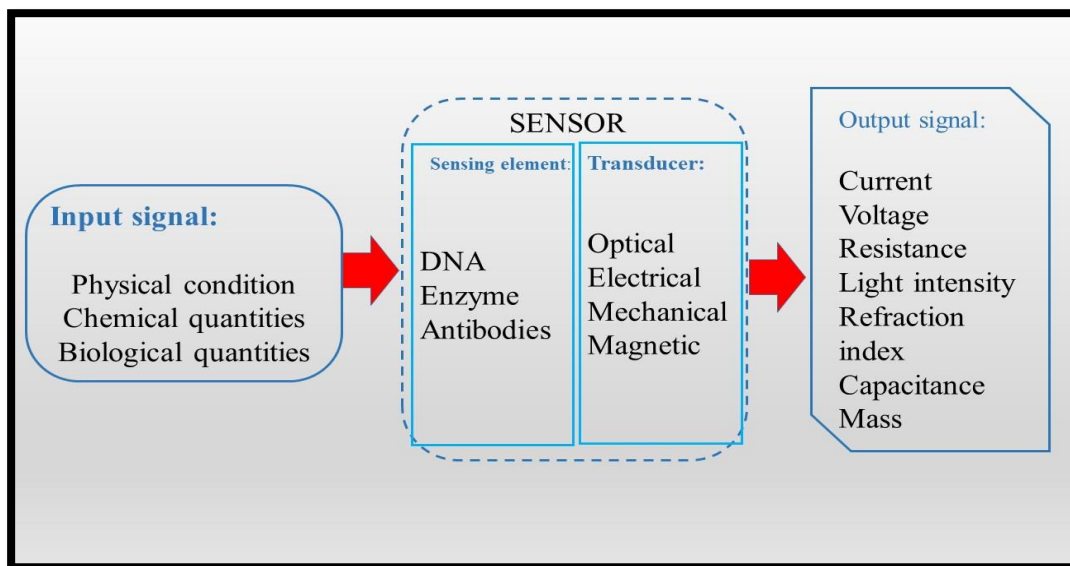


Figure 1-2. Sensor system [9].

insulin secretion or disruption in insulin effect or both in most cases [12]. One of the most common autoimmune diseases is type 1 diabetes mellitus (T1DM) which is caused by the loss of β -cells in the pancreas. T1DM can strike at any

Chapter One: Introduction and Literature Review

age, but it is more common in adolescents, with a peak onset around puberty. T1DM is equally common in both sexes during childhood, while men are more probable to develop the condition in early adulthood [13]. Although it was once most frequent among Europeans, it is now spreading to other ethnic groups. T1DM accounts for 5-10% of all diabetes patients. In addition, T1DM is one of the public autoimmune diseases in childhood. Nevertheless, type 2 diabetes mellitus (T2DM) is rising all over the world, and it is increasing by increasing obesity. Complications of T2DM are one of the primary causes of morbidity and mortality. Long-term issues can be avoided if drugs are taken as prescribed and a healthy lifestyle (i.e., diet and physical activity) is maintained [14]. Figure 1-3 illustrates the blood sugar, the normal and excessive the amount.

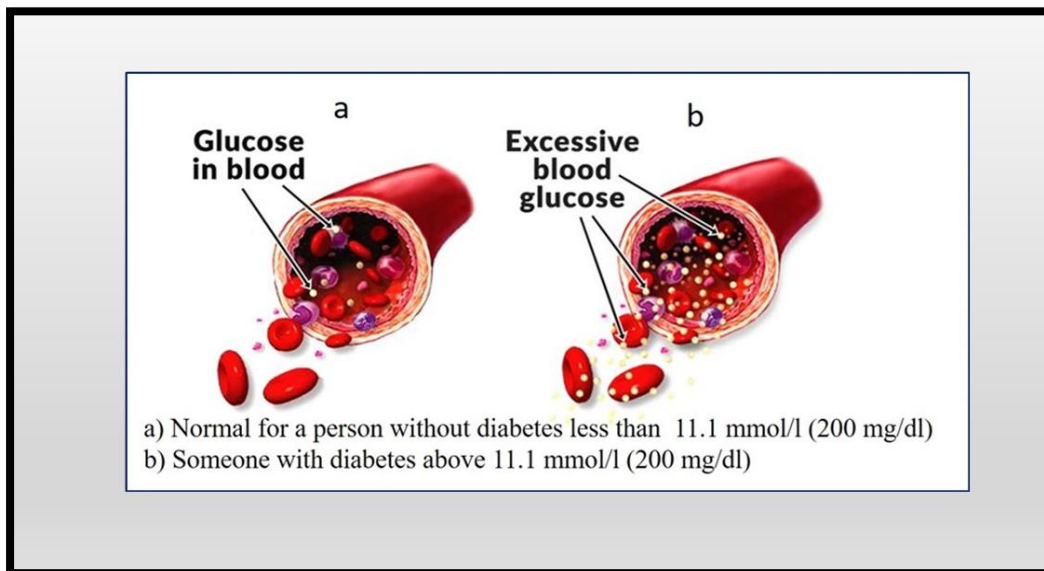


Figure 1-3. Blood sugar, the normal and excessive the amount [15]

1.2 Literature Review

Since glucose biosensors are the most studied type of biosensor, a variety of designs have been developed. However, because of the difficulty of attaching an electronic device directly to a biological system, thus transforming the biological signal into a readily processed electrical signal is a crucial domain. Therefore, several sensing concepts and devices have been created over the last few decades. Biosensors have been extensively explored and used in a variety

Chapter One: Introduction and Literature Review

of applications since then, ranging from public health and environmental monitoring to homeland security and food safety [16]. As a result, a many scientific research have gone into designing biosensors for diverse applications. Glucose biosensors have been extensively explored and created using a variety of ways. Here are some of the most noteworthy studies from the last ten years.

In 2012 R. Ahmad, et al [17] reported that ZnO NRs were prepared directly on the Si/Ag electrode by hydrothermal method. The preparation was done using Zinc nitrate hexahydrate ($\text{Zn}(\text{NO}_3)_2 \cdot 6\text{H}_2\text{O}$), hexamethylenetetramine (HMT) and phosphate buffered saline (PBS, pH 7.4) at 90 °C. They used several periods 2, 4, 6, 8, 10, and 12 hours to obtain different lengths of zinc oxide rods to be used as amperometric glucose biosensors. The glucose biosensor in particular, with an aspect ratio (AR) = 60 has a wide linear range of 0.01-23.0 mM and a maximum sensitivity of 110.76 $\mu\text{A}/\text{mM cm}^2$. Extremely quick response time (<1 s) and detection limit 0.1 μM .

In 2012 X. Feng, et al [18] reported the preparation of Ag nanoparticles were used to create Ag-ZnO core-shell heterostructured nanomaterials for the first time, enabling the development of a brand-new hydrogen peroxide biosensor. The Ag-ZnO-2 biosensor had the best electrochemical properties, the strongest redox peak currents, and the smallest E_p of about 40 mV, according to electrochemical measurements, which also showed that the electrochemical properties of the Ag-ZnO-x-based biosensors were related to the Ag nanoparticle content. Additionally, the Ag-ZnO-2-based biosensor demonstrated remarkable electrocatalytic capabilities, including a linear range 2-540 μM , sensitivity 83 $\text{mA}/\text{cm}^2 \text{mM}$, LOD 0.18 μM , and good stability and repeatability.

In 2013 A. Umar, et al [19] reported that by using a simple solution technique, well-crystalline ZnO nanoflowers were produced. In order to create a highly sensitive non-enzymatic glucose sensor, ZnO nanoflowers were also tested as an effective electron mediator. This sensor showed a high sensitivity

Chapter One: Introduction and Literature Review

of $411 \mu\text{A M}^{-1} \text{cm}^{-2}$, a detection limit of 1.25 mM, and a short response time of 10.0 s. The investigations that were presented demonstrated that non-enzymatic ZnO nanoparticles can be used as a very sensitive glucose sensor.

In 2014 Y. Liu, et al [20] reported that Zinc-nickel hydroxycarbonate composites were thermally annealed to create mesoporous ZnO-NiO structures. The resulting designs exhibit a high surface area and a potent synergy between the ZnO and NiO nanoparticles since they are demonstrated to be assembled by many mesoporous nanosheets. An electrode made from the material produced by annealing at $400 \text{ }^\circ\text{C}$ responds to glucose over a broad concentration range from 0.5 M to 6.4 mM, with a detection limit as low as $0.5 \mu\text{M}$, a quick reaction time 3 s, and good sensitivity $120.5 \mu\text{A mM}^{-1} \text{cm}^{-2}$.

In 2014 R. Ahmad, et al [21] prepared aligned zinc oxide nanorods (ZnO NRs) using a low-temperature solution method an equimolar 0.03 M of $\text{Zn}(\text{NO}_3)_2 \cdot 6\text{H}_2\text{O}$ and HMT and heated at $85 \text{ }^\circ\text{C}$ for 5 hours, which were produced directly on an Ag sputtered glass substrate. The synthetic urea sensor (glass/Ag/ZnO NRs/urease) demonstrated a high sensitivity of $41.64 \mu\text{A/mM cm}^2$, a broad linear range of 0.001-24.0 mM, and a small detection limit of $10 \mu\text{M}$. The electrode's specific surface area and NRs adhesion are expressly increased by the directly manufactured ZnO NRs.

In 2015 J. Anusha, et al [22] prepared the biosensors by immobilizing glucose oxidase on chitosan submicron particles (GCSP) created from the gladius of *Todarodes pacificus*, an efficient enzymatic glucose biosensor. Electrochemical analysis was used to estimate the electrode's glucose sensing behavior, and the results demonstrated outstanding analytical performance. The electrode ZnO/Pt/GCSP coupled with GOx demonstrated high sensitivity $88.76 \mu\text{A mM}^{-1} \text{cm}^{-2}$ with a low detection limit $90 \mu\text{M}$ and rapid response $\leq 2\text{s}$.

In 2016 A. Ibrahim, et al [23] reported the preparation and characterization of a multiwall carbon nanotube (MWCNT) as an extremely sensitive and selective glucose biosensor. The MWCNT composite with ZnO

Chapter One: Introduction and Literature Review

ellipsoids decoration was made using simple ultrasonication and a hydrothermal technique. A very high and repeatable sensitivity of $157.5 \mu\text{A mM}^{-1} \text{cm}^{-2}$ and a detection limit of $5 \mu\text{M}$, based on S/N ratio, were displayed by the manufactured glucose biosensor. The manufactured biosensor had a large linear dynamic range of 0.01 to 15.0 mM and a correlation coefficient of $R^2 = 0.9994$. The manufactured ZnO ellipsoids decorated MWCNT composite based glucose biosensor also showed better sensing response for the detection of glucose in PBS and serum samples.

In 2016 J. Li, et al [24] reported an electrochemical glucose based on the immobilization of the enzyme, a biosensor GOx on a carbon electrode with a glassy surface was modified using hybrid silver-ZnO nanorods (HNRS). The HNRS contained various silver percentages were synthesized using a solvothermal technique in one stage hence it was heated at $120 \text{ }^\circ\text{C}$ for 12 hours. Glucose activated two linear responses from the sensor ranges from 0.01 to 0.1 mM and from 0.1 to 1.5 mM. The detection limit and the sensitivity were $18.7 \text{ mA M}^{-1} \text{cm}^{-2}$ and $5 \mu\text{M}$, respectively. They reported that the biosensor was steady, acceptable, selected and repeatable.

In 2018 N. Muthuchamy, et al [25] prepared enzymatic glucose sensor on a glassy carbon electrode (GCE), by using glucose oxidase (GOx) and zinc oxide (ZnO) nanoparticles embedded in nitrogen-doped carbon sheets (ZnO@NDCS). With a sensitivity of $231.7 \mu\text{A mM}^{-1} \text{cm}^{-2}$, the manufactured GCE/ZnO@NDCS/GOx biosensor demonstrated high and repeatable sensitivity, and response time 3 s. Additionally, with a correlation coefficient $R^2 = 0.998$ and a lowest detection limit (based on a S/N ratio = 3) of $6.3 \mu\text{M}$, exhibited a broad linear range from 0.2 to 12 mM. The GCE/ZnO@NDCS/GOx biosensor has been successfully used for the quantitative monitoring of glucose in human blood serum and is acceptable stable and selective.

Chapter One: Introduction and Literature Review

In 2019 X. Hoo, et al [26] used the hydrothermal method to prepare ZnO NRs as a glucose biosensor. They used ZnO seeds / ITOs which were vertically immersed in a growth solution containing 0.1 M zinc nitrate hexahydrate ($\text{Zn}(\text{NO}_3)_2 \cdot 6\text{H}_2\text{O}$) and 0.1 M HMT in screw-capped bottles and heated to 80 °C for 4 h. They achieved ZnO NRs with diameter of 70-100 nm and length of 800 nm. The optimized electrode, which was composed of Nafion, 60 μL of GOx, ZnO NRs, and ITO, demonstrated a low limit of detection of 0.18 mM and high sensitivities of 14.53 $\mu\text{A mM}^{-1} \text{cm}^{-2}$, within a broad working range of 0.05-1.0 and 1.0-20 mM.

In 2022 V. Myndrul, et al [27] manufactured a sensor that can quickly and cheaply detect diabetes using a ruthenium-doped carbon nitride (ZnO-g-Ru- C_3N_4) modified with a zinc oxide rod. The sensing device is an efficient enzyme-free glucose detector with high sensitivity 346 $\mu\text{A mM}^{-1} \text{cm}^{-2}$ across the applied lower potential of +0.26 V, vs. Ag/AgCl, quick response 3 s, and a wide linear range of 2-28 mM, as well as a lower limit of detection 3.5 nM. With justified repeatability, reusability (the single electrode may be reused 26 times in the physiological buffer and three times in serum), and stability, the biosensing gadget offers enhanced anti-interference ability. Additionally, the sensor device's real-time applicability in human blood, serum, and urine samples was assessed.

1.3 Thesis objectives

- 1) Preparation of 1D ZnO coated by Ag Nps.
- 2) Synthesis of highly sensitive biosensor of glucose-sugar concentration in the human body based on 1D ZnO pure and coated by Ag Nps.

1.4 Organization of the thesis

The organized of the thesis as follows: in chapter 1, the general introduction, literature review, and research objective are presented. Chapter 2 covers the ZnO nanostructures and fundamental for sensing applications and the history of biosensors. While chapter 3 covers the synthesis approaches of ZnO and ZnO nanostructures coated by Ag Nps and there characterization, and device fabrication methods. Finally, chapter 4 contain results and discussions.

Chapter 2:

Theoretical Part

Chapter 2: Theoretical Part

2.1 Introduction

The basic features of nanomaterials are the basis for nanotechnology applications. As a result, understanding the underlying physical features of nanomaterials is a crucial demand for designing rational devices. It should pay attention that as the dimensions of semiconductor substances drop down to the nanoscale, "quantum size effects" certain changes occurred in their physical properties.

2.2 Fundamental properties of ZnO

ZnO is a direct wide band gap semiconductor with n-type conductivity under UV radiation. During crystallization, a hexagonal wurtzite structure is formed with unique characteristics based on noncentrosymmetric structures of crystals. Wet techniques are used in procedures of the majority of ZnO synthesis. In comparison to tin oxide, ZnO has a higher affinity for biological entities, which is a plus prerequisite for future medical biosensor applications. Because of its wide E_g of 3.37 eV and high bond energy of 60 MeV in ambient conditions, ZnO has a high sensitivity. Furthermore, because of its nontoxicity, electron transfer potential, and high chemical stability, ZnO is a popular material for bimolecular immobilization without the use of an electron mediator [28]. Investigations into zinc oxide began in 1912. Following the development of the transistor, the semiconductor age began [29]. ZnO was the subject of thorough research as a compound semiconductor. Following, the discovery of zinc oxide's excellent piezoelectric capabilities in 1960 [30], surface acoustic wave devices were the first electronic devices to use ZnO as a thin layer [31]. The potential application of ZnO as a wide band gap semiconductor for light emitting devices and transparent or high temperature electronics is a significant driving force behind research on this material [32]. It has a reasonably high exciton binding energy making ZnO a good candidate for photodetectors. ZnO has a variety of applications in a wide range of fields, including sensing [33], magnetic [34], electronics [35], catalytic [36], and solar-powered gadgets [37]. Due to the lack of a center of mass,

Chapter 2: Theoretical Part

it is a promising substance for excitonic effects _ based optical systems. ZnO has symmetry of its wurtzite structure and a high electromechanical connection contains significant piezoelectric and pyroelectric characteristics. Furthermore, ZnO is biosafe and biocompatible, as well as phototoxic intracellularly, which makes it an attractive candidate for chemical sensor and biosensor applications [38].

2.3 Crystal structure and chemical binding

2.3.1 ZnO structure

ZnO is an II-VI compound semiconductor with an ionicity that falls in between covalent and ionic. Wurtzite zinc blende, and rocksalt are the crystal formations of ZnO, on the other hand, is the thermodynamically stable phase in ambient circumstances [39,40]. Since the zincblende materials are less ionic than the wurtzite materials, they are totally covalent and so suitable for use in semiconductor technology. Each Zn or O has four closest neighbors in the zincblende and wurtzite structures, and the in-plane bonds are stronger than the out-of-plane bonds due to higher electron densities. In the rocksalt structure, each Zn or O has six closest neighbors, in contrast to the zincblende / wurtzite structures [41] as shown in figures 2-1.

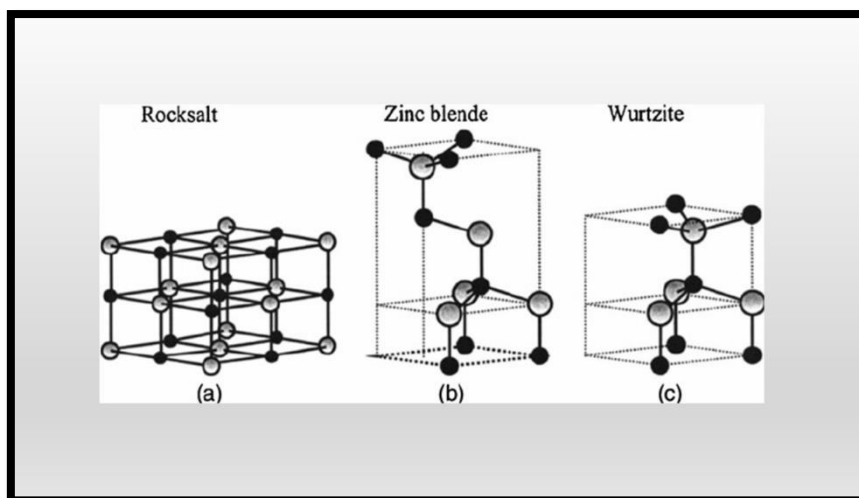


Figure 2-1. ZnO structures a) rocksalt b) zinc blend c) wurtzite [42].

Chapter 2: Theoretical Part

There are two distinct crystal lattices where ZnO crystallizes. The first is the wurtzite lattice, which has a hexagonal structure and is mostly used in the thin film sector as a transparent conducting oxide (TCO) or as a catalyst in the manufacture of methanol. The second structure, a spinal phase that is utilized to explain the earth's lower mantle, is more commonly referred to by geologists as the rocksalt structure at high pressure. But the wurtzite structure, which is widely known to have piezoelectric capabilities with a high electromechanical coupling factor, is a thermodynamically stable phase [43]. Applications of nanomaterials, that depend on morphology, have recently come under scrutiny [44]. Changes in the shape of nanomaterials create new opportunities for their use in previously unfeasible applications. Consequently, a variety of oxide materials are investigated to determine whether morphology and characteristics are correlated. Among them, one such instance is ZnO, which has reportedly been described as the richest family in terms of various material structures and morphologies [45]. By using a variety of techniques, including reactive sputtering [46], spray pyrolysis [47], zinc oxidation [48], electro deposition [49], pulsed laser deposition [10], chemical vapor deposition (CVD) [50], metalorganic CVD (MOCVD) [51], plasma enhanced CVD (PECVD) [52], low pressure sputtering [53], chemical bath deposition (CBD) [54], and the sol–gel route [55] are just a few of the due to its efficiency in creating thin, transparent, homogenous, multi-component oxide films of varied compositions on a variety of substrates at a cheap cost. The sol–gel method has become one of the most promising processing methods. Additionally, it enables fine-tuning of the film's thickness and refractive index by changing synthesis parameters. Several research groups have created ZnO nanostructures, including nanowires, nanotubes, nanobelts, and nanorods.

2.3.2 Electrical properties

ZnO semiconductors frequently exhibit n-type conductivity because of its native defects such as oxygen vacancies and zinc interstitials [56]. As previously stated, ZnO is a wide and direct bandgap semiconductor substances with a

Chapter 2: Theoretical Part

comparatively significant exciton binding energy, which makes it appealing for a variety of electrical and optoelectronic applications. Large band gap substances may have high interruption voltages, low noise generation, the ability to endure huge electric fields, and the ability to functionalize at high temperatures with high power. At sufficiently low and high electric fields, electron transport in ZnO differs. The energy obtained by electrons from a low electric field is negligible when compared to the thermal energy of electrons. As a result, providing a modest electric field has no effect on the energy distribution of electrons in ZnO. Electron motion does not depend on a few applied electric field and depends on Ohms law. The electron distribution changes dramatically from equilibrium and these electrons are hot when the temperature is higher than the lattice temperature by increasing the applied electric field to the extent that the energy of the electrons from the applied field is no longer low compared to the thermal energy. There is no loss of any energy in the lattice during a short and important period [39]. In worth mentioning that, the resistivity of a material is a measure of how strongly a material opposes the flow of electrical current. The resistivity (ρ) is the reciprocal of electrical conductivity. The unit of resistivity in SI units is the ohm-meter ($\Omega\cdot\text{m}$). The resistance is a measure of how difficult it is to pass current through a wire. Resistance depends on the resistivity. The resistivity is a characteristic of the material used to fabricate a wire or other electrical component, whereas the resistance is a characteristic of the wire or component. The unit of resistance is the ohm (Ω). For a given voltage, the higher the resistance, the lower the current [57].

2.3.3 Optical properties

A semiconductor's optical characteristics are determined by both inherent and extrinsic influences. Excitonic effects resulting from the Coulomb effect interaction are among the intrinsic optical characteristics of electrons in the conduction band (CB) and holes in the valence band (VB). Extrinsic characteristics have to do with injecting drugs or introducing flaws into the system. Between CB and VB, a semiconductor produces separate electrical states [39]. Optical

Chapter 2: Theoretical Part

transitions in ZnO have been studied using a variety of techniques, including optical absorption, transmission, reflection, photoluminescence, and cathodoluminescence. The distinction between semiconductors and insulators arises because in small band gap materials at room temperature a small, but appreciable so, number of electrons can be excited from the filled valence bands into the unfilled conduction bands simply by thermal vibration. Recently researchers employ nanoscale biosensors based on semiconductors resources, specifically metal oxides (MO), as artificial mediators to serve as a layer between enzymes and electrodes. MOs have a variety of morphologies, including rods, stars, flowers, and cones, porous or dense films which may be used in biosensor applications. In another hand investigations on mono-component MOs that contains multi-component or coupled semiconductors composite, tandem, heterostructures, etc... [58]. Furthermore, to improve certain properties, these materials were coupled with metal NPs or doped with other metal ions.

2.4 Ag doping ZnO for enhancement sensing performance

Electron transfer from redox sites in glucose oxidase (GOx) is enhanced by metallic nanoparticles such as gold and platinum doped with zinc oxide, but electron transfer is difficulty from zinc oxide to the electrode. Silver, a noble metal, has excellent electrical conductivity and good chemical stability [59]. Additionally, Ag-doped ZnO is simple to make and has been used in photo-degradation reactors and dye-sensitized solar cells to prevent the recombination of photo-induced electron-hole pairs [60]. Nevertheless, a pure ZnO has a limitation in the transferability of electrons since the electrons returned back to the oxidation centers in the enzyme rather than moving to the working electrode in the biosensor which reduces the performance of biosensors [61]. As a result, doping ZnO with Ag may speed up the passage of redox electrons from ZnO to the electrode of a glucose sensor. According to some studies, doping metals in ZnO has a significant impact on the morphologies and wettability of the resulting ZnO nanostructures [62], which in turn has an impact on the location of the solid-liquid

Chapter 2: Theoretical Part

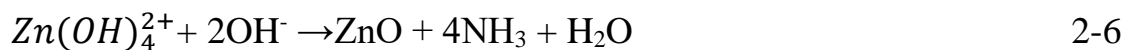
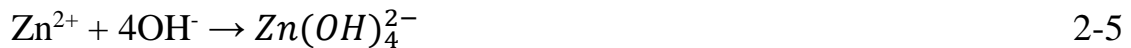
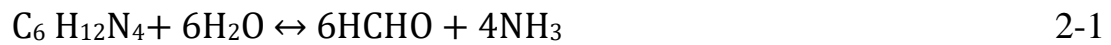
interface formed between the electrode and analytic liquid and ultimately, the effectiveness of the corresponding glucose sensor. However, more research has to be done on the combined effects of the aforementioned contributing factors on the effectiveness of glucose sensors. As a typical direct-bandgap oxide semiconductor, ZnO has special optical and electrical properties that make it a versatile material. ZnO thin films are typically doped with additional elements to enhance their optical and/or electrical properties [63]. Due to some point flaws, intrinsic ZnO thin films often display n-type conductivity such as zinc interstitials and oxygen vacancies. Consequently, creating a stable P-type ZnO material via doping has emerged as a key research area. According to theoretical research, Ag is a good option for doping to produce p-type ZnO in an oxygen-rich environment [64]. The impact of Ag doping on the electrical and optical characteristics of ZnO has thus been the subject of numerous studies [65].

2.5 Preparation methods

Several preparation methods could be used to prepare nanomaterials. Furthermore, the method of deposition thin-film is used to produce layers of less than 1 μm [66]. Entirely chemical ones involving gas and liquid phases are both purely physical. Numerous reactive sputtering methods and glow-based processes overlap as physical-chemical processes integrate the physical and chemical reactions. Special processes of film formation, including oxidation, which technically do not comprise any depositary processes, have been incorporated because of their significant relevance in solid state technology [67]. The growing availability of techniques for fabricating and characterizing semiconductor-based nanometric structures with controlled composition and dimensions has sparked widespread interest in their application in various biotechnological systems [68] including biosensors [69]. The qualities of 1D ZnO nanostructures are heavily influenced by their synthesis techniques, as well as their structure, surface morphology, chemical composition, surface contamination, electron transport, and other variables that influence sensing properties. As a result, various approaches

Chapter 2: Theoretical Part

have been used to create ZnO 1D nanostructures in order to modify their properties. These approaches, on the other hand, are considered expensive methods, require high temperatures, and have limit growth on soft flexible substrates. To address these issues, the "bottom-up" strategy can be used to synthesize new materials on a variety of substrates. In particular, the low temperature hydrothermal approach has been widely used for growing many different ZnO nanostructures for a variety of reasons, including low cost, simplicity, environmental friendliness, and ease of scaling up. Preparing conditions and growth of hydrothermal parameters can result in a variety of nanostructures. The following are the reaction processes that are involved in the nanorod approach [70]:



Because the properties of 1D ZnO nanostructures are determined by their preparing technique, surface morphology, size, shape, and structures, as well as chemical bonding, show critical roles in defining the properties of 1D ZnO nanomaterials and their associated sensing applications. Researchers are particularly interested in modifying the characteristics of 1D ZnO nanostructures for specific sensing applications. Organized preparation of 1D ZnO nanostructure is thought to be important in determining the possibilities and challenges for the creation of sensing devices.

Chapter 2: Theoretical Part

2.5.1 Dip coating method

The characteristics of the thin films and their thickness prepared in dip coating method depend on several factors such as immersion time, dragging speed, number of immersion times, solution formation, temperature, and environmental humidity. The substrate is withdrawal vertically at a certain distance, then it dips at a certain speed from the solution so that the substrate will be wet with a thickness and the thin film will be formed soon when the substrate is pulled out from the solution. The factors that affecting the thickness of the thin films in addition to the above are the inclusion of surface tension along with the height of the membrane due to the effects of drying and separation pressure or docking and is important for films less than 1 μm thick [71]. The thickness of the thin film (t) is calculated from the relationship (Landau_ Levich) [83]:

$$t = 0.94 \frac{(v_0 \eta)^{2/3}}{\gamma^{1/6} \sqrt{\rho g}} \quad 2-8$$

Where v_0 was the withdraw speed of the sample, γ is the surface tension of liquid at the position, g is the gravitational constant 9.81 m s^{-2} and η is the viscosity of the liquid. During the pulling of the substrate, the solution of the thin films begins to be attached to them, and the thickness of the thin films depends on the speed at which the substrate is pulled, hence the slower the pulling, the thinner the coating layer [73]. The advantages of this approach are cost effective, biomedical applications, providing corrosion and ion release protection, multilayered (thick) coating, high adhesion, ability to coat complex geometries, flexibility in the composition, and no need of conductive substrates. While the drawbacks of this technique are thickness control, slow rate of coating cycle, possibility of coating failure during heat treatment on multilayered coating structures [74,75].

Chapter 2: Theoretical Part

2.6 Sensing applications depend on ZnO and transition metals doped ZnO nanostructures

Nanomaterial-based sensors have gained considerable position in recent years, from industrial applications and scientific research perspectives. The most significant factors for the creation of new sensors-based devices are little power usage, facility of manufacturing, very accurate, immediately response results, high biological compatibility, portability, and ease of use for untrained people. Therefore, the preferred fabrication techniques are those based on an economic approach, with the use of low-cost materials and low-cost synthesis methods. Metal oxide semiconductor nanoparticles have drawn a lot of attention in response to the above needs regarding for promising uses in a variety of technical domains, as well as sensors. Metal oxide nanostructures appears as one of the most adaptable nanosubstances in the field of nanotechnology-based sensors due to their exceptional physical and chemical properties [76]. Due to the unique chemical and physical properties of ZnO nanostructures, it is considered one of the most promising metal oxides in many industries. ZnO nanostructures are very attractive to researchers in the field of sensing because of these qualities. Because of the features mentioned earlier which keep excitons in ZnO unchanging up to 350 °K, high transparency, high ionicity, and biocompatibility, zinc oxide nanomaterials have gotten a lot of attention in the sensing field [77]. In addition, ZnO is a versatile material that may be used in a variety of applications such as transparent electronics, optoelectronics, solar cells, smart windows, biodetection, and piezoelectric devices [78]. Furthermore, the performance of the sensors can be improved by doping various metals into the ZnO nanostructure or alloying ZnO with other metal oxides. This is because the dopant effects on the band gap, optical property, and electrical conductivity of ZnO nanostructures [79]. Furthermore, by doping transition metals into ZnO nanostructures, room temperature ferromagnetic characteristics can be produced, which has the potential to improve the performance of sensing devices and future spintronics applications [80]. 1D zinc

Chapter 2: Theoretical Part

oxide nanostructures, such as NRs, NWs, and nanobelts, are the preferred structures among the ZnO nanostructures. Due to their crucial physical properties and practical potential, nanotubes are becoming a prominent focus in nanoscience research and are of interest for a wide range of applications. There are numerous reasons for the high interest in 1D zinc oxide nanostructures in sensing applications. The electron transport is in direct touch with the surrounding, and high ratio between surface and volume, which is required for fast reaction kinetics. They can achieve excellent electronic conductivity, low power consumption, relatively simple preparation procedures, and large-scale production. Because of their high crystallinity, ultrahigh sensitivity, and ability to integrate addressable arrays on a mass manufacturing scale, 1D ZnO nanostructures have outstanding stability. It also has semiconducting and piezoelectric properties, which can be used to make electromechanically coupled sensors and transducers. It is also biocompatible and can be incorporated into microelectronic devices very readily [81]. The unique features of 1D ZnO nanostructures offer a promising mix of sensitivity, chemical selectivity, and an electrically and chemically programmable substrate, all of which are important for tailored sensor response [82]. As a result, 1D ZnO nanostructures are promising options for implementing sensor applications. Using multiple metals doped ZnO nanorods has also improved the high activity of several types of sensors, for example, high performance of UV sensors can be achieved using Cu, Ag, or Al-doped ZnO nanorods [83], Mg, Au, Al or Cr doped ZnO NRs for gas sensors [84], Cd doped ZnO NRs for humidity sensor [85], and Sb doped ZnO nanobelts for strain sensor [86].

2.6.1 Sensors and their applications depend on ZnO NRs

A sensor, as we discussed previously, is a device that detects changes in physical circumstances, chemical, or biological quantities and provides a measured signal. The design of a modern sensor system creates excellent opportunities because it is based on nanomaterials and structures that leads to efficient work of

Chapter 2: Theoretical Part

the sensors in terms of improved detection limit, high sensitivity, faster response and lower cost, in addition to that, small samples, high efficiency and ease of use for all groups. Conductors when they are in the form of nanostructures. Due to their appealing physical and chemical characteristics, zinc oxide nanostructures are one of the most promising metal oxide nanomaterials. One of the main areas of attention in nanoscience research for a variety of applications is 1D ZnO nanostructures due to their important physical features and application potential.

2.6.2 Biosensors and their applications based on ZnO NRs

L. C. Clark, the inventor of the oxygen electrode sensor, first proposed the notion of biosensors in 1956 [87]. Clark created the first biosensor in 1962 by immobilizing the GOx on modified oxygen electrodes and using it as an electrochemical sensor. The consumption of dissolved oxygen can be used to determine the amount of glucose in a solution [88]. The immobilized GOx electrode was invented in 1967 to monitor glucose concentrations in biological solutions and tissues in vitro [89]. The function of the biosensor is to detect the analytes by a biomaterial, as this interaction results in a measurable signal. The sensor consists of two parts, one of which is a biological receptor such as an antibody, an enzyme, or any other element that detects targeted analytes in a custom (selective) manner. The other part is the transducer, which converts the biological signal resulting from the interaction into a signal that can be displayed on a special screen after being amplified. Examples of these signals are light intensity, mass, voltage, current, capacitance, and resistance. These sensors are used in many applications and technology, including medical diagnosis, defense, security, food and drug delivery [90].

The most crucial characteristics of biosensors are high sensitivity, selectivity, chemical stability, biocompatibility, minimal hardware requirements, quick reaction time, low cost, and comfort for non-expert users. Consequently, a transducer with excellent electrical, optical, magnetic, and mechanical properties was constructed using nanomaterials. The most often used biosensors in biosensing

Chapter 2: Theoretical Part

applications have been electrochemical ones. The transducers detect a biological signal generated by a bio-receptor using an amperometric, potentiometric, or conductometric pathway. Additionally, due to their small size, low cost, low volume, limited hardware needs, and low power requirements, electrochemical devices are ideally equipped for dispersed testing and have enormous potential in a number of biomedical and environmental applications. In electrochemical biosensors, electron transport from redox-active biomolecules to electrodes typically occurs indirectly through the use of redox mediators. For biosensors based on direct electron transfer (DET), the absence of mediators, on the other hand, results in high selectivity because both the electrode material and the enzyme operate in a potential window closer to the redox potential of the enzyme itself, making biosensors resistant to competing reactions. [91]. Without adding a mediator to the analyzed solution, the electrochemical transducer based metal oxide nanostructures enhance direct electron transfer processes, amplification, and orientation of the analytic signal of the bio-recognition response. Metal oxide-based transducers are well suited for direct and quick biosensors that can transform biological recognition responses to electrical signals [92]. 1D ZnO nanostructures in particular have many notable properties for applications of biosensors such as their high efficiency of catalytic, high ratio of surface area to volume, biocompatibility, stability, strong adsorption ability and fast electron transfer. These characteristics make ZnO NRs attractive candidates for biosensor applications that can't be done with big sensors at the same time.

2.7 Glucose Biosensor

A sensor that connects a physicochemical transducer with a biological component to form an electronic signal proportional to a single analyte is known as a glucose biosensor. The resulting signal is transmitted to the result display device [93,94]. Ideally, the "bio"-element does not recognize any other analyte and is highly specific to the analyte to which it is sensitive [95]. Because of the development of several signal transmission technologies, the performance and

Chapter 2: Theoretical Part

sensitivity of sensors have improved due to the use of nanomaterials. Sensors, nanosensors, and other nanoscale systems have made in vivo analysis quick and easy due to their dimensions, which are a fraction of a micrometer. The platinum electrode network is one of the most important examples of its use as very sensitive electrodes [96]. Several works for developing new principles and sensor architectures, especially for glucose converting systems [97]. The Yellow spring instrument (YSI) Company first commercialized electrochemical glucose biosensors in 1975. Initial proposals for implanted sensors in contribute with radio transmitters for wireless data read-out were proposed simultaneously. The growing number of diabetic patients became increasingly interested in accurate glucose monitoring. Although glucose self-monitoring is widely accepted and delivers significant improvements in diabetes patients' quality of life, it is clearly limited by the number of daily tests that are routinely conducted [98]. It is not practical to collect small volumes of blood by pricking the finger and monitoring the blood sugar level with single-use test strips during the night, nor does it provide meaningful data concerning blood glucose trends, peaks, or patterns. There is obviously a high demand for improved sensing technologies for continuous glucose monitoring (CGM) [99]. Sensors are based on a general concept, which is the measurement of the Faradic current response in which the active types of reduction and oxidation in the active sample electrode-solution are transformed based on a constant voltage applied between the reference electrode and the working electrode. [100]. Enzyme-based amperometric sensors are biorecognition elements that catalyze substrate conversion. Electrons are transferred between the electrode and enzyme or inversely in redox active enzymes to re-establish the redox active state and generate a measurable current [101]. One of its advantages is the substrate specificity of enzyme-based amperometric sensors. Furthermore, the relationship between analyte concentration and produced current signal allows for a simple but reliable electrochemical detection [102]. As a result, enzyme-based amperometric

Chapter 2: Theoretical Part

sensors are well suited to implant in vivo. CGM systems depend on amperometric biosensors have a 14-day battery life and a major increase in ease of use due to the ability to link the transmitter of the sensor to a receptor system and self-tracking glucose levels in blood via particular applications [103].

2.7.1 Components of biosensors

A biosensor is a device that combines a biological component with a physiochemical detecting system and detects, transmits, and stores data about an analyte. A biosensor that operates in the nanoscale zone is called a nanosensor. Optical biosensors, electrical biosensors, electrochemical biosensors, nanowire biosensors, nanotube-based biosensors, viral nano biosensors, and nanoshell biosensors are some of the several forms of nanobiosensors. Figure 2-2 demonstrates a fundamental biosensor assembly that consists of a bioreceptor, or biological recognition element, a transducer, and a processor. Living biological systems like cells, tissues, or entire organisms, as well as biological molecular species like antibodies, enzymes, and proteins, are employed as biological recognition components. The transducer basically performs the role of a translator, identifying the biological or chemical event from the biological component and converting it into another signal for the processor to interpret, which then translates it into a measured output.

Chapter 2: Theoretical Part

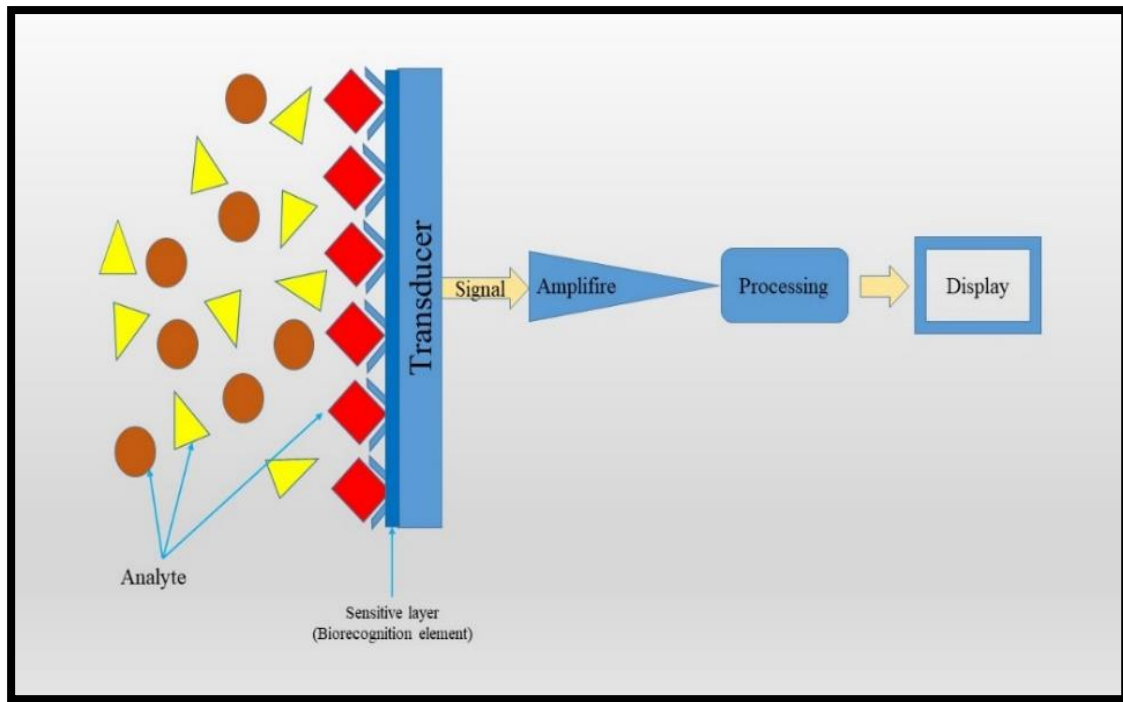
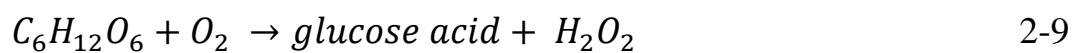


Figure 2-2. Biosensor elements and mechanism[96].

Clark and Lyons developed a glucose sensor using an electrochemical method to monitor oxygen consumed by enzyme-catalyzed. A thin layer of glucose enzyme is immobilized on the working electrode to be reacted according to the following equations 2-9, 2-10 [88]:



The reductive detection for oxygen consumption can be calculated by applying a negative voltage to the cathode electrode:



Chapter 3:

Experimental Methods

3.1 Introduction

This chapter includes a description of the method of work, the manufactured devices used to complete the preparation of samples, the chemicals used during the preparation of samples, the type of tests, and the devices used in characterizing the samples.

3.2 Manufactured devices

3.2.1 Dip coating design and fabrication

In this project, a low-cost manufactured home-made dip coating system was used for the production of a ZnO thin film. The system includes a stepper motor 42HD2037, NEMA17, 33 mm, stepper driver module TB6600, 4.5A, AC/DC adapter JCY-1250, output 12 V-5 A, SK8 SH8 vertical type holder 8 mm linear rail shaft end support, 626ZZ ball bearing, Copper nut for T8 lead screw, Chrome plated smooth rod diameter 8 mm length 320 mm, flexible couplings 8 mm, T8 guide lead screw 300 mm, and container. The stepper motor rotates the lead screw, which causes the coating arm to move downward or upward, figure 3-1 illustrates a diagram of the dip coating system.

Chapter 3: Experimental methods

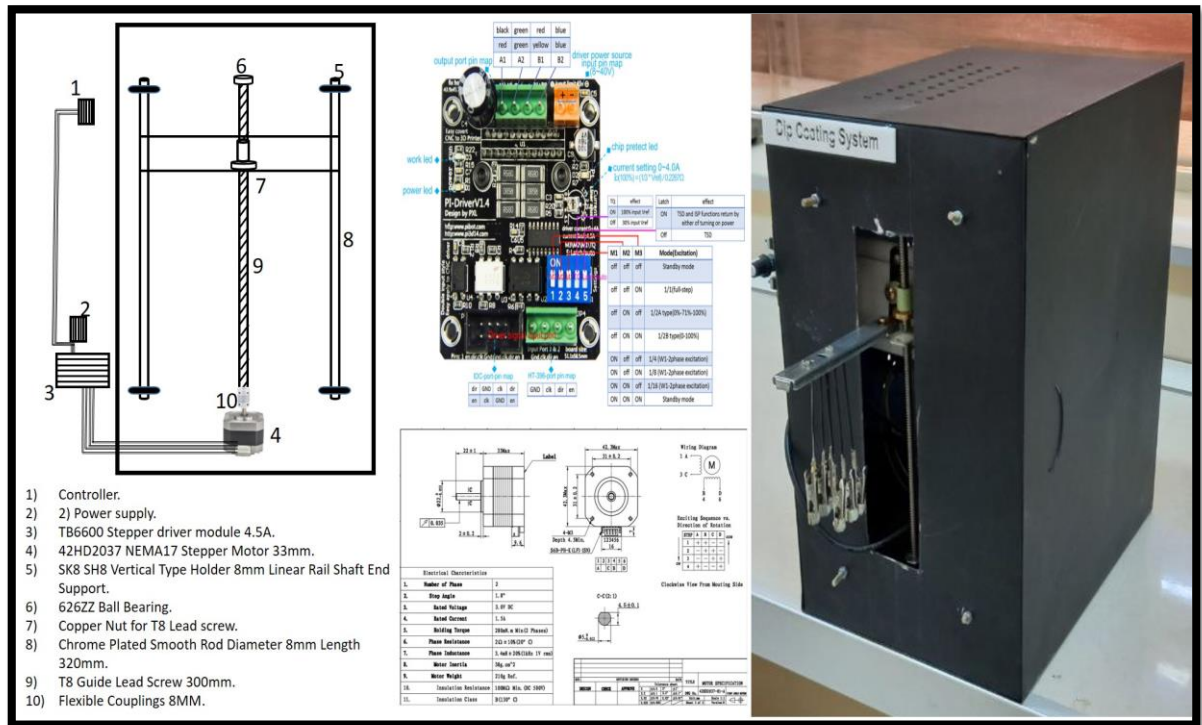


Figure 3-1. Schematic diagram of designed dip coating system.

The main forces influencing the dip-coating process are inertia, solution viscosity, gravitational force, and liquid surface tightening [104]. The device exhibited completely controlled parameters depending on the driver and the controller. The novelty of this work is the use of copper nut and T8 lead screw which leads the stepper motor to be smoothly moved and gives a high flow of movement. Generally one of the drawbacks of this method is that it is considered a time-consuming method [105,106]. This problem was overcome by making a sample holder that can carry six samples at once or more to obtain 6 samples at the same time and with the same preparation conditions as shown in figure 3-2.



Figure 3-2. a) The developed sample holder, b) copper nut and T8 guide lead screw 300 mm.

3.2.2 Manufacturing the muffle furnace

Annealing processes need an electric furnace, which was successfully manufactured by building the first inner insulating layer of gypsum blocks material, as it can withstand a temperature of more than 500 °C. Then it is covered with another insulator of fiberglass, and finally placed in an iron box to preserve the internal parts. As for the heaters, nine heaters, each with a power of 300 watts, were used and distributed as shown in figure 3-3. The muffle furnace temperature is controlled through a controller and thermocouple in order to maintain the muffle furnace temperature and the accuracy rate is ± 2 °C. To protect the user of this device, an electrical switch has been connected to prevent the current leakage 30 mA in anticipation of any leakage during the work.



Figure 3-3. Manufacturing muffle furnace.

3.3 Materials and methods

The materials that were used in preparing the thin film as follows: The coating solution used Zinc acetate [$\text{Zn}(\text{CH}_3\text{CO}_2)_2 \cdot 2\text{H}_2\text{O}$] and absolute ethanol [$\text{CH}_3\text{CH}_2\text{OH}$ J.T. Baker]. For growth solution used zinc nitrate hexhydrate [$\text{Zn}(\text{NO}_3)_2 \cdot 6\text{H}_2\text{O}$] (99.998%) and HMT ($\text{C}_6\text{H}_{12}\text{N}_4$) 99 % Sigma- Aldrich. For coating by silver used AgNO_3 . The active element for the working electrode used Glucose oxides from *Aspergillus Niger* (GOx, G7141-10KU) Sigma- Aldrich, phosphate buffered saline (PBS) with Ph = 7.4. For cross-linking procedure used Nafion ($\text{C}_7\text{HF}_{13}\text{O}_5\text{S} \cdot \text{C}_2\text{F}_4$) Sigma- Aldrich and glutaraldehyde ($\text{C}_5\text{H}_8\text{O}_2$) Sigma- Aldrich.

3.4 Preparation method

3.4.1 Preparing seed layer – Cleaning methods

Indium Tin Oxide (ITO) coated glass substrates $15 \Omega/\text{sq}$, size (355*406*1.1) mm were employed as the working substrates. The sample size was 20 mm *15 mm. Before coating process, the ITO were cleaned using the following cleaning approach. The ITO were submerged in ethanol under sonication using an ultrasound sonicator (BK200, China, from local market).

Chapter 3: Experimental methods

The sonication process were applied for 10 minutes to remove organic contaminants and undesirable particles. Then the cleaning processes were repeated with the same conditions using distilled water. Following these cleaning procedures, drying the substrates using a hair dryer.

3.4.2 Preparation and deposition of seed solution

To prepare the seed solution, zinc acetate dihydrate was dissolved in ethanol with continuous stirring by a magnetic stirrer for 60 minutes at 60 °C to obtain a homogeneous solution at concentration of 0.1 M viscosity 1.13 Pa.sec and Φ equal 6. This solution was moved to the dip coating system for deposition. The deposition included several consecutive steps, first immersing the ITO substrate in a solution containing the coating material at a constant speed 10 mm s⁻¹. Then the substrate remained in the solution for a certain period 5 minutes and then the substrates were pulled upwards at the same speed 10 mm s⁻¹. After dragging the samples, they were dried at 90 °C for 10 minutes on the hot plate to evaporate the solvent to obtain an ultra-thin layer. These processes were repeated one, two, and three times. Finally, the samples were annealed in a muffle furnace for 60 minutes at 300 °C to enhance the crystallinity. The preparation procedure was illustrated in figure 3-4.

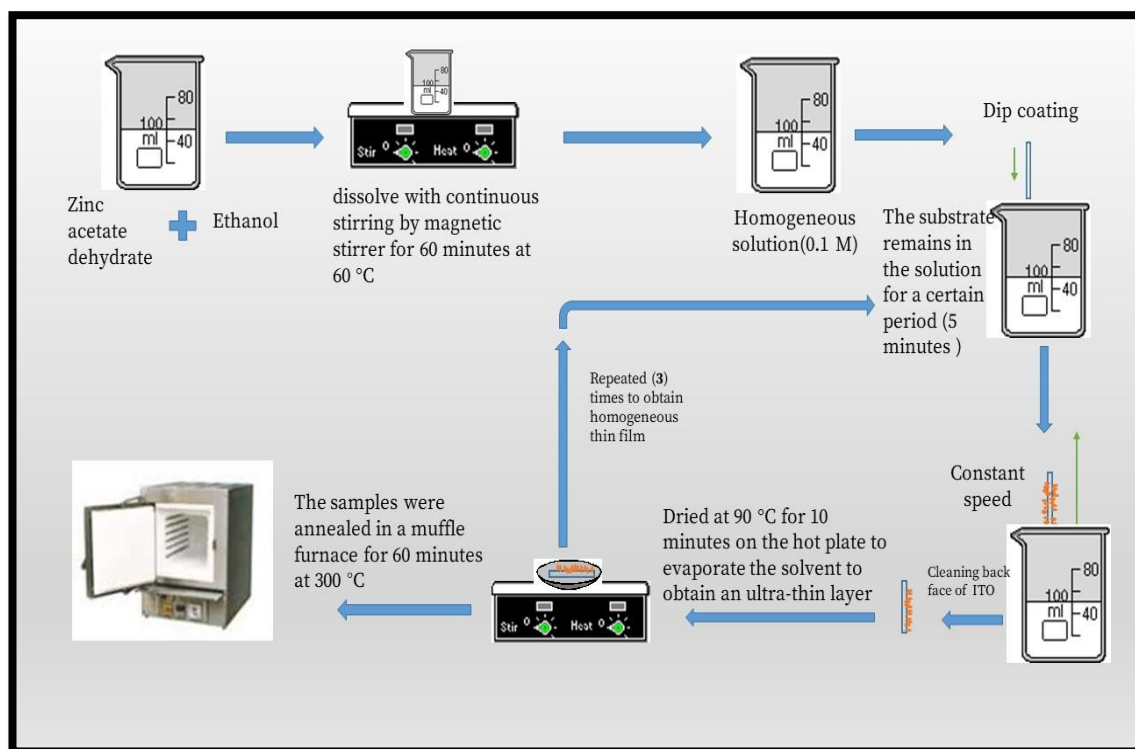


Figure 3-4. Schematic diagram of the sample preparation procedure.

3.4.3 Synthesis of ZnO NRs

The ZnO NRs were grown on a thin film of ITO in this dissertation. The most often employed chemical agents to manufacture ZnO NRs in the precursor solution preparation approach of ZnO nanocrystals are zinc nitrate hexahydrate ($\text{Zn}(\text{NO}_3)_2 \cdot 6\text{H}_2\text{O}$) and HMT ($\text{C}_6\text{H}_{12}\text{N}_4$) [107]. A solution of equimolar amounts (0.05 M) of zinc nitrate hexahydrate and HMT solution were prepared separately in deionized water for 30 minutes. After that, both transparent solutions were rapidly mixed by introducing the HMT solution into the Zn ions solution while stirring continuously [38]. Rapid mixing was used to obtain a homogeneous solution or monodisperse nanoparticles. The hydrothermal growth procedure is the ultimate step. The substrate-attached ZnO seed-layers were plunged horizontally in the growing solution and maintained at 90 °C in a prepared electrical furnace. After that, the samples were collected after (6 hour) growth times, washed with deionized water, and dried at room temperature for further

Chapter 3: Experimental methods

characterizations and device fabrication. The concentration of the solution has been chosen at 0.05 M for the majority of the cases in this study.

3.4.4 Coated ZnO NRs by Ag NPs

After completing the ZnO NRs growth process with the aim of improving the electrical properties and increasing the amount of carrying electrons and achieving better results in increasing the electrode's sensitivity to glucose, the samples were coated with Ag NPs. To prepare the solution, AgNO₃ is dissolved in DI water to obtain a concentration of 1 mM. The sample was coated by dip coating method, same conditions for preparing the seed layer, and then dried at room temperature.

3.5 Preparation glucose biosensor

Immobilizing presses of the enzyme on the electrode surface, 10 mg / ml of GOx was dissolved in a phosphate buffered saline (PBS). 5 μL of the enzyme solution was deposited on the surface of the electrode and was left for 120 minutes to dry at room temperature. The cross-linking procedure was carried out by adding 5% of Nafion (C₇HF₁₃O₅S·C₂F₄) and 2.5% of glutaraldehyde (C₅H₈O₂) on the surface of the electrode and was left to dry at room temperature. In addition, 2 μL of Nafion was deposited on the electrode surface to avoid possible enzyme leakage and eliminate foreign interferences.

3.6 Characterization methods

Different characterization techniques were utilized to evaluate the morphology, optical characteristics, structure, I-V characteristic, and cyclic voltammetry, once the growth process was completed. To obtain precise information on the crystal structure of the materials.

3.6.1 X-ray diffraction

XRD is a fast and effective technique for determining a crystalline material's phase, provide data of unit cell lattice parameters, crystal orientation,

Chapter 3: Experimental methods

micro strain equation 3-3, dislocation density equation 3-2, crystal size (Scherrer equation 3-1) and crystal structure [108]:

$$D = k\lambda/(\beta \cos\theta) \quad 3-1$$

$$\delta = 1/D^2 \quad 3-2$$

$$\varepsilon = \beta / (4*\tan (\theta)) \quad 3-3$$

Where D is crystal size nm, k is Scherrer constant (0.9), λ is the wavelength for X-ray source 1.5406 Å, β is full width at half maximum (FWHM) radians, and θ is peak position, δ is dislocation density nm⁻², and ε is microstrain. The dislocation density (δ) is representing the size of the defect in the crystallite. The higher δ values specify inferior crystallinity levels for the films because δ inversely proportional to the square of crystal size [109] equation 3-2. XRD, SHEMADZU / Japan, examination in Iran, was employed for characterizations in order to assess the thin films' structural characteristics. The X-ray diffraction technique is commonly used to characterize unknown crystalline materials. The XRD technique relies on constructive interference of X-rays and a crystalline sample as its operating principle [110]. The atoms in a crystal are distributed in space in a regular pattern, resulting in crystal lattices, with a spacing distance d, a group of parallel planes formed resulting from these lattices, the cathode ray tube produced X-Rays and filters them through nickel filters and directed toward the sample. When X-rays of wavelength are projected at an angle onto a crystal lattice, the interaction of the incident X-rays with the sample produces:

$$n\lambda = 2d_{hkl} \sin \theta \quad 3-4$$

Where n = 1, 2, 3 ... (ordinarily n = 1), λ is X-Ray wavelength 0.15418 Å, d_{hkl} is the separations between the planes, θ is the inclination of the lattice

Chapter 3: Experimental methods

planes with respect to the incident beam, the 2θ is the angle of incidence and scattering of beams, and maximum intensity of 2θ was Bragg angle. All diffraction paths of the lattice are constructed by scanning the sample through 2θ range. Equations 3-5, 3-6, and 3-7 can be used to determine the lattice parameter of the ZnO hexagonal wurtzite based on these XRD patterns. The diffraction vector S intersects the angle between the incident and diffracted beam [79], and the plan $[hkl]$ is at right angles to a plane of atoms. Finally, $a = b$, and c the lattice constants, as well as the spacing d_{hkl} , for ZnO wurtzite structure, can be computed using the following relationships:

$$a = \sqrt{\frac{1}{3} \frac{\lambda}{\sin\theta}} \quad 3-5$$

$$c = \frac{\lambda}{\sin\theta} \quad 3-6$$

$$\frac{1}{d_{hkl}^2} = \frac{4}{3} \frac{h^2+hk+k^2}{a^2} + \frac{l^2}{c^2} \quad 3-7$$

3.6.2 Field emission scanning electron microscope (FESEM)

One of the most significant devices for morphology investigation is the field emission scanning electron microscope (FESEM), images are created by scanning samples with a focused electron beam in a FESEM. Electrons interact with atoms in the sample, resulting in a variety of signals. The FESEM uses a concentrated electron beam to scan across the surface of the samples, then generates a huge number of signals, which are then translated to a visual signal that may be presented on a screen. These types of signals, on the other hand, are rarely found on a single machine and are dependent on the detector's type and specifications. Secondary electron detectors, on the other hand, are the most prevalent technique of detection in all FESEMs. Ionization of the specimen (atoms) occurs when the primary beam meets the sample's surface, and weakly

Chapter 3: Experimental methods

bound electrons may be emitted (secondary electrons). Because these electrons have low energy 3-5 eV, they may be able to migrate from a surface region in a matter of nanometers. As a result, secondary electrons precisely mark the position of the beam and provide high-resolution topography data [111]. Scanning the sample and detecting secondary electron signals generates the image of the surface on the screen. The FESEM pictures in this study were acquired using a secondary electron detector. EBSD Instrument: ZEISS SIGMA VP /Germany, examination in Iran.

3.6.3 UV-visible spectroscopy

UV-vis spectroscopy absorption is a type of spectroscopy used in the ultraviolet-visible region. UV-vis absorption spectroscopy offers information on light absorption as a function of wavelength, which characterizes the electronic transitions in the samples being examined. The UV-vis spectrophotometer measures the intensity of light passing through a sample and compares it to incident light intensity, light that passes through the sample before being detected [112]. Beer's law can be used to express the absorbance A :

$$A = -\log \frac{i}{i_0} \quad 3-8$$

Where i is the intensity of light passing through the sample and i_0 is the intensity of light before passing through the sample.

Transmittance is the transmission-mode analog to the reflectance. That is, transmittance is a dimensionless number defined by the ratio of the radiant flux (Φ_t) transmitted to the incident radiant flux (Φ_i). Like the reflectance, conservation of energy dictates that the transmittance for nonfluorescent materials have values in the interval 0 –1, inclusive. [113] The optical band gap of the grown samples was calculated in this study using the following equation [114]:

$$\alpha = \frac{k}{hv} (hv - E_g)^{\beta_d} \quad 3-9$$

Where $\alpha = 2.303 \times (\frac{A}{d})$ is the absorption coefficient, d is the thickness of the sample (length of nanorods), $\beta_d = \frac{1}{2}$ for direct band gap semiconductors and $k = \alpha\lambda/4\pi$ is the extinction coefficient, h is Plank's constant and hv is the incident photon energy [115].

$$(\alpha hv)^2 = C (hv - E_g) \quad 3-10$$

The optical energy gap of the sample was obtained from the intercept of the linear portion with the x-axis of $(\alpha hv)^2$ versus hv curve. All measurements done by instrument Shimadzu-UV-VIS Spectrophotometer (UV-1900i) examination in Kerbala University, collage of science, department of physics.

3.6.4 I-V properties Four-point probe (FPP) method single configuration technique

The four probes with collinear arrays touched a sample surface as shown in figure 3-5 to determine the sheet resistance using the single configuration technique. By flowing a current I_{14} between probes 1 and 4, the voltage V_{23} between probes 2 and 3 was measured by Keithley 2450 source meter, examination in Kerbala University, collage of science, department of physics,. The resistance (R_S) was then determined using Equation 3-11. Equation 3-12 was used to calculate the sheet resistance (R_{SS}) by applying a sample thickness and sample size correction factor against the probe spacing, as described in Equation 3-13:

$$R_S = \frac{V_{23}}{I_{14}} (\Omega) \quad 3-11$$

$$R_{SS} = K_S \times R_S \left(\frac{\Omega}{Sq} \right) \quad 3-12$$

K_S The correction factor, given by:

$$K_S = F(s_s/S) \times F(d/S) \times F(T) \times F(S) \quad 3-13$$

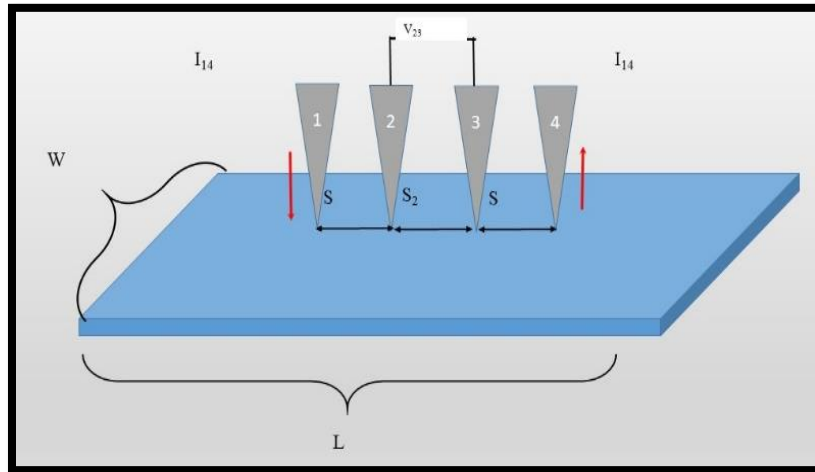


Figure 3-5. Four-point probe method for rectangular sample [116].

From Equation 3-14, $F(s_s/S)$ is the correction factor for the sample size (s_s) against the probe spacing S . The value of rectangular sample $F(s_s/S) = 4.0095$. In addition, $F(d/S)$ is the correction factor of sample thickness (d) against probe spacing S . $F(d/S)$ is equal to 1.000 if the probe spacing is 1.00 mm and the thickness is less than 0.3 mm [116]. Furthermore, $F(T)$ stands for temperature correction factor, and if the measured temperature is 23.0 ± 0.5 °C, $F(T)$ equals 1.000 since $F(T) = 1 - CT(T - 23)$. Additionally, $F(S)$ is the probe spacing correction factor, with $F(S) = 1 + 1.082 \times (1 - (S_2/S))$ [117]. If S_2 is assumed to be equal to S , then its value is set to be 1.000.

3.6.5 Electrochemical measurements

The electrochemical process may generate charges near the working electrode's surface, resulting in a potential difference between the biosensor's working electrode and the reference electrode in the electrolyte solution. When the concentration of ions in the target electrolyte solution varied, the

Chapter 3: Experimental methods

electrochemical response electromotive force (EMF) altered as well. The Nernst expression can be used to explain the EMF response of ion selective electrodes (biosensor) [118]:

$$E = E_o + \frac{RT}{ne} \ln\left(\frac{[Ox]}{[Red]}\right) \quad 3-14$$

Where E_o represents the cell potential under standard conditions, E represents the cell potential, T represents the temperature in kelvin, R represents the ideal gas constant, e represents the fundamental charge of electrons, and n represents the number of electrons transferred during the reaction. The concentrations of oxidized and reduced species are represented by $[Ox]$ and $[Red]$, respectively. The used log form of the Nernst equation is given by [119]:

$$E = E_o - \frac{0.059}{n} \ln\left(\frac{[Red]}{[Ox]}\right) \quad 3-15$$

By inhibiting enzyme activities, biosensors can also be utilized to detect some harmful chemical substances. The inhibitory effect of the heavy metal compound on the enzyme is either permanent or reversible. The phenomenon causes an alteration in enzyme activity. The following equation gives the glucose oxidase inhibition degree:

$$I\% = \left(\frac{I-I_0}{I}\right) \times 100 \quad 3-16$$

Where $I\%$ represents the degree of inhibition, I_0 represents the glucose response in the absence of the inhibitor, and I represents the glucose response in the presence of the inhibitor [120] [121]. The ZnO NRs coated by Ag NPs were utilized as an electrode for the GOx immobilization of the enzyme. The voltammetry measurements were performed using a (DY2300 Series Potentiostat / Bipotentiostat) Digi-ivy, Inc. Austin, Texas _USA, Model: DY2321, software version: DY2321X040A0227IR; DY2300, Revision 10.12.20. Line Frequency (Hz): 60. Additionally, a platinum (Pt) wire and an Ag/AgCl were used as counter and reference electrodes, respectively as showed

Chapter 3: Experimental methods

in figure 3-6. The cyclic voltammetry method was used with scan rates of 50 mVs⁻¹ and potential ranges between -1.00 to 1.00 V. All electrodes were compared according to the determined net current response based on glucose concentration at a constant voltage. The current value of the buffer solution without glucose was subtracted from the current value of the solution with glucose to obtain the net current value, denoted as μA . Operational stabilities were examined by employing each electrode 5 times in a glucose solution with a different concentration ranging from 0 to 100 μM .

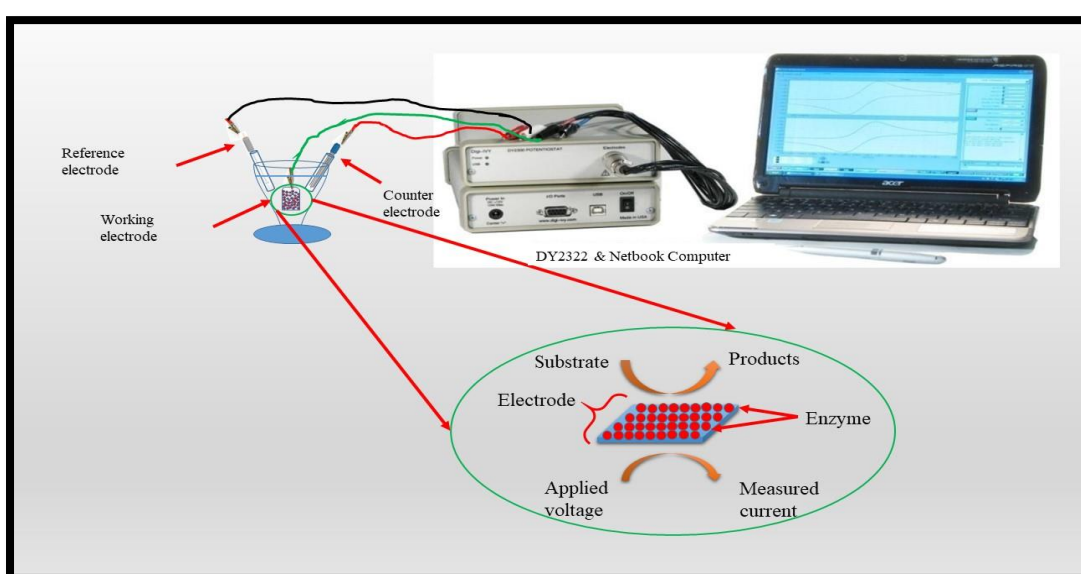


Figure 3-6. Cyclic voltammetry system and mechanism of working electrode.

The electrode sensitivity and the limit of detection of the modified electrode was calculated as shown in Eq. 3-17 [122] and Eq. 3-18 [123], as follows:

$$\text{Sensitivity} = \text{slop} / \text{active area} (\mu\text{A mM}^{-1} \text{cm}^{-2}) \quad 3-17$$

The amperometric sensitivity was obtained from the slope of the linear range calibration curves.

$$\text{LOD} = (3 \sigma s) / 3.3 \quad 3-18$$

Chapter 3: Experimental methods

Where σ is the standard error of the regression line, and s is the slope of the calibration curve.

Table 3-1 shows samples ID, dipping cycles for each sample, and their structures.

Table 3-1. Samples ID used in this thesis.

Sample ID	Dipping cycles	Sample structure
S ₁	1	Seed layer
S ₂	2	Seed layer
S ₃	3	Seed layer
S ₄	1	ZnO NRs
S ₅	2	ZnO NRs
S ₆	3	ZnO NRs
S ₇	1	Ag NPs coated ZnO NRs
S ₈	2	Ag NPs coated ZnO NRs
S ₉	3	Ag NPs coated ZnO NRs

Chapter 4:

Results and discussion

4.1 Structural properties

4.1.1 ZnO Seed layer

To investigate the structure of the prepared thin films, XRD analysis was performed as shown in figure 4-1. When comparing the diffraction peaks and the JCPDS data 96-900-8878, it was found that the prepared material shows hexagonal zinc oxide (P 63 mc) structure. The lattice constants of ZnO are $a = b = 3.25 \text{ \AA}$ and $c = 5.207 \text{ \AA}$. Generally, four main peaks Miller indices were detected namely, (002), (102), (103), and (202) which belong to the hexagonal wurtzite structure. The highest intensity was the plain (101) at angle $2\theta = 31.767^\circ$ which belong to ITO substrate. These results which were detected by XRD data proved that the deposited samples were pure which shows the effectiveness of the manufactured dip coating system for depositing pure thin films.

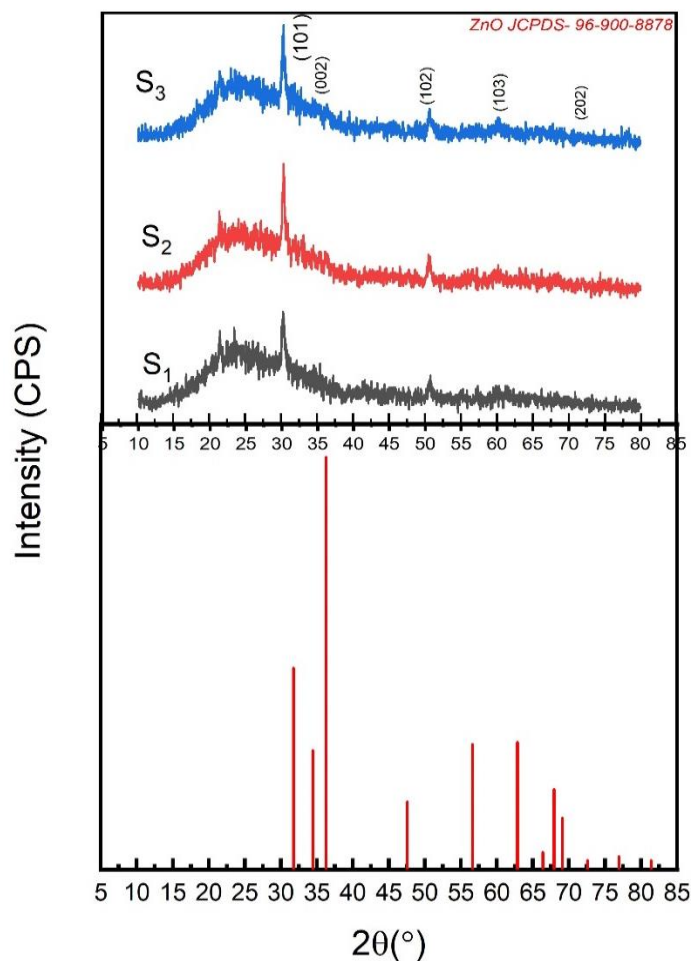


Figure 4-1. XRD patterns and slandered JCPDS data.

Chapter 4: Results and discussion

It was found from XRD data that the first layer has an average crystal size of about 20.13 nm, the second layer is about 20.95 nm, and it is about 20.95 nm for the three-layer sample indicate that by increasing seed layer thickness particle size will increased , as illustrate in table 4-1.

Table 4-1. Illustrate all parameters calculated from XRD data for samples S₁, S₂, and S₃.

Sample ID	2θ°	FWHM radians	(hkl)	D nm	Average crystal size nm(Eq.3-1)	δ *10 ⁻³ nm ⁻² (Eq.3-2)	ε*10 ⁻³ (Eq.3-3)
S ₁	34.19	0.51	(002)	16.30	20.13	3.77	7.24
	51.19	0.34	(102)	25.91		1.49	3.10
	62.1	0.51	(103)	18.18		3.02	3.70
S ₂	34.19	0.51	(002)	16.30	20.95	3.77	7.24
	51.19	0.34	(102)	25.91		1.49	3.10
	62.1	0.51	(103)	18.18		3.02	3.70
	72.2	0.42	(202)	23.41		1.82	2.51
S ₃	34.19	0.51	(002)	16.30	20.95	3.77	7.24
	51.19	0.34	(102)	25.91		1.49	3.10
	62.1	0.51	(103)	18.18		3.02	3.70
	72.2	0.42	(202)	23.41		1.82	2.51

4.1.2 ZnO NRs

The investigations were taking place by the comparison of the presented peaks in the XRD pattern of the samples with thus of the JCPDS 01-079-0205 data. Five main peaks appeared in this examination, (101) for ITO, (002), (101), (103), and (004) which belonged to the wurtzite hexagonal structure, and the highest peak intensity was (002) at 2θ = 34.527°, which represented the dominant trend of these prepared thin films as showed in figure 4-2. It was found that the prepared thin films had a hexagonal ZnO structure P63 mc, where the value of the lattice constant is a = b =3.2490 Å, c = 5.2070 Å. These results represented an indication of the high purity and crystallinity of the prepared thin films.

Chapter 4: Results and discussion

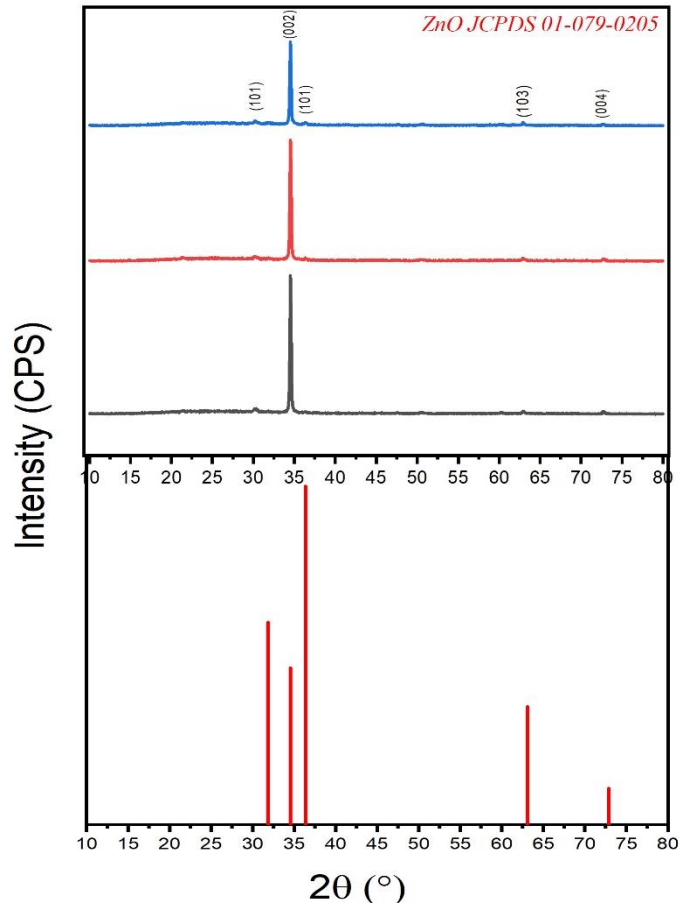


Figure 4-2. XRD patterns and slandered JCPDS data for S₄, S₅, and S₆.

The average crystal size from XRD data was 29.592 nm for S₄, 30.508 nm for S₅, and 25.73 nm for S₆, as illustrated in table 4-2.

Chapter 4: Results and discussion

Table 4-2. Illustrate all parameters calculated from XRD data for samples S₄, S₅, and S₆.

Sample ID	2 θ °	FWHM radians	(hkl)	D nm (Eq.3-1)	Average crystal size nm	$\delta * 10^{-3}$ nm ⁻² (Eq.3-2)	$\varepsilon * 10^{-3}$ (Eq.3-3)
S ₄	34.54	0.17	(002)	49.15	29.592	2.64	6.84
	50.58	0.68	(101)	12.98		0.41	2.38
	62.95	0.34	(103)	27.52		5.94	6.25
	72.74	0.25	(004)	38.86		1.32	2.41
S ₅	34.54	0.17	(002)	49.15	30.508	0.66	1.50
	50.58	0.68	(101)	12.98		3.81	8.19
	62.95	0.34	(103)	27.52		0.41	2.38
	72.76	0.34	(004)	29.15		1.32	2.41
S ₆	34.53	0.21	(002)	39.32	25.73	1.18	2.00
	36.32	0.51	(101)	16.47		3.81	8.19
	63.00	0.34	(103)	27.53		0.65	2.97
	72.69	0.34	(004)	29.14		3.69	6.75

4.1.3 ZnO NRs coated with Ag NPs

The as-prepared sample was investigated by XRD in order to identify the structural properties of the prepared materials, as shown in figure 4-3. The figure demonstrated that all the prepared samples contained five main diffraction patterns related to ZnO and three main diffraction patterns corresponding to Ag. Additionally, the figure revealed that all of the diffraction peaks were obviously crystalline, in which the peaks matched with the miller indices (100), (002), (101), (102), and (103) planes. According to the XRD analysis, the prepared samples can be indexed to the hexagonal, P63 mc, wurtzite hexagonal phase of ZnO, JCPDS 96-901-1663. As well, it could be noticed clearly that the samples contained extra peaks consisting of the (111), (200), and (311) planes related to

Chapter 4: Results and discussion

Ag cubic structure, which can be indexed to the cubic Pn-3m related to (JCPDS 01-072-0607). Due to the presence of concentration of Ag nanoparticles was 0.001 M, the ZnO NRs coated by Ag NPs pattern showed low intensity peaks of Ag NPs. The lattice constants of ZnO are $a = b = 0.325$ nm and $c = 0.520$ nm, whereas for Ag are $a = c = 0.490$ nm. It is obvious that the (002) plane alignment is referred to as the strong domain peak at a value of $2\theta = 34.540^\circ$. Particularly, the strong peak (002) indicated the preferred orientation. The presence of this peak indicated that the prepared samples exhibited 1D nanostructure with c direction, hence it was reported independent work that ZnO powder [124,125] or porous ZnO nanostructures [126] show the low intensity of (002) plane. This unique peak (002) indicated the good quality and high purity of the prepared samples. The average crystallite size (D) of the samples was calculated using the Debye–Scherrer equation. The ZnO has a crystallite size of around 4.14 nm. By comparison, it could be noticed that the intensity of the peak at the $2\theta = 34.540^\circ$ was low for sample S₇. Meanwhile, by increasing the dipping times for sample S₈ up to two times the intensity was strongly increased. By further increment of dipping times sample S₉, dipping cycles three times, the highest intensity was detected. These results indicated that by increasing the number of coated layers, improvement in the structure was perceived [127].

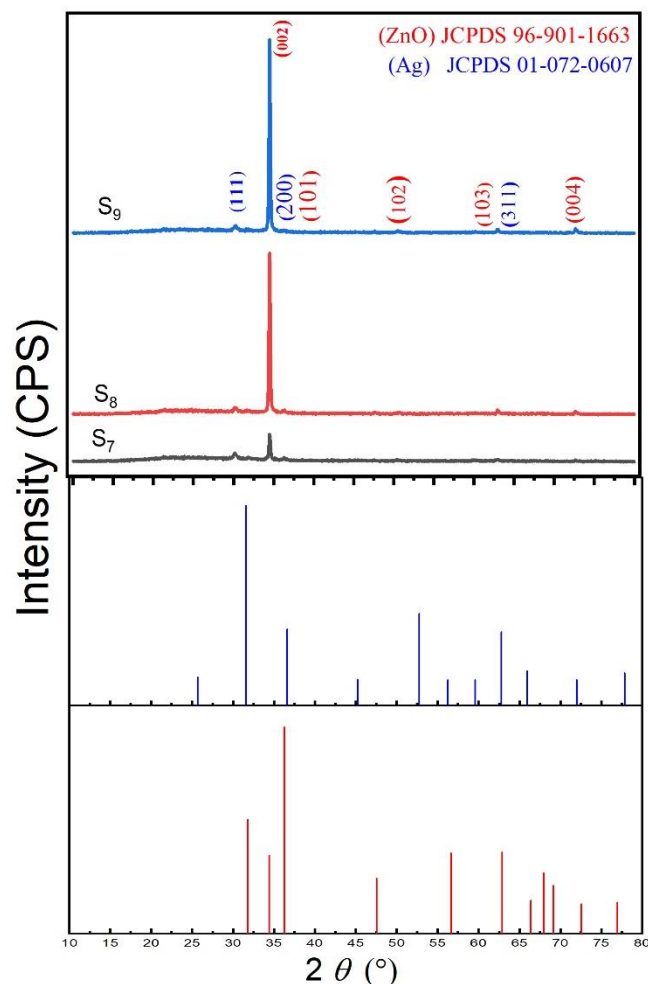


Figure 4-3. XRD diffraction pattern for S₇, S₈, and S₉ compared with JPCDS cards.

Represented the analysis of the structural properties of the samples using X'Pert program. By matching the data of XRD with the JCPDS, it was found that the ratio of Ag: ZnO were 26 to 74, 96 to 4 and 98 to 2 according to samples S₇, S₈ and S₉, respectively. These results indicated that as the length of NRs increased, the ratio of Ag reduced as showed in figure 4-4. Regarding XRD data, it was found that increasing in crystal size with increasing the thickness of seed layer, therefore the sample S₇ has an average crystal size of about 32.67 nm, S₈ is about 27.59 nm, and it is about 32.67 nm for S₉ and these crystals size were estimated as shown in table 4-3.

Chapter 4: Results and discussion

Table 4-3. Illustrate all parameters calculated from XRD data for sample S₇, S₈ and S₉.

Sample ID	2θ °	FWHM radiance	(hkl)	D nm (Eq.3-1)	Average crystal size nm	$\delta * 10^{-3}$ nm ² (Eq.3-2)	$\varepsilon * 10^{-3}$ (Eq.3-3)
S ₇	34.52	0.157	(002)	52.99	32.67	0.36	2.20
	36.32	0.315	(101)	26.54		1.42	4.19
	47.68	0.472	(102)	18.40		2.95	4.66
	62.94	0.394	(103)	23.64		1.79	2.81
	72.69	0.236	(004)	41.79		0.57	1.40
S ₈	34.52	0.157	(002)	52.99	27.59	0.36	2.20
	36.32	0.315	(101)	26.54		1.42	4.19
	47.68	0.472	(102)	18.40		2.95	4.66
	62.94	0.394	(103)	23.64		1.79	2.81
	72.69	0.236	(004)	41.79		0.57	1.40
S ₉	34.52	0.157	(002)	52.99	32.67	0.36	2.20
	36.32	0.315	(101)	26.54		1.42	4.19
	47.68	0.472	(102)	18.40		2.95	4.66
	62.94	0.394	(103)	23.64		1.79	2.81
	72.69	0.236	(004)	41.79		0.57	1.40

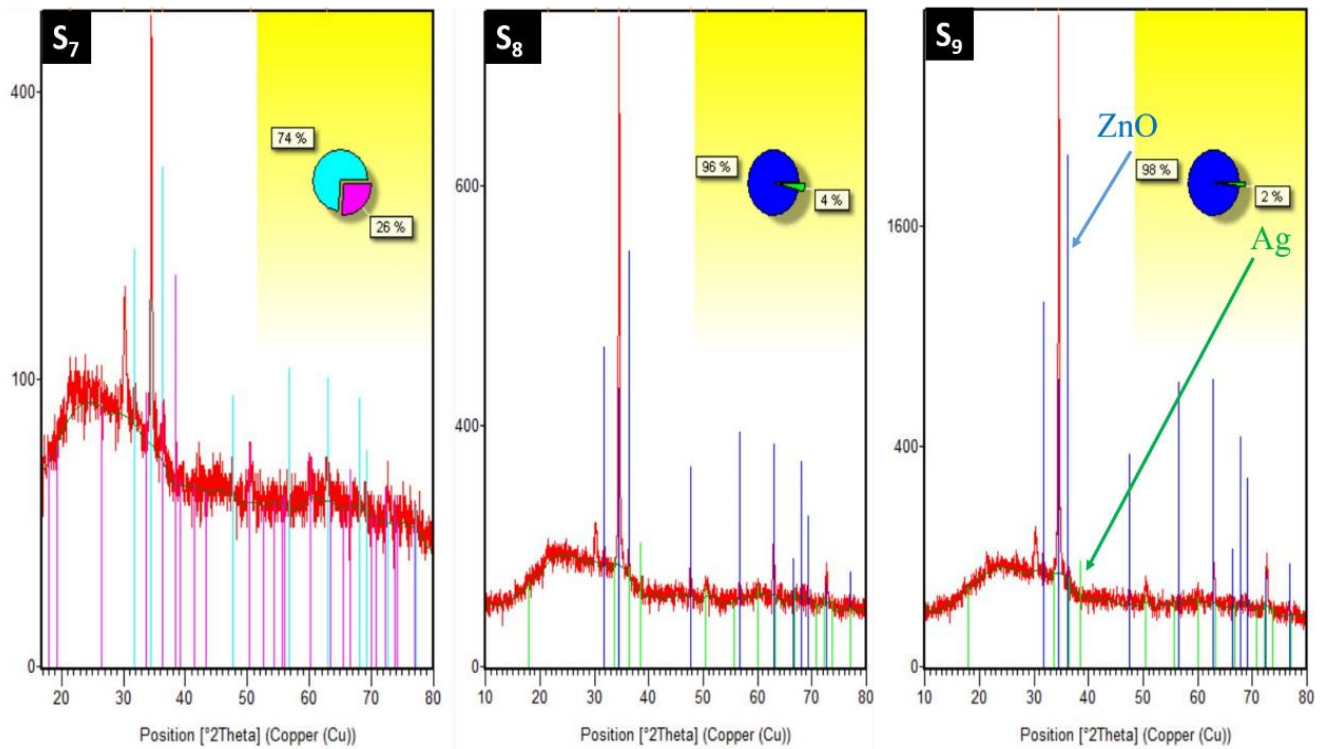


Figure 4-4. ZnO and Ag ratio in the XRD analysis depending on Ag - JCPDS 01-072-0607 and ZnO - JCPDS 96-901-1663 for samples S₇, S₈, and S₉.

4.2 Morphological properties

4.2.1 ZnO Seed layer

In order to ascertain the effect of dipping times on the thickness, morphology and topography of the prepared thin films, FESEM studies were conducted. Figure 4-5 a, b, and c show the cross section of S₁, S₂, and S₃, respectively. As for the S₁, figure 4-5a the thickness was 133 nm. By increasing the dipping time to two times as shown in figure 4-5 b the thickness was increased to 465 nm. Finally, by increasing the dipping times to three times, as in figure 4-5c the thickness becomes 497 nm. These results indicated that increasing the dipping time is an effective way to control the thickness.

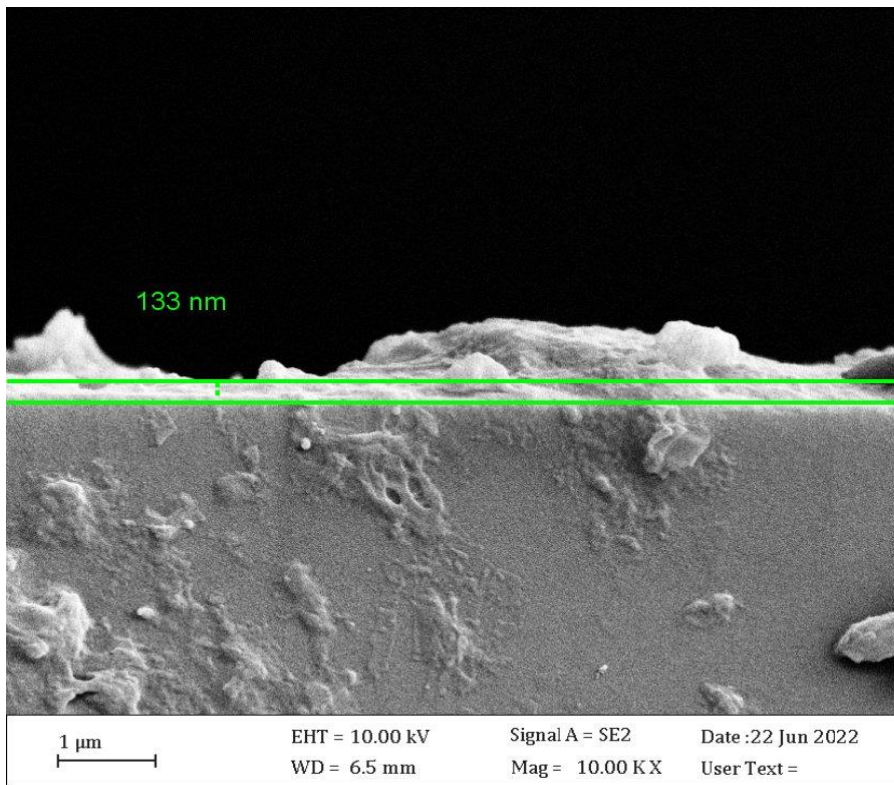


Figure 4-5a. Cross-section of sample S₁.

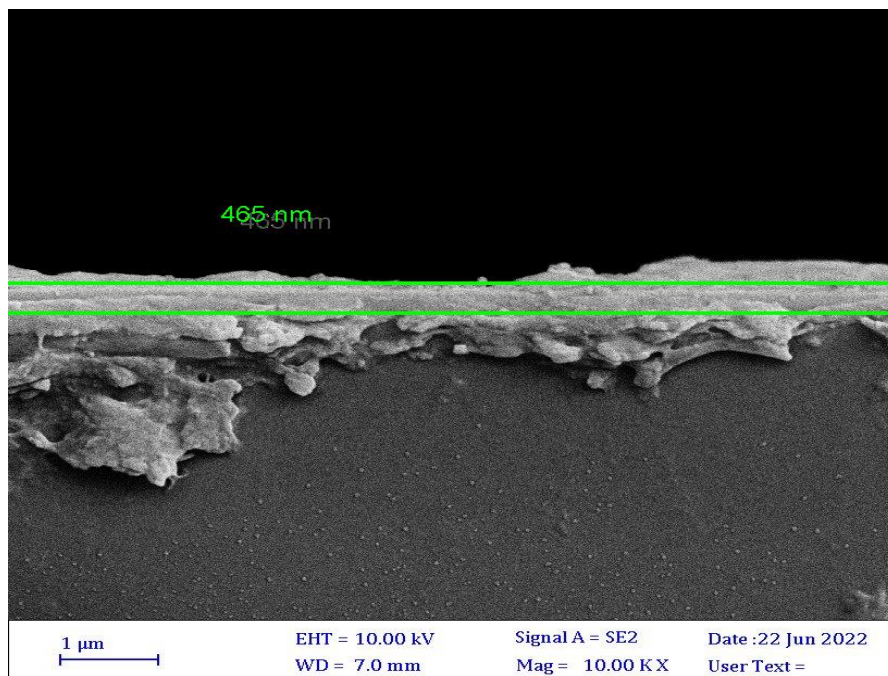


Figure 4-5b. Cross-section of sample S₂.

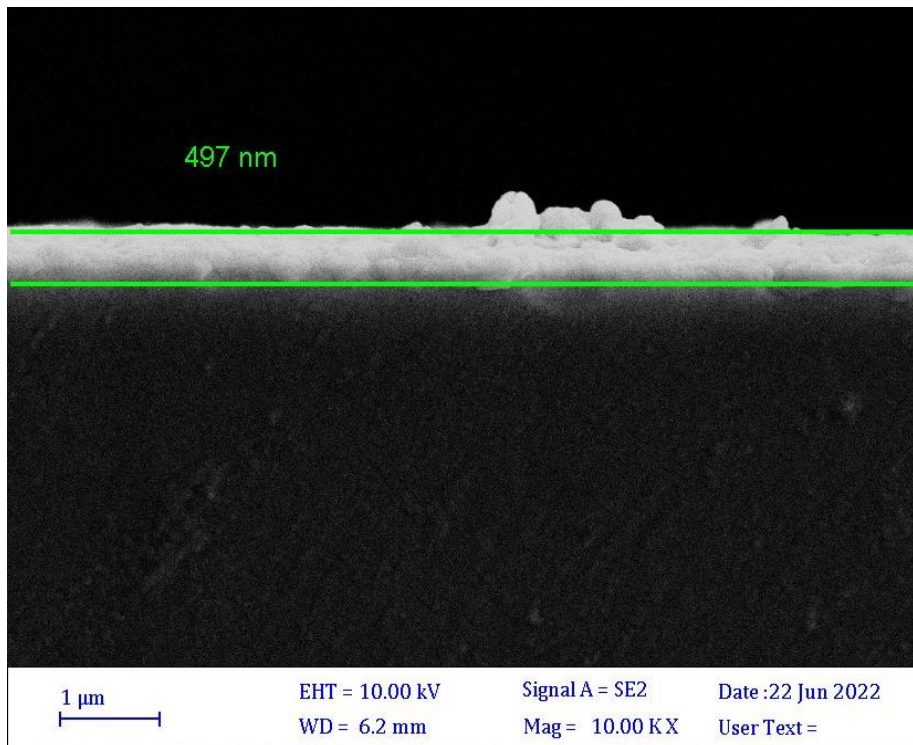


Figure 4-5c. Cross-section of sample S₃.

Figure 4-5 d, e and f represents the top-view of the prepared samples. It is clear that after annealing, the ZnO particles aggregated to form an un-continued thin film. When coating for the second time, these voids were filled and a homogeneous distribution layer was formed, as shown in figure 4-5 e. As for the third layer, the average diameter of its bodies is greater than that of the second layer, and it is also homogeneous distribution in figure 4-5 f.

Chapter 4: Results and discussion

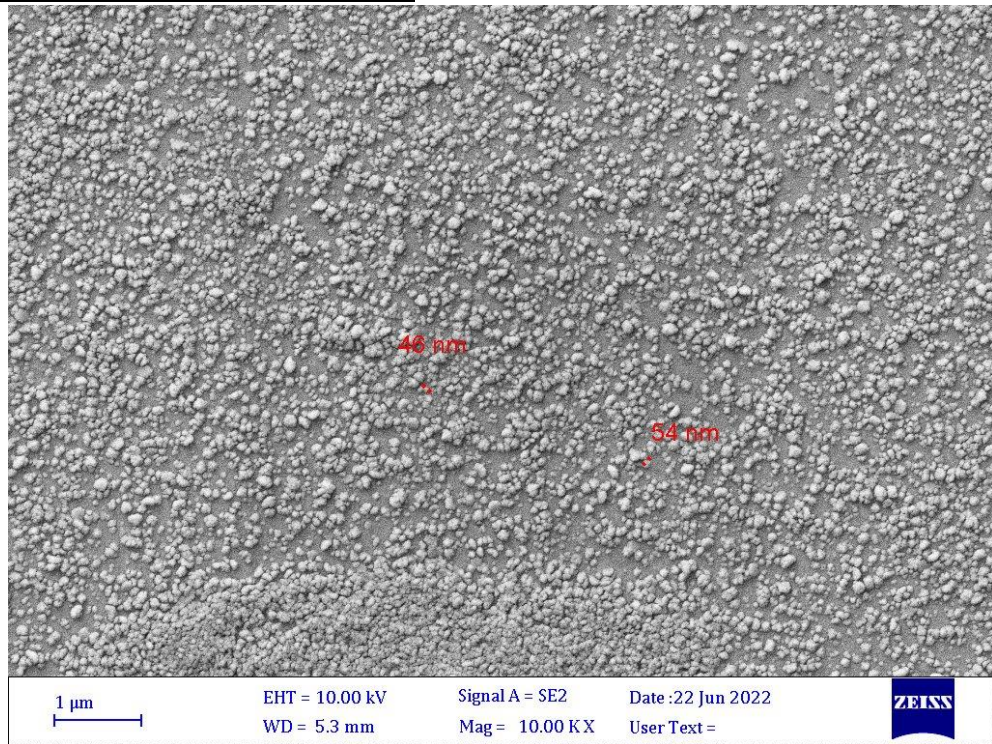


Figure 4-5d. The surface morphology of samples S₁.

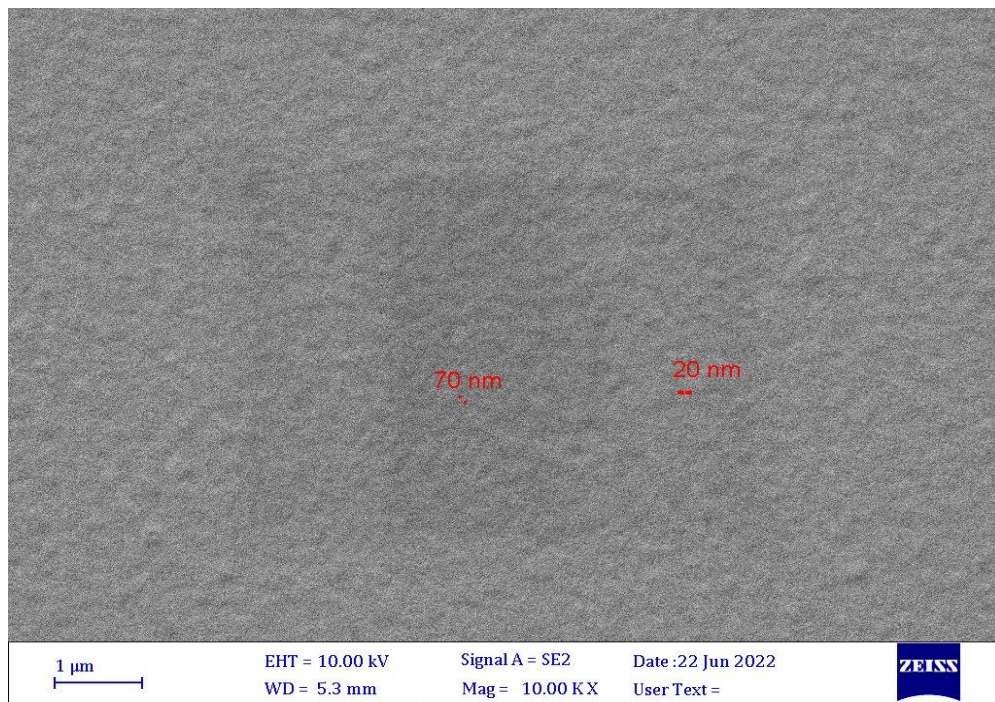


Figure 4-5e. The surface morphology of samples S₂.

Chapter 4: Results and discussion

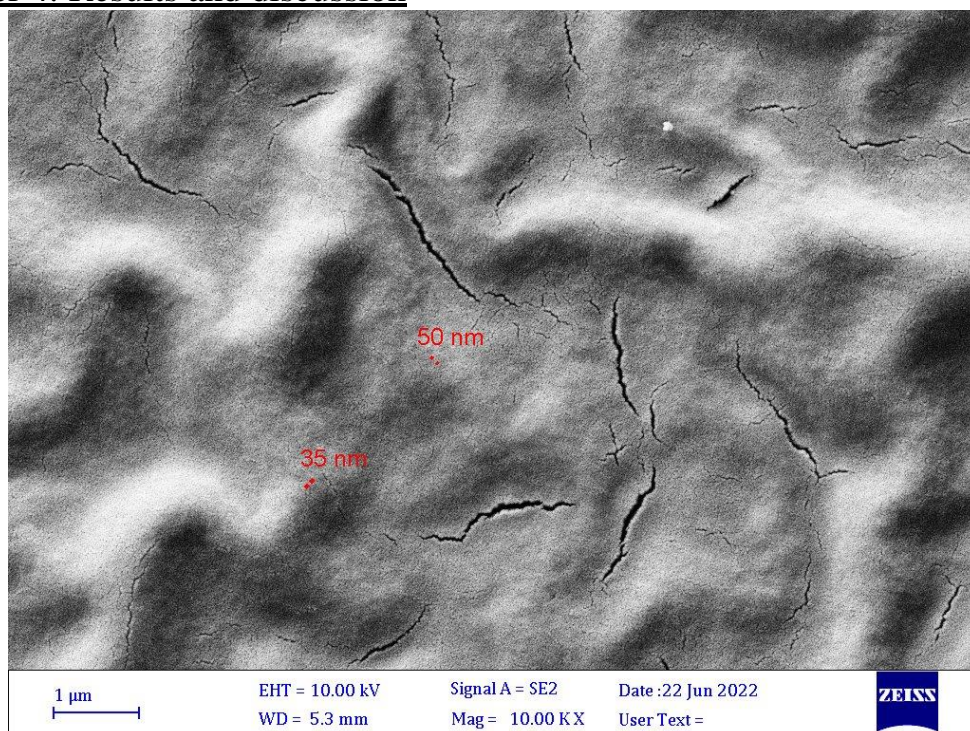


Figure 4-5f. The surface morphology of samples S₃.

While the crystal size from FESEM image were 33.85, 21.21, and 32 nm for samples S₁, S₂, and S₃ respectively as shown in figure 4-5 g, h, and i. This difference in the values from the XRD and FESEM values is due to implying that a grain possibly contained several crystallites.

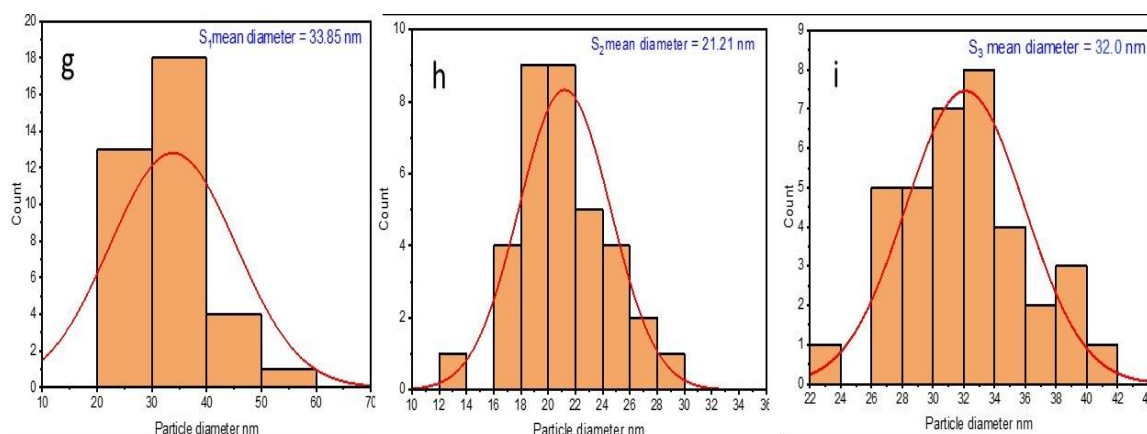


Figure 4-5g, h, i. Size distribution of particles diameter of samples S₁, S₂, and S₃ respectively.

To study the elemental characterization, purity and elemental distribution, EDS and mapping tests were investigated as shown in Figure 4-6. It could be noticed clearly that the prepared material exhibited high purity, hence no other elements rather than Zn and O were detected. A peak related to Au was also detected, which was assigned to coating the sample with gold for testing FESEM

Chapter 4: Results and discussion

and another peak was found in 3.35 KV related to substrate Sn. As well, the ratio of Zn to O was 53.4 to 46.6 in the single-layer Figure 4-6 S₁. Meanwhile, an increase in the percentage of Zn to O 75.2 to 24.8 when dipping cycles become two-layer sample Figure 4-6 S₂. Finally, in the three-layer sample, the percentage was 90 to 10 as shown in figure 4-6 S₃. These results indicated that the elemental composition and the oxides state were strongly affected by the number of dipping times and thus the thickness.

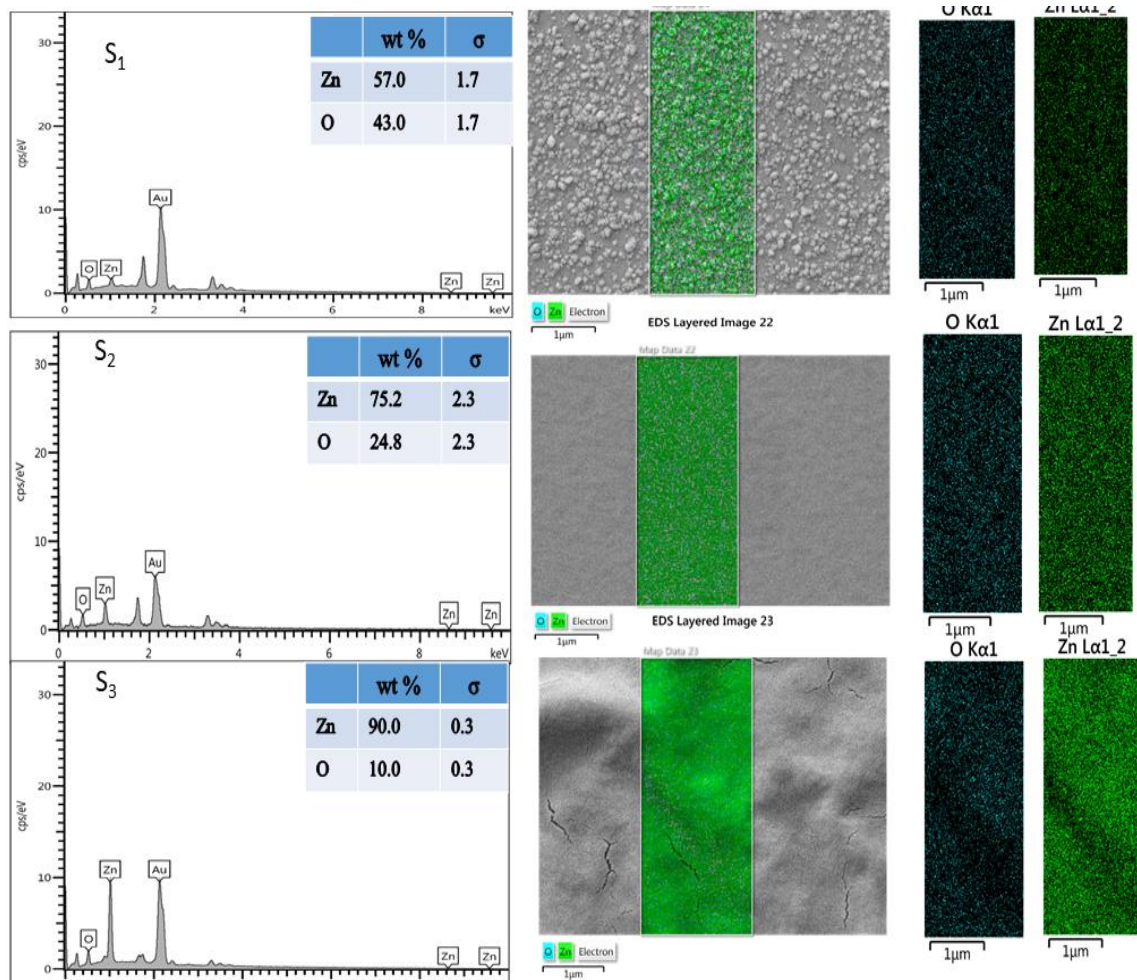


Figure 4-6. Mapping and EDS composition of samples S₄, S₅, and S₆.

4.2.2 ZnO NRs

Figure 4-7 shows FESEM cross section images a, b, c for S₄, S₅, and S₆ respectively. They displayed that the average thickness of the S₄ was 535 nm, while the thickness of S₅ was 692 nm. Nevertheless, the thickness of S₆ were 755 nm.

Chapter 4: Results and discussion

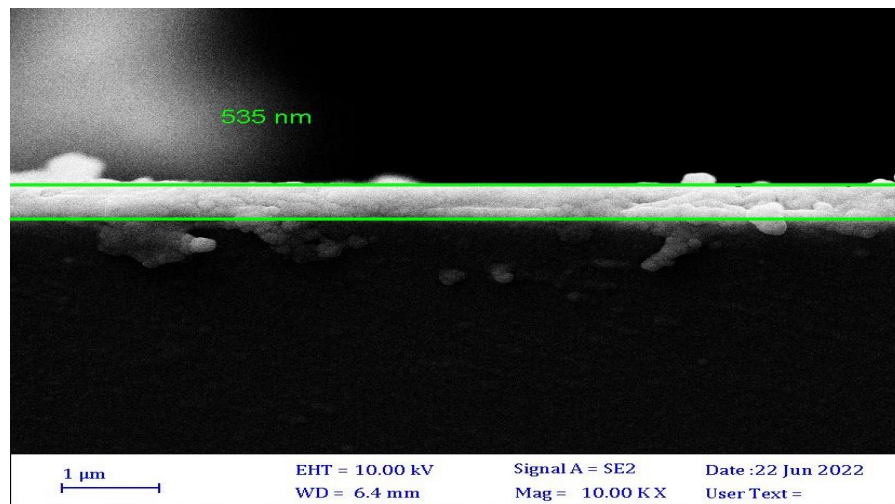


Figure 4-7a. The cross section of sample S4.

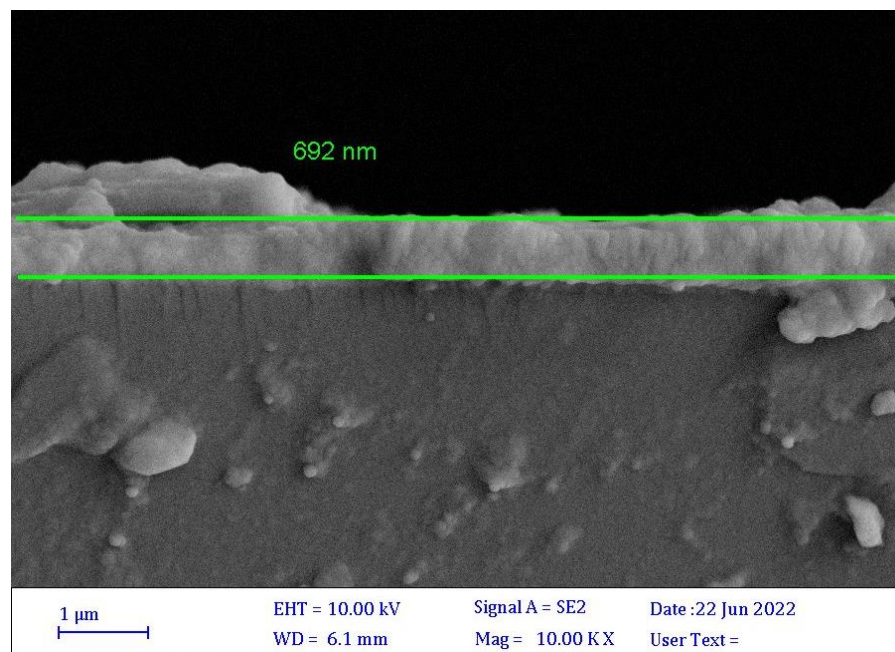


Figure 4-7b. The cross section of sample S5.

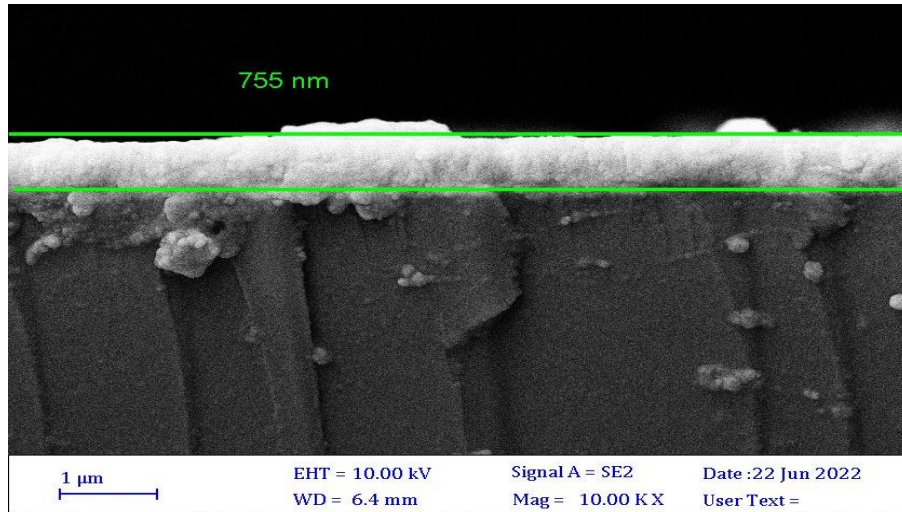


Figure 4-7c. The cross section of sample S₆.

As for the d, e, and f images show the top view of the S₄, S₅, and S₆, respectively, as these images show excellent coverage of ZnO NRs. As reported in previous study, these rods are assembled to form a hexagonal shape with a diameter ranging between 115-170 nm. The density of these ZnO NRs is due to the homogeneous distribution of the seed layer and also because of the value of $Ph = 7$ [128].

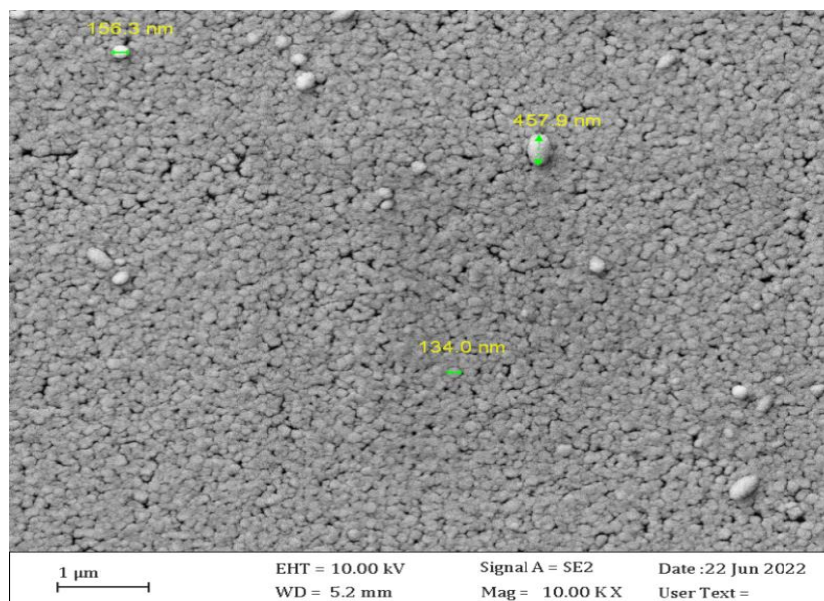


Figure 4-7d. Top view of homogenous distribution of sample S₄.

Chapter 4: Results and discussion

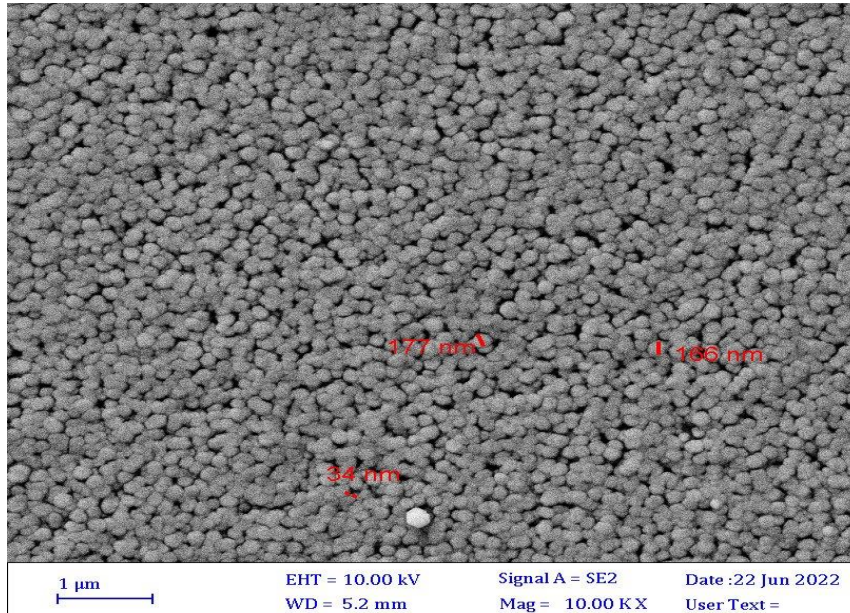


Figure 4-7e. Top view of homogenous distribution of sample S₅.

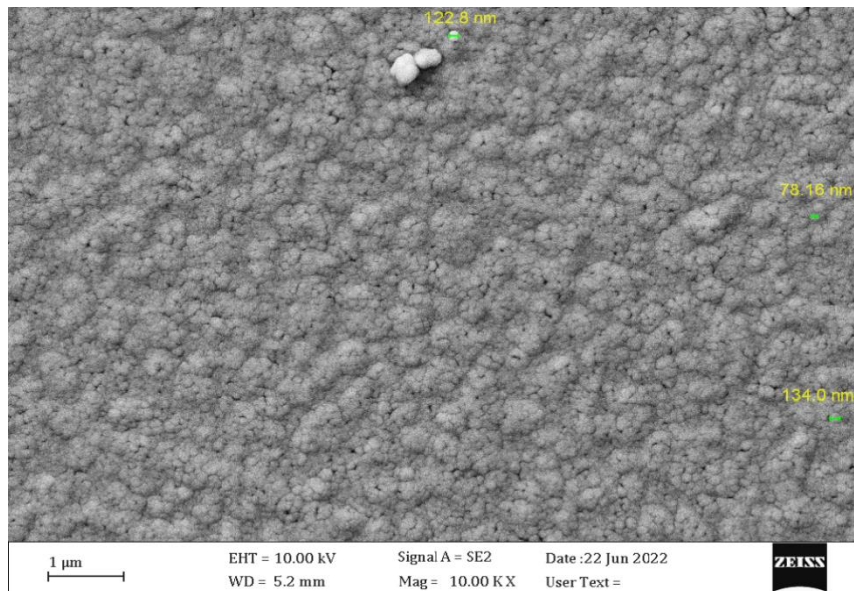


Figure 4-7f. Top view of homogenous distribution of sample S₆.

Figure 4-7 g, h and i represented the distribution of the average diameters of the nanorods that belonged to each thin film. As the average diameters of S₄ were 26.227 nm, S₅ were 49.81, and S₆ were 51.023 nm. These results show that by increasing the thickness of the seed layer, the diameter of the ZnO NRs was increased [129].

Chapter 4: Results and discussion

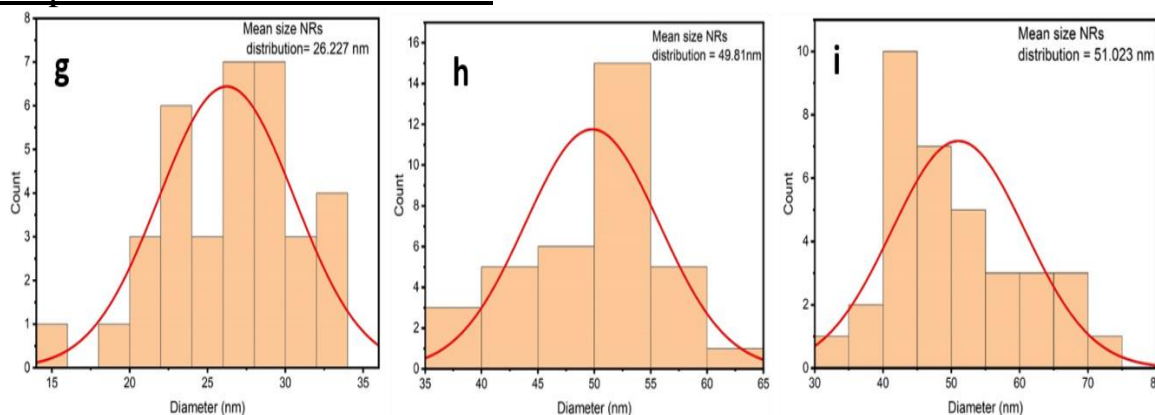


Figure 4-7g, h, i. The size distribution of particles diameter of S₄, S₅, S₆ respectively.

In order to investigate the purity and the elemental distribution of the ZnO NRs, EDS examinations were applied figure 4-8. As the number of seed layers increased, and thus the length of the nanorods enlarged, the concentration of oxygen increased and Sn peak disappear gradually as ZnO NRs has high absorbance and increasing in the thickness led to Sn far from the surface.

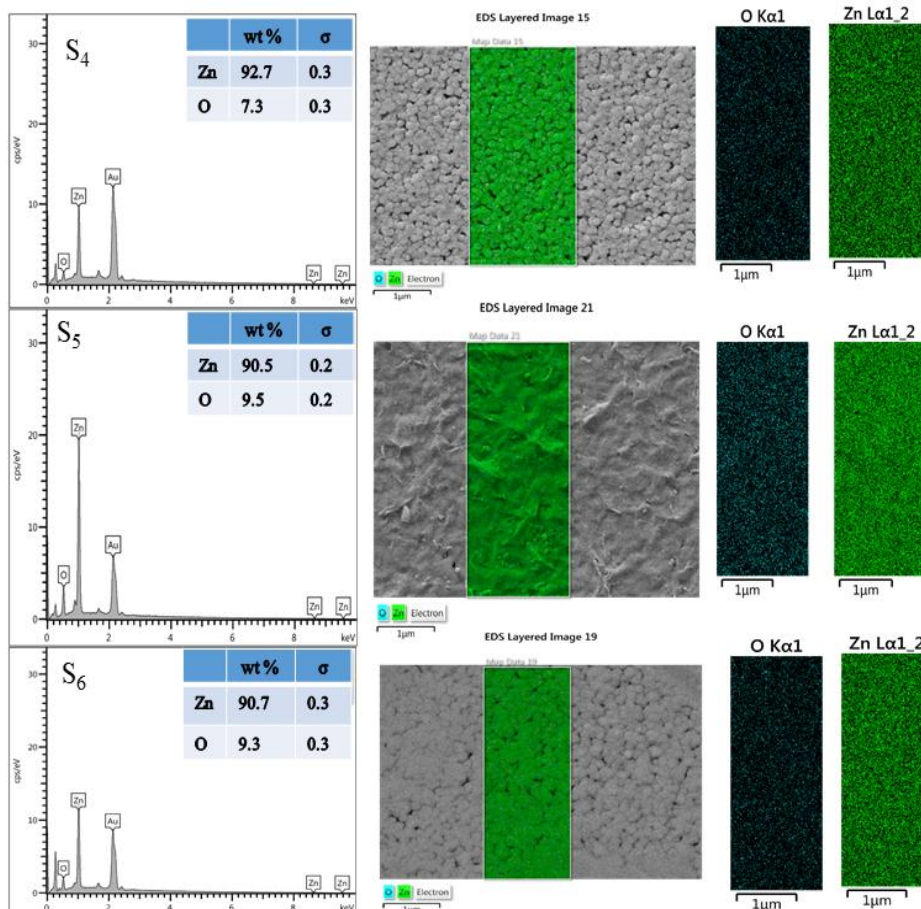


Figure 4-8. Mapping and EDS composition of samples S₄, S₅, and S₆.

Chapter 4: Results and discussion

4.2.3 ZnO NRs coated with Ag NPg

The surface morphology examinations of the prepared samples were carried out by FESEM. Figure 4-9 shows the surface morphology, cross-section, and size distributions. Figure 4-9 a, b and c, they denoted a cross section of the samples S₇, S₈ and S₉ correspondingly. These images show the variations in the length of the nanorods for samples as 380 nm, 466 nm, and 708 nm, respectively. The difference between these samples is the number of seed layers, the larger the number of seed layers, the greater the height of the nanorods.

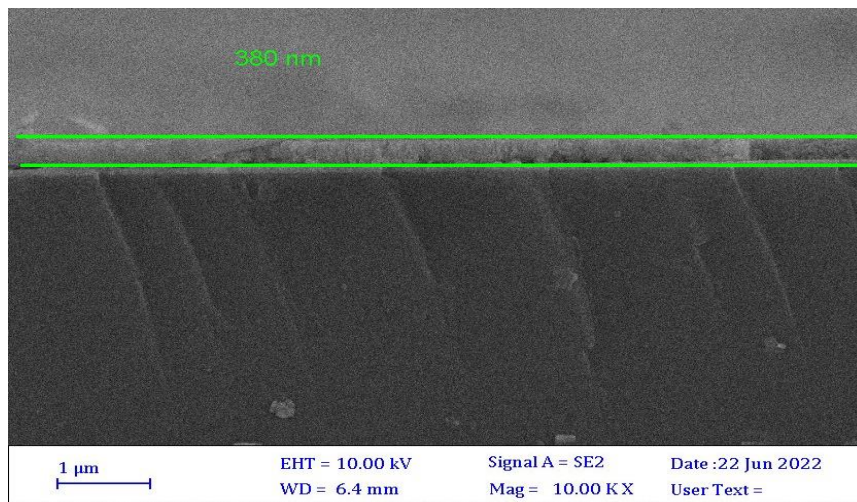


Figure 4-9 a. The cross-section of sample S₇.

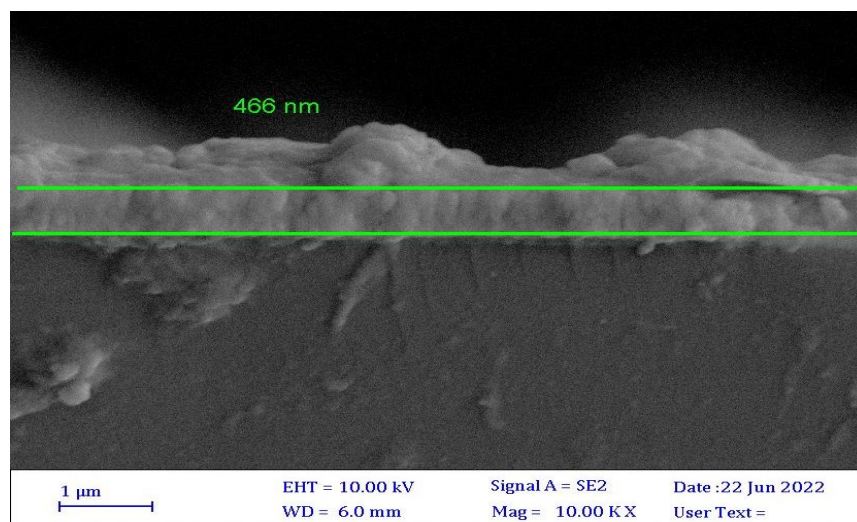


Figure 4-9 b. The cross-section of sample S₈.

Chapter 4: Results and discussion

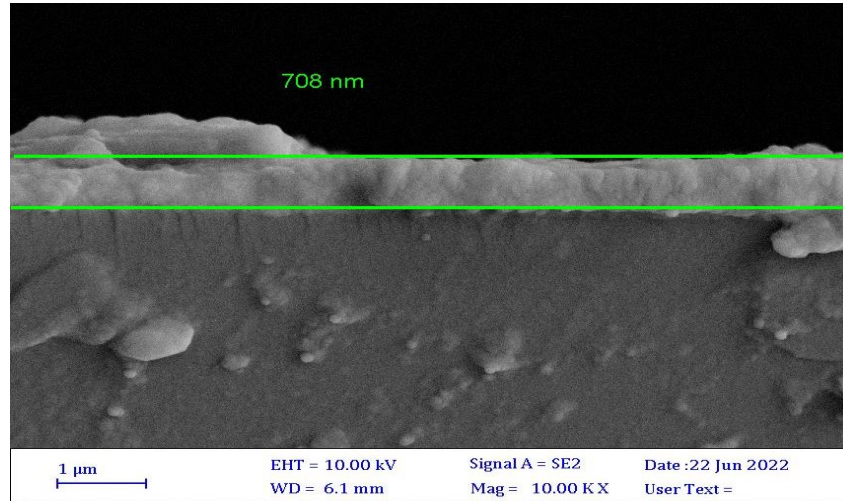


Figure 4-9 c. The cross-section of sample S₉.

As images 4-9 d, e and f represent the surface morphology of the samples S₇, S₈ and S₉, respectively. Generally, all the samples displayed small nanoparticles with an average size of around 20 - 40 nm. These nanoparticles agglomerated and stacked together to form larger hexagonal combined nanorods structures that were longitudinally aligned on the surface of the substrate. The ZnO nanorods were grown with flat feature surfaces of size ranging around 100, 120 and 150 nm for the samples S₇, S₈ and S₉, respectively. As well as, the diameter of the nanostructure increases due to its dependency on the size of the particles of the aggregate seed layer. By comparison, wider, longer and more upright nanorods can be created with thicker thin films. As well, the distance between adjacent nanorods shrunk as the seed layers became the thicker until the substrate was completely filled.

Chapter 4: Results and discussion

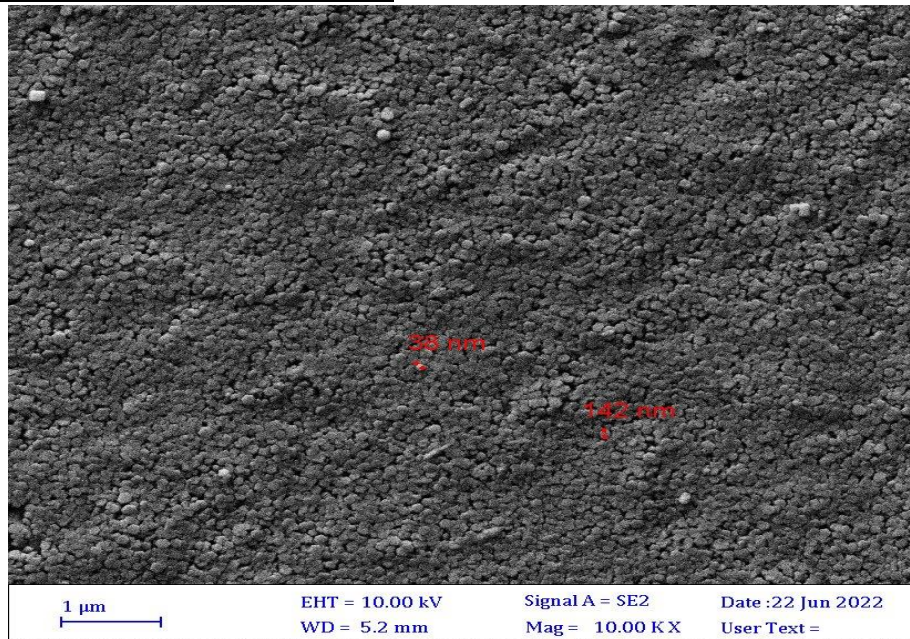


Figure 4-9d. Top view of homogenous distribution of sample S7.

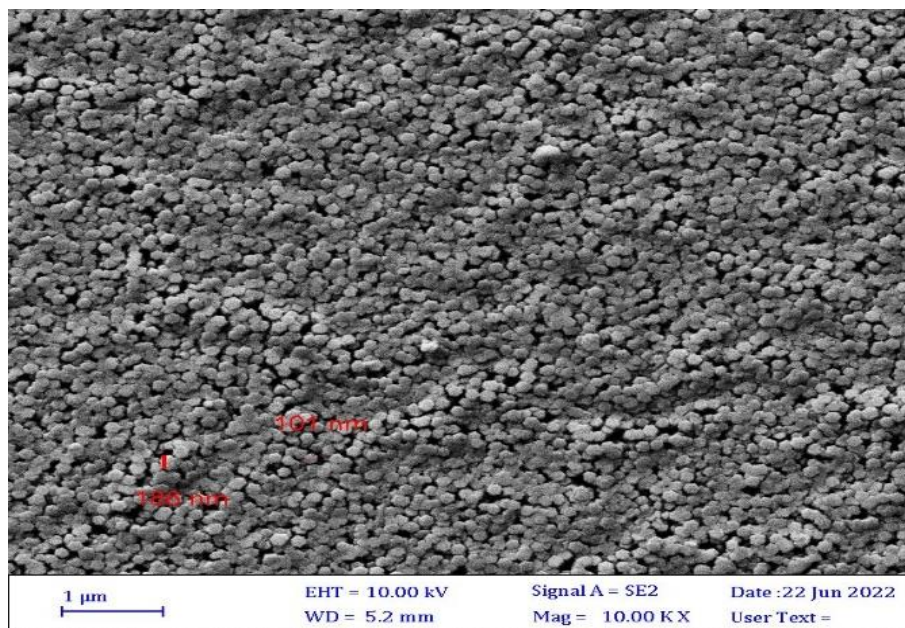


Figure 4-9e. Top view of homogenous distribution of sample S8.

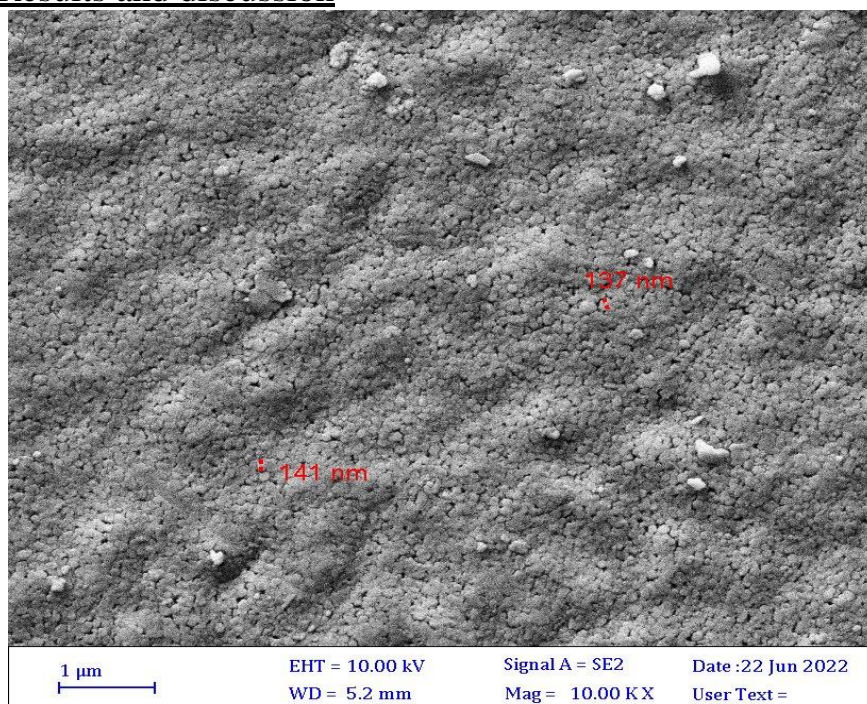


Figure 4-9f. Top view of homogenous distribution of sample S₉.

In addition, Figure 4-9 g, h, and i shows the distribution of nanorods diameters for each sample. As the statistical results, the diameters of samples S₇, S₈ and S₉ are 23.68, 27.5, and 33.95 nm, respectively. It can be noticed clearly, that the higher the number of dipping cycles and thus thicker seed layer, the largest the diameter.

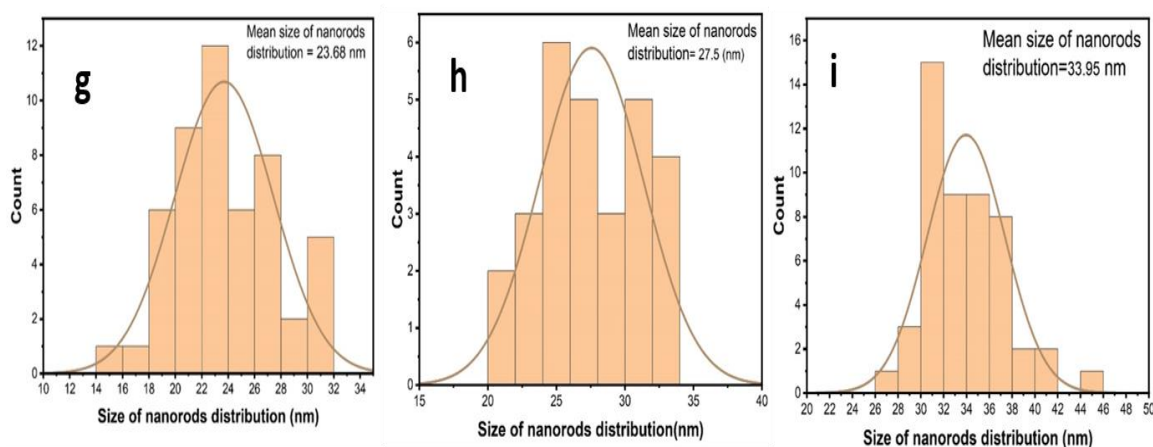


Figure 4-9g, h, i. The size distribution of nanorods diameter of sample S₇, S₈ and S₉ respectively.

Chapter 4: Results and discussion

Figure 4-10 illustrates the EDX and Mapping of the three samples S₇, S₈ and S₉ respectively. It is clear that the percentage of oxygen is low while the percentage of zinc is very high. Whereas silver does not appear in this examination because of the presence of oxygen vacancies, silver did not appear on the surface, but rather concentrated in the interfacial spaces of the nanorods. Additionally, the absence of the peak of Sn because of high absorbance of ZnO NRs and increased of thickness.

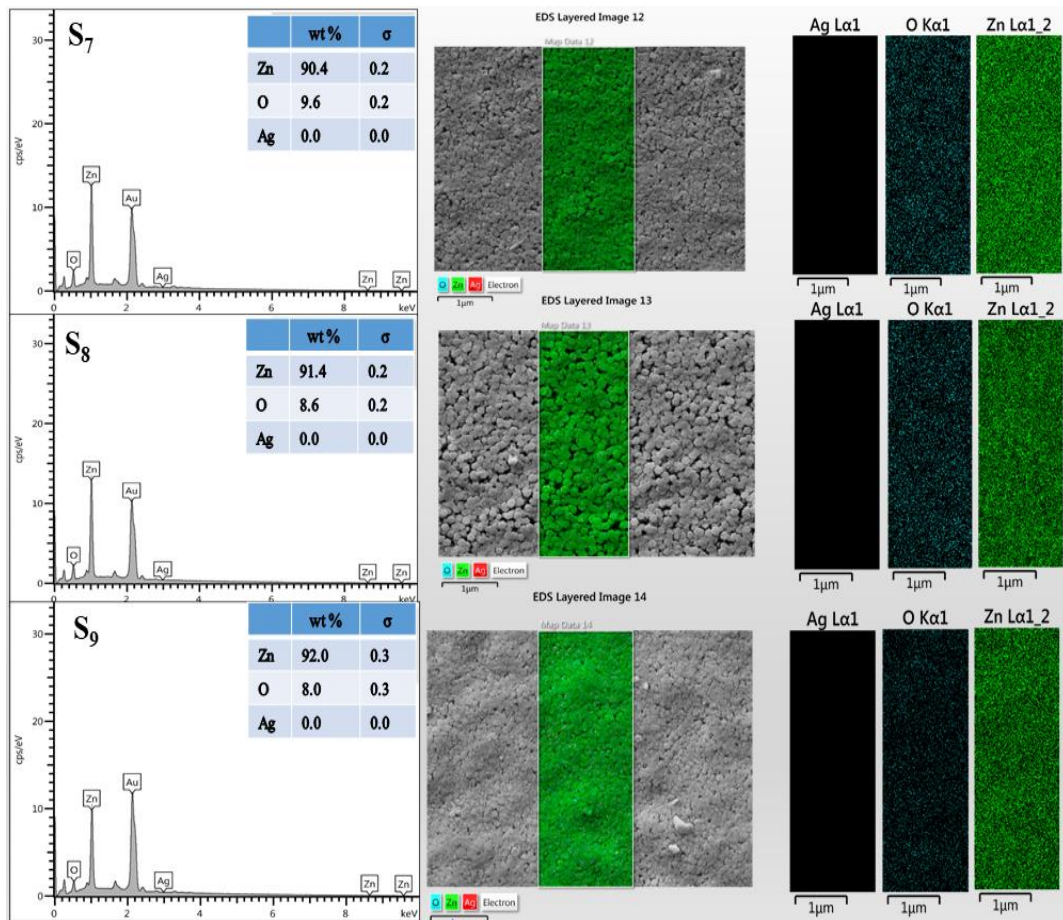


Figure 4-10. Mapping, and EDS composition for ZnO NRs coated by Ag NPs for samples S₇, S₈ and S₉.

4.3 Optical properties

4.3.1 ZnO Seed layer

The transparency of the deposited ZnO thin films was investigated as shown in Figure 4-11. The results revealed that the ZnO thin films have high transparency. These results indicated that these films are suitable for TCO applications.

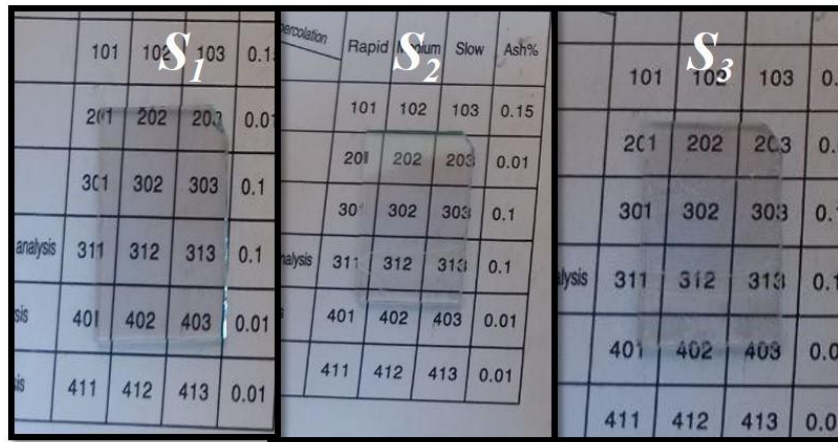


Figure 4-11 Photographs of transparent thin films seed layer S₁, S₂, and S₃.

One of the properties that was calculated is the energy gap of the thinfilm prepared using the relation between $E = h\nu$ eV and $(\alpha h\nu)^2$ (eV/cm)² as shown in figure 4-12. This figure shows that by increasing the number of coating times, increasing the thickness of the prepared thin film, the energy gap decreases. The one-layer sample was $E_g = 3.552$ eV, the two-layer sample was $E_g = 3.277$ eV, and the three-layer sample was $E_g = 3.229$ eV.

Chapter 4: Results and discussion

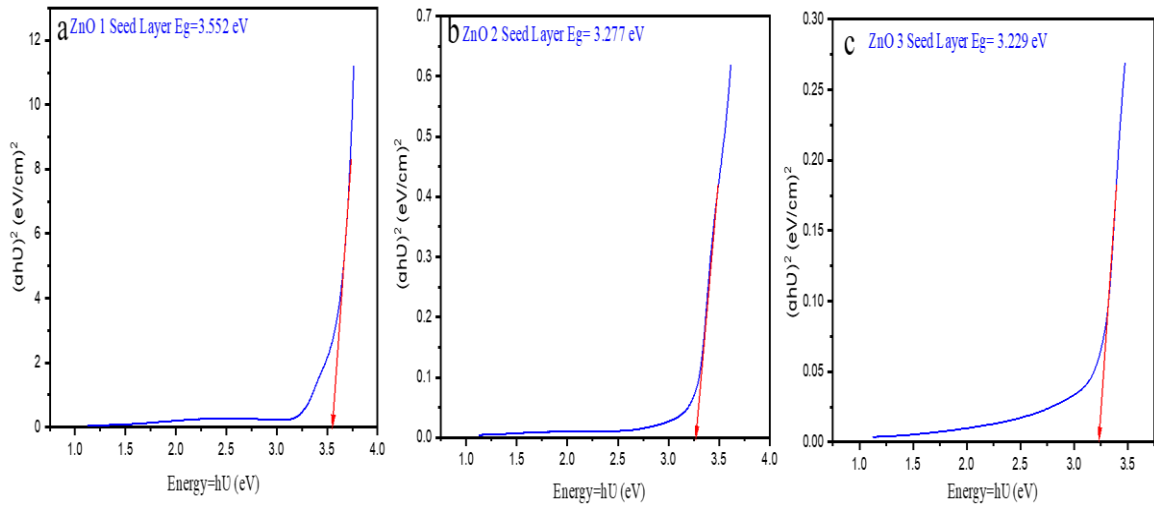


Figure 4-12. Energy gap of samples a) S₁, b) S₂, c) and S₃.

The optical transmittance of the prepared thin film was characterized. The results showed a high transparency around 80 – 87 % as shown in figure 4-13. Through examinations of the prepared samples, it is clear that at low wavelengths from 180 nm to 325 nm all samples have a low transparency which indicates high absorbance. At 325 nm, optical absorption edges were noticed clearly, which could be identified by the optical gap of ZnO. While, when the wavelength increased from 325 nm to 400 nm, the transparency begins to gradually increase during this range. Finally, when the wavelength accessed visible light and NIR area, transmittance increased up to 80-87 % ,this results higher than results obtained from [130]. Moreover, it is obvious that S₃ showed less transmittance than the rest of the other samples. This could be attributed to the number of dipping; hence S₃ was dipped three times which led to produce a thicker layer and then lower transmittance compared to other samples which were dipped once or twice. This finding indicated that this preparation method represents an exciting method for fabricating ZnO thin films with controlled thickness.

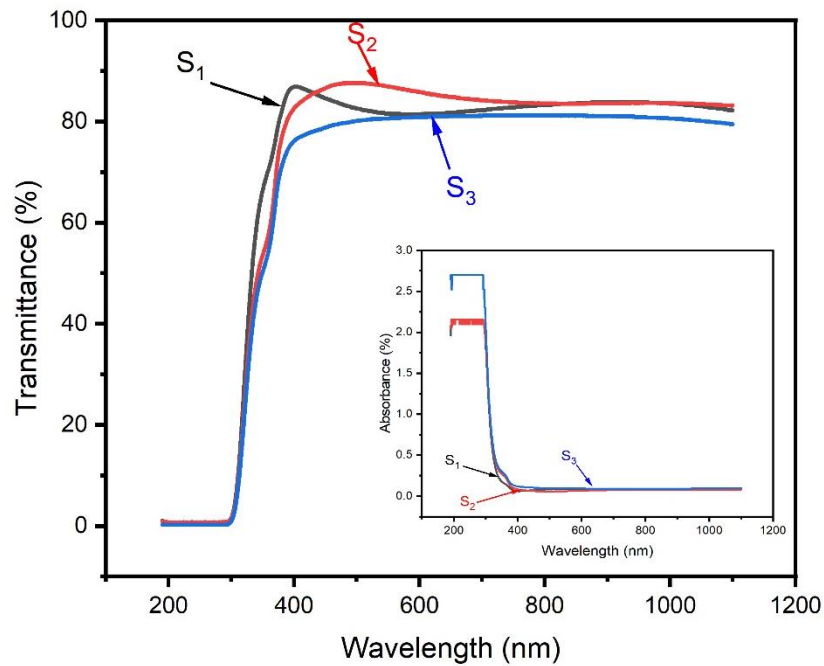


Figure 4-13. UV – Vis characterization of the prepared ZnO thin films for S₁, S₂, and S₃.

4.3.2 ZnO NRs

Figure 4-14 displays the images of ZnO thin films on ITO glass. The photographs prove the transparency of the prepared ZnO NRs in which sample S₄ showed high transparency while the transparency reduced till it become semi-transparent for sample S₆.

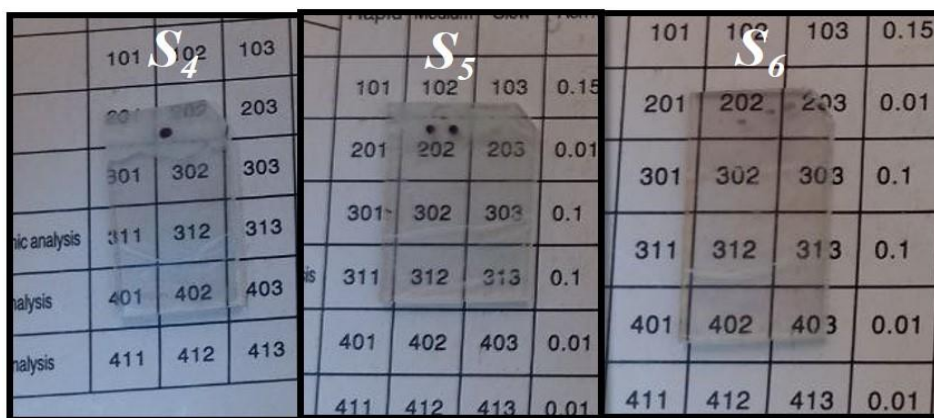


Figure 4-14. Photographs of transparent ZnO NRs thin films S₄, S₅ and S₆.

The optical measurements (transmittance) using UV/Vis spectroscopy of the ZnO NRs were made at room temperature as shown in figure 4-15. The

Chapter 4: Results and discussion

results showed that the action of growth of NRs reduced the transmittance of the prepared samples and this is obvious, due to the increase of excited electrons, which led to an increase in absorption and a decrease in transmittance. Sample S_6 represented the highest absorbance of this group because of the ZnO NRs length 755.55 nm, which amounted to 62%. After the wavelength of 550 nm, these three samples showed a sharp increment in the transmittance up to 75, 70 and 61% respectively. This results were compatible with [131].

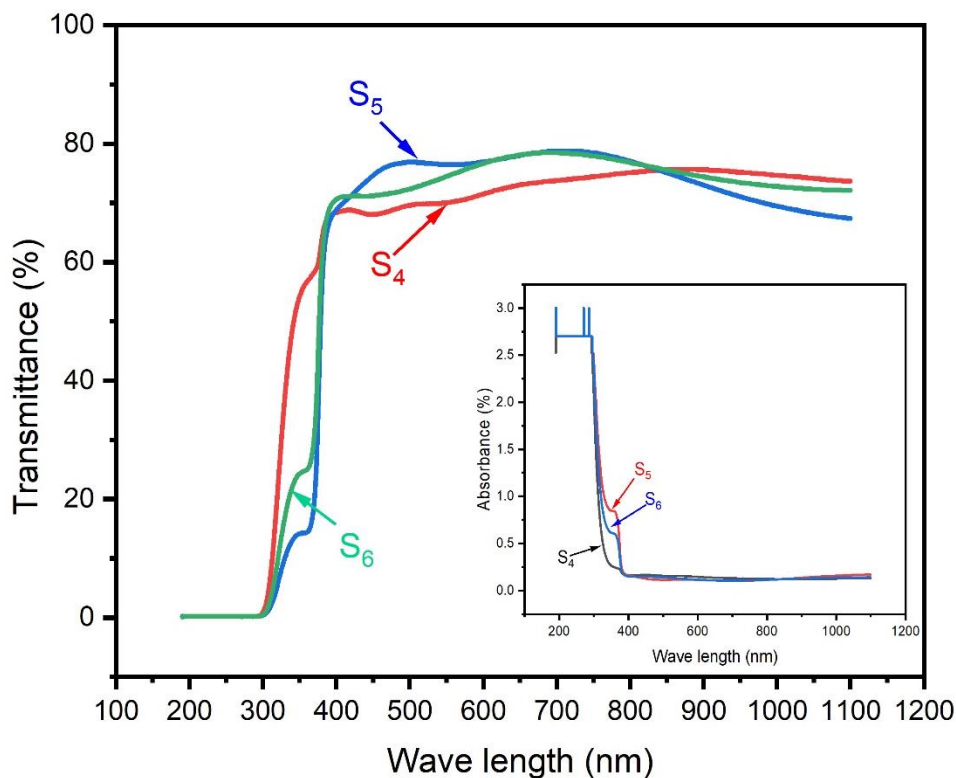


Figure 4-15. UV – Vis characterization of the prepared ZnO NRs thin films for S_4 , S_5 , and S_6 .

Figure 4-16, shows the energy gap of the prepared samples S_4 , S_5 and S_6 . It could be noticed that the energy gap decreased with the increment of the length of the ZnO NRs (the thickness of the thin films). As the thickness of the thin film increases, the transmittance of the light beam usually decreases and shifts towards the higher wavelengths, and thus the optical absorption edge shifts towards the higher wavelengths (the lower photon energy), and as a result, the optical gap energy decreases. The results showed that the value of the energy gap of S_4 was $E_g = 3.275$ eV, for S_5 $E_g = 3.236$ eV, while the value of the energy

Chapter 4: Results and discussion

gap was $E_g = 3.169$ eV for S_6 . In this context, the energy gap value can be controlled by controlling the thickness of the prepared thin films and this results compatible with previous work [132].

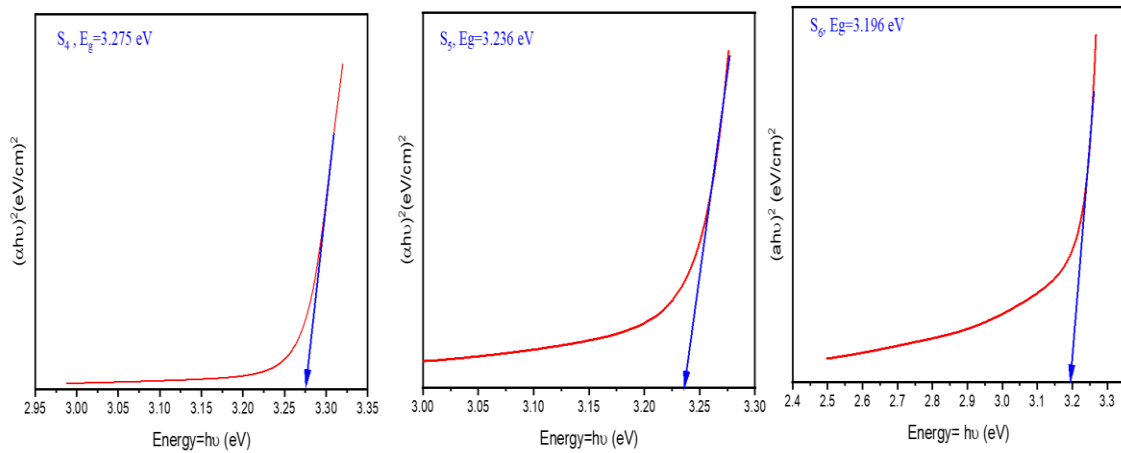


Figure 4-16. Energy gap for S_4 , S_5 , and S_6 .

4.3.3 ZnO NRs coated with Ag NPs

The prepared ZnO NRs coated by Ag NPs show high transparency, as shown in figure 4-17. The results showed high transmittance in the visible to a near-infrared range of all samples with some variation in values due to the number of seed layers for each thin film. The transmittance increases sharply in the wavelength region of 300 nm, where it reaches 70%, and the value rises to 80%. Nevertheless, the higher the number of layers and thus longer nanorods, the lower the optical transmittance.

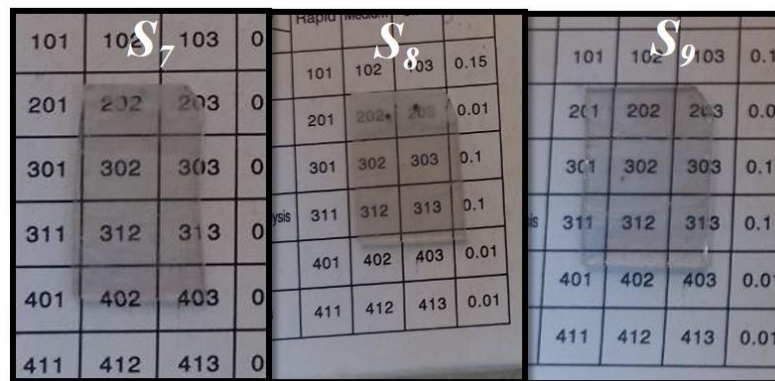


Figure 4-17. Photographs of transparent thin films ZnO NRs coated by Ag NPs for S_7 , S_8 , and S_9 .

Chapter 4: Results and discussion

The optical characterization of thin films provides information about physical properties such as bandgap energy, band formation, and optically active defects. The optical transmittance and energy gap values are affected by the thickness of the film as the transmittance decreases sharply in the ultraviolet region due to the high absorption in the energy gap. As expected, the transmittance decreases with the increasing thickness of the film because many more photons are absorbed into the material by increasing thickness. In addition, sharp transmittance edges appeared in all the samples that showed a red shift towards the lower energies and larger wavelength. This blue shift is proportion directly to the length of the nanorods.

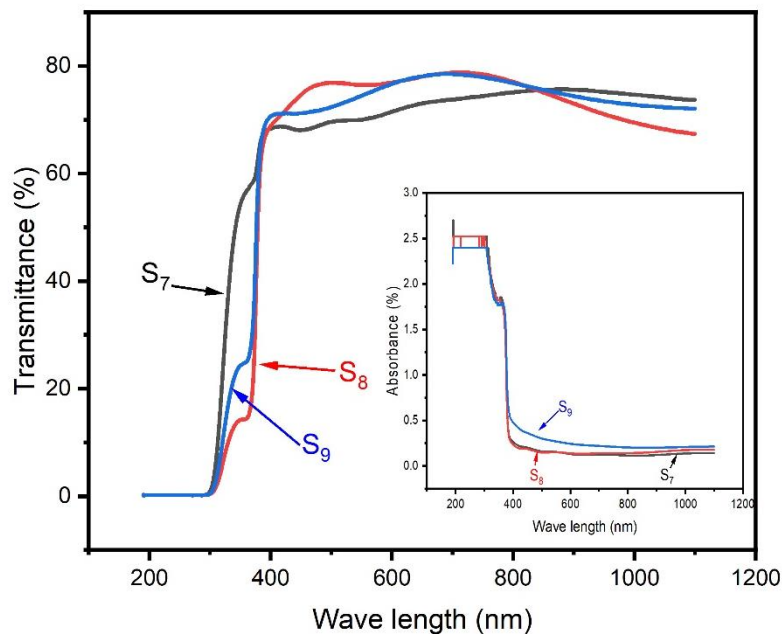


Figure 4-18. Optical Properties for ZnO NRs coated by Ag NPs for samples S₇, S₈, and S₉.

As shown in figure 4-19 it is clear that the energy gap decreases with increasing the number of coating layers of the sample, in other words, the energy gap decreases with increasing thickness of the thin film. In addition, the energy gap decreases when doping with Ag NPs.

Chapter 4: Results and discussion

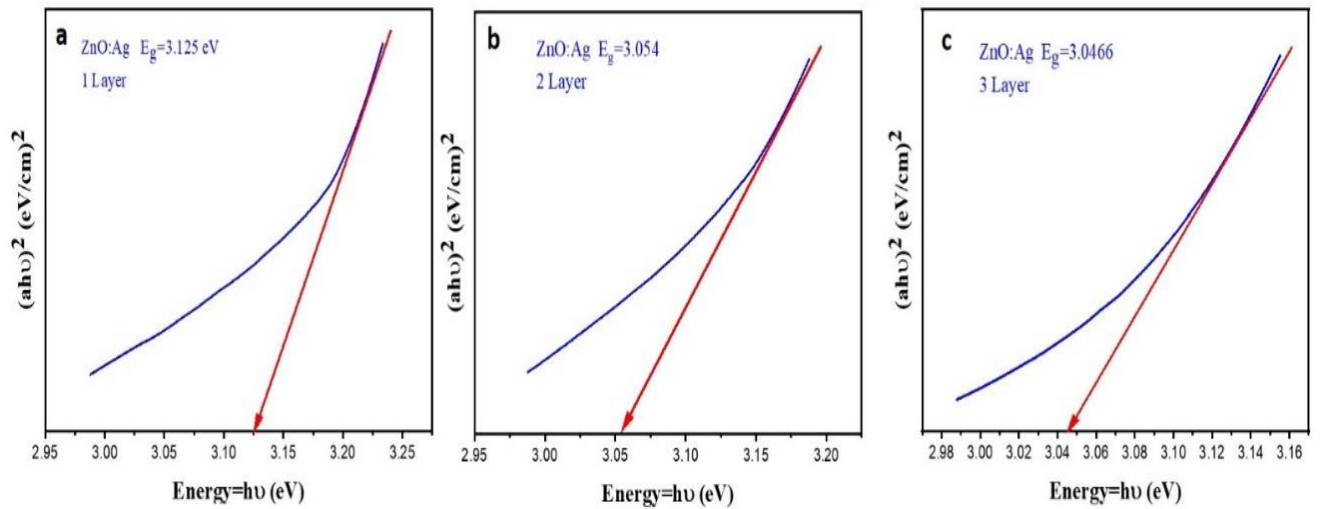


Figure 4-19. Energy gap for ZnO NRs coated by Ag NPs for samples S7, S8, and S9.

4.4 Electrical properties

4.4.1 ZnO Seed layer

I-V properties of ZnO thin films deposited on the ITO substrate were tested by measuring the voltage resulting from applying a variable current. The results confirmed that all the prepared thin films exhibited Ohmic properties as shown in figure 4-20. The sheet resistance of S₁ and S₂ was not totally linear which indicated that the seed layer is not homogeneously covered the surface. Meanwhile, for S₃ the sheet resistance increased linearly which displayed that the prepared thin film was homogeneous. Assuming that all other parameters remain constant, the sheet resistance is directly proportional with the film thicknesses. In this work, the sheet resistance is inversely proportional to the thickness as illustrate in table 4-4. This is due to the fact that more dipping cycles lead to higher thickness. In another hand, samples S₁ and S₂ exhibited less thickness than sample S₃ with inhomogeneous film. The un-continued film has uncovering parts that act as resistance, which rise the sheet resistance.

Chapter 4: Results and discussion

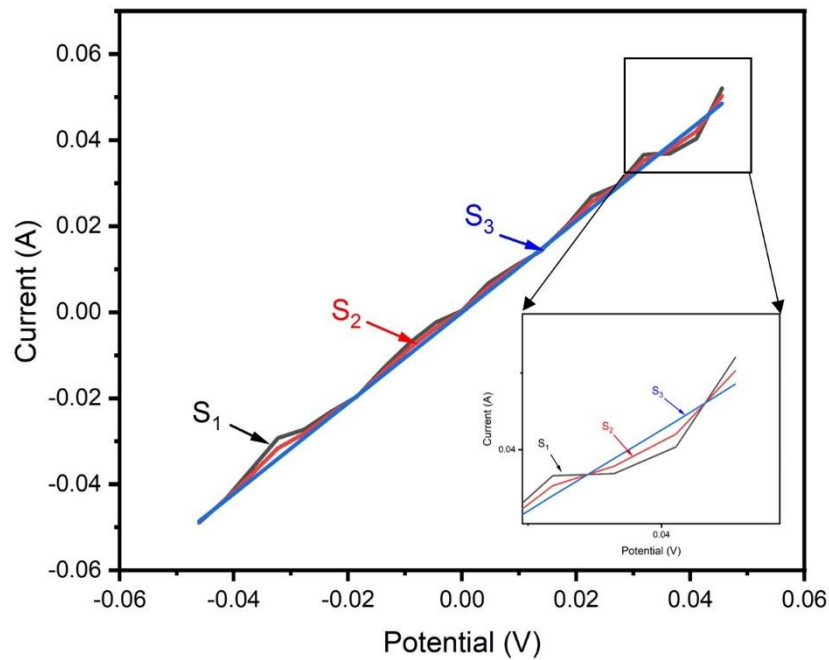


Figure 4-20. I-V characterization for S_1 , S_2 , and S_3 .

Table 4-4. Four Point Probe Method sheet resistance for samples S_1 , S_2 , and S_3 with varying dipping cycles.

Sample ID	R_s (Ω)(Eq.3-11)	R_{ss} (Ωsq^{-1})(Eq.3-12)
ITO	4.583	18.372
S_1	4.858	19.477
S_2	4.824	19.339
S_3	4.790	19.202

Through the electrical examinations of the three samples, and by increasing the number of coating times, we notice an improvement and regularity in the electrical properties and a decrease in resistance as shown in

Chapter 4: Results and discussion

table 4-4. The mobility of the carrier, which is affected by the crystalline and nanostructure of the polycrystalline material, was thought to explain this phenomenon. The increment in the resistivity depends on the crystallinity, thickness and grain size. With the dip coating approach, it can possibly build up more and more layers to reduce the sheet resistance.

4.4.2 ZnO NRs

The electrical properties of the prepared ZnO NRs were shown in figure 4-21. The linear relationship was an indication of its Ohmic properties. It was noticed that the higher the length and larger diameter of the nanorods, the better their conductivity and thus lower resistivity. The sample S₆ showed the best electrical properties due to its high length of NRs. Table 4-5 showed the gradual decrement in the resistance values by increasing the length of nanorods. As compare the effects of precursor concentrations ranging from 0.01 M to 0.1 M on crystal formation, alignment, optical, and electrical properties, the precursor concentration had a significant impact on the ZnO nanorods' well-aligned orientation and maximum aspect ratio [133].

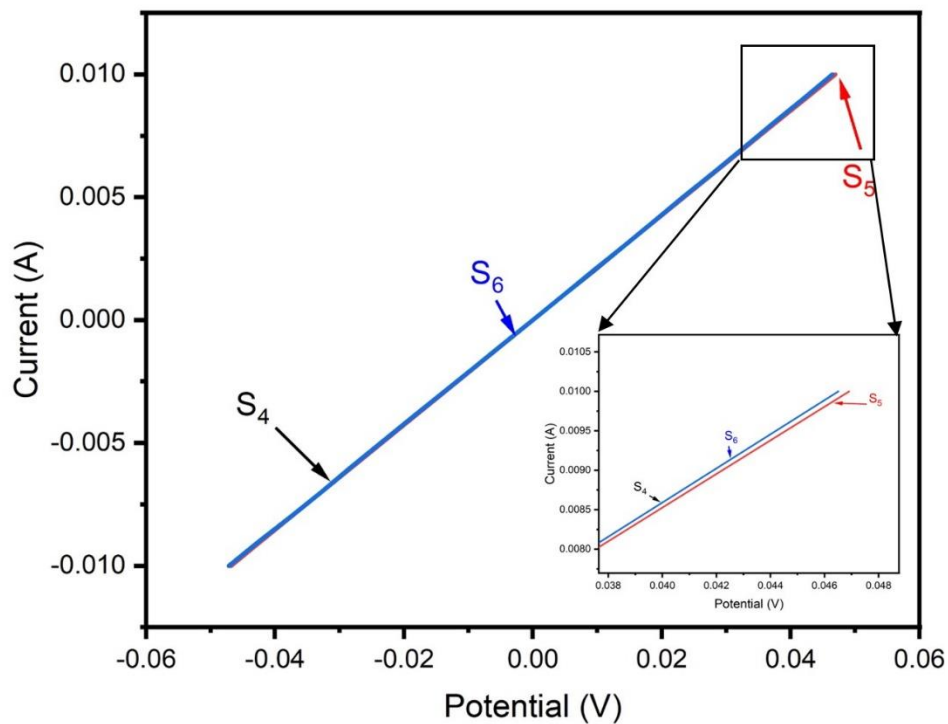


Figure 4-21. I-V characterization of S₄, S₅, and S₆.

Chapter 4: Results and discussion

Table 4-5. Four point probe method sheet resistance for samples S₄, S₅, and S₆ with varying dipping cycles.

Sample ID	R _s (Ω)(Eq.3-11)	R _{ss} (Ωsq ⁻¹)(Eq.3-12)
ITO	4.583	18.372
S ₄	4.744	19.021
S ₅	4.737	18.988
S ₆	4.725	18.943

4.4.3 ZnO NRs coated with Ag NPs

Figure 4-22 shows the electrical properties of ZnO NRs coated by Ag NPs. The linear relationship suggests that all of the ZnO thin films coated by Ag NPs have an Ohmic characteristic. Generally, the results show that sample S₉ exhibited the best conduction, it was found that the electrical properties improved by increasing the thickness, growing the diameters of nanorods and coated by Ag NPs. This results caused by the nature of the nanorods structure which controls the path of electrons in a specific direction, so the conduction speed increases, which gives a positive indication of the decrease in the resistance of the thin film. As well, coated by Ag NPs improves the electrical conductivity due to the abundance of electrons in which they participate in the thin film's conduction. Table 4-6 illustrates decreasing resistance values with increasing the number of seed layer and coated by Ag NPs, the optimum sample was S₉

Chapter 4: Results and discussion

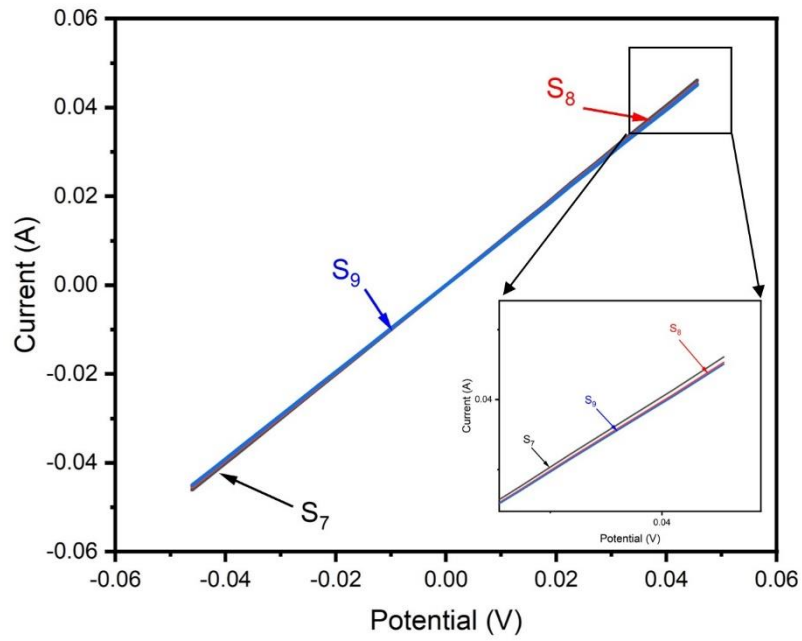


Figure 4-22. I-V characterization for S₇, S₈, and S₉.

Table 4-6. Comparison of FPP method sheet resistance for ZnO NRs samples of varying dipping cycles and coated by Ag NPs.

Sample ID	R_s (Ω)(Eq.3-11)	R_{ss} (Ωsq^{-1})(Eq.3-12)
ITO	4.583	18.372
S ₁	4.858	19.477
S ₂	4.824	19.339
S ₃	4.790	19.202
S ₄	4.744	19.021
S ₅	4.737	18.988
S ₆	4.725	18.943
S ₇	4.609	18.476
S ₈	4.535	18.182
S ₉	4.505	18.060

4.5 Cyclic voltammetry properties

4.5.1 ZnO NRs

Cyclic voltammetry measurements were made in the absence and presence of glucose using the manufactured electrode ZnO NRs coated by Ag NPs as a working electrode, the reference electrode is Ag/AgCl and the auxiliary electrode is Pt electrode. These electrodes were used as the basis of the interaction between the enzyme and glucose. The scanning rate was 50 mV s^{-1} and the voltage range was -1.00 to 1.00 V . The concentration difference of glucose was studied for the three samples with a difference in the number of seed layers. The enzyme was coated on the prepared electrode electrochemically, where its properties are described by cyclic voltammetry in Phosphate buffer saline (PBS) solution. This medium is one of the best options for studying the electrochemical enzymatic reaction. S_4 , S_5 and S_6 initially, were measured with very low concentrations, starting from $1 \text{ }\mu\text{M}$ and continuing to $500 \text{ }\mu\text{M}$. At low concentrations, no response could be recorded. After increasing the concentration to 1 mM , the samples responded to the applied voltage as shown in figure 4-23. The three samples S_4 , S_5 , and S_6 showed a partial response to the redox reactions in terms of the exchange of electrons between the enzyme reaction with glucose. The track trace shows a small amount of the reaction, in other words, a lesser range of the interaction, and this is due to the lack of surface electrons participating in the process of electron transfer resulting from the oxidation and reduction reaction between the biological element and glucose. Also, the reduced surface area due to the high density of the ZnO NRs led to a lower reaction product than expected. Figure 4-24 represents the relationship between the values of the current measured when the glucose concentration changed for the three samples. A discrepancy is observed in the sensitivity values, detection limit and linearity as shown in table 4-7. Therefore, these variables must be improved by doping with silver nanoparticles.

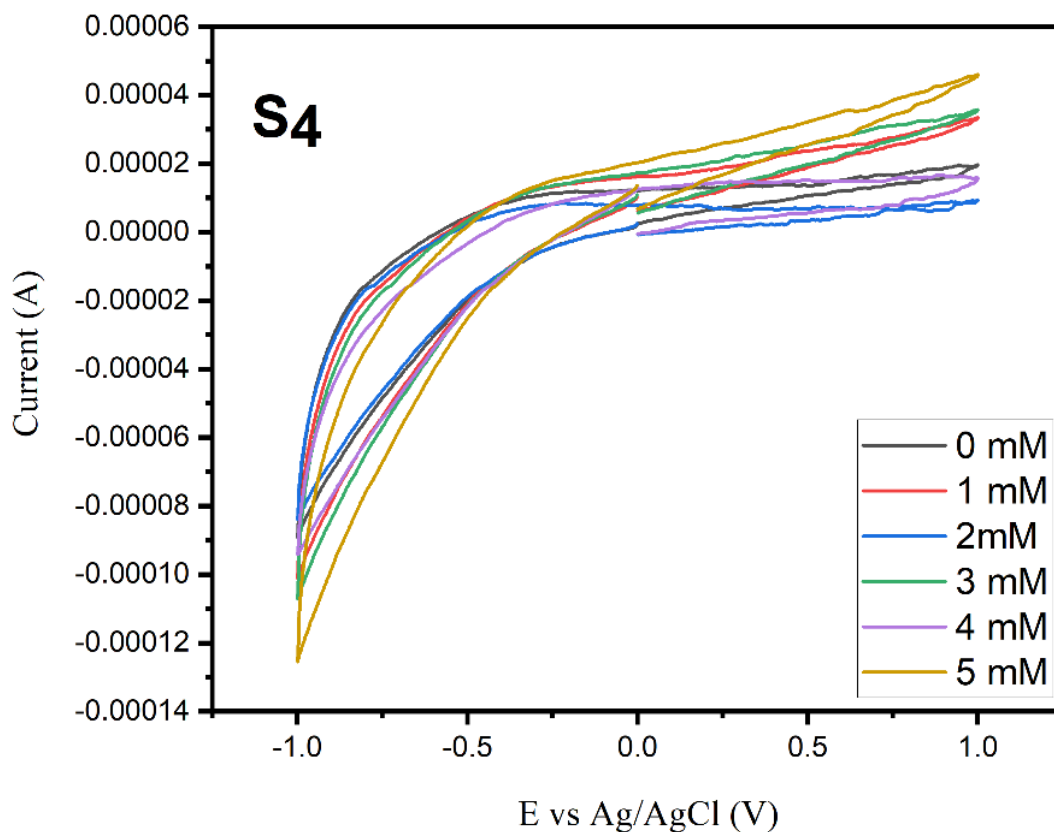


Figure 4-23a. Cyclic voltammograms of the ZnO NRs coated by Ag NPs in the presence of glucose of 0 mM- 5 mM in PBS with a scan rate of 50 mV s^{-1} of sample S4.

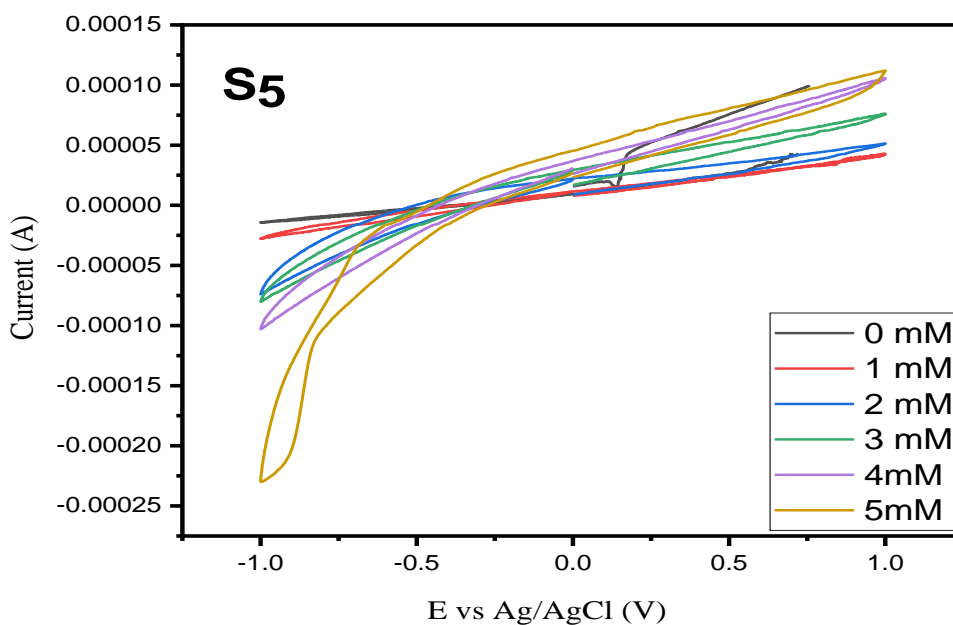


Figure 4-23b. Cyclic voltammograms of the ZnO NRs coated by Ag NPs in the presence of glucose of 0 mM- 5 mM in PBS with a scan rate of 50 mV s^{-1} of sample S5.

Chapter 4: Results and discussion

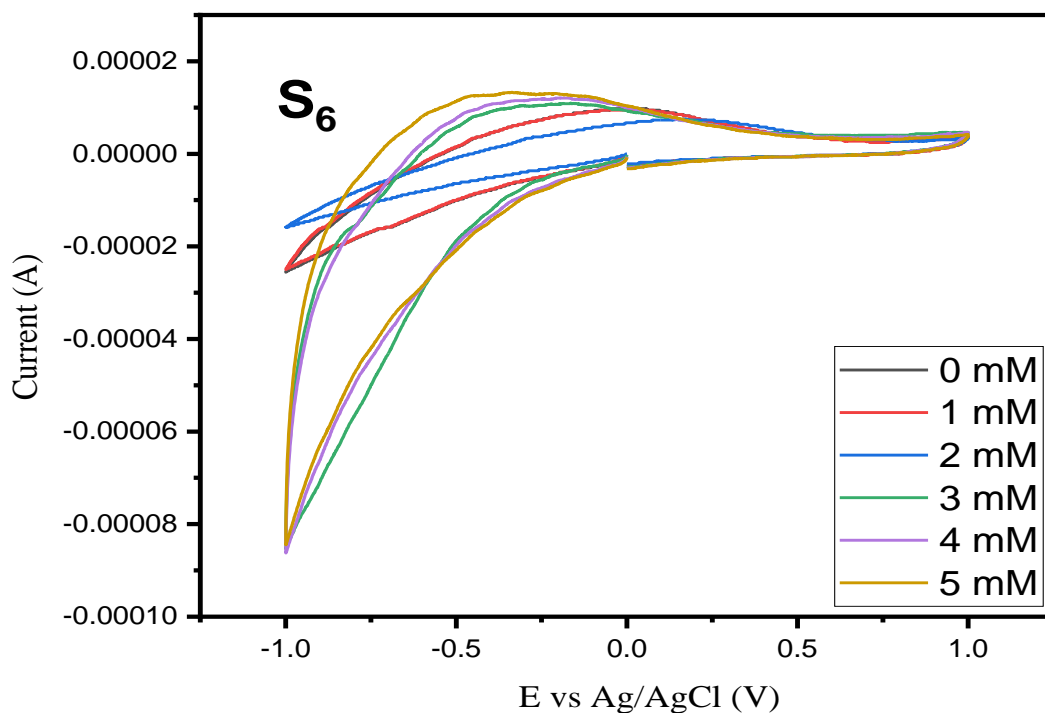


Figure 4-23c. Cyclic voltammograms of the ZnO NRs coated by Ag NPs in the presence of glucose of 0 mM- 5 mM in PBS with a scan rate of 50 mV s^{-1} of sample S_6 .

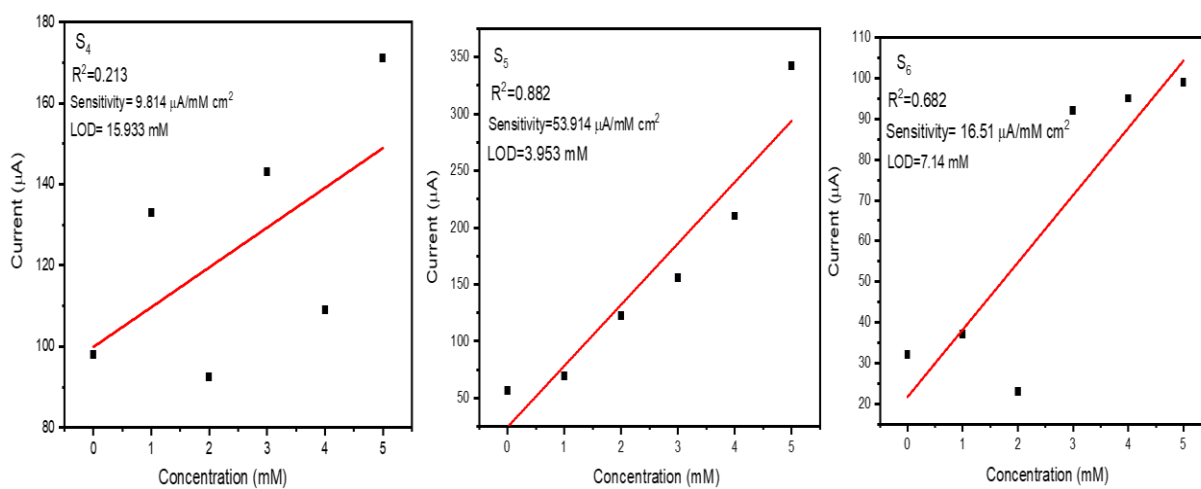


Figure 4-24. Increments of current as a function of glucose concentration for samples S_4 , S_5 , and S_6 .

Chapter 4: Results and discussion

Table 4-7. Varying in data obtained from cyclic voltammetry data for samples S_4 , S_5 , and S_6 .

Sample ID	R^2 (from linearity)	Sensitivity $\mu\text{A}/\text{mMcm}^2$ (Eq.3-17)	LOD mM (Eq.3-18)
S_4	0.213	9.814	15.933
S_5	0.882	53.914	3.953
S_6	0.682	16.51	7.14

4.5.2 ZnO NRs coated with Ag NPs

The same approach used in measuring the cyclic voltammetry of samples S_4 , S_5 , and S_6 was followed in the measurements of samples S_7 , S_8 and S_9 . The results presented in figure 4-25 showed an improvement in the values of resulting current for sample S_9 . The lower the ratio of silver coated the sample, giving the number of electrons compatible with the conductive voltammetric properties of the sample. It was found that the best doping rate is 0.001 M, as shown in figure 4-18 resulting from the analysis of XRD data using the X'Pert program. Figure 4-25 shows relation between applied voltage (E vs Ag/AgCl) and resulting current from the reaction between the GOx immobilized on the surface of the electrode, the increment of the trace track in the plot with the increase in the number of coating layers for the samples in which the reaction takes place in terms of oxidation and reduction. Cyclic voltammograms of coated and ZnO NRs samples in 0.1 M PBS are shown in figure 4-25. At the ZnO/ITO electrode, a low oxidation current existed. Coated ZnO NRs samples showed an important redox peak, which enhanced and shifted toward a lower potential as the Ag NPs content decreased. These enhanced peak current and potential shift were attributed to the improved conductivity and electrocatalytic properties due to the Ag NPs coating. Interestingly, the electrocatalytic activity of the prepared electrode was noticeably different from the others. It showed a strong and well-defined redox peaks. The increased current density occurred

Chapter 4: Results and discussion

because of the charge carriers approaching the conduction band of ZnO, which could be involved in the charge transfer at the metal oxide/electrolyte interface [61]. From this observation, the decrease in coating with Ag NPs concentration provided a higher electrical conductivity, faster electron transfer kinetics, and excellent electroactive surface area, thereby improving the electrochemical response [134]. The better the performance of the manufactured electrode was for lower ratio coated by Ag Nps. Sample S₉ shows a low detection limit compared to the other two samples due to the higher surface area and lower Ag percentage, as mentioned previously.

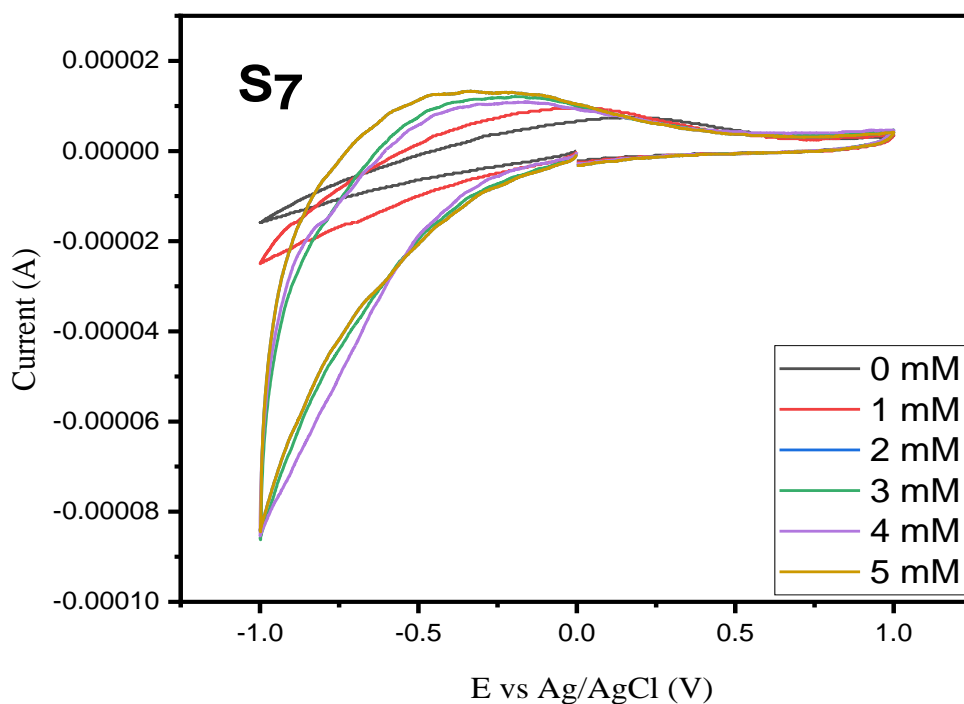


Figure 4-25a. Cyclic voltammograms of the ZnO NRs coated by Ag NPs in the presence of glucose in 0 mM- 5 mM in PBS with a scan rate of 50 mV s^{-1} of sample S₇.

Chapter 4: Results and discussion

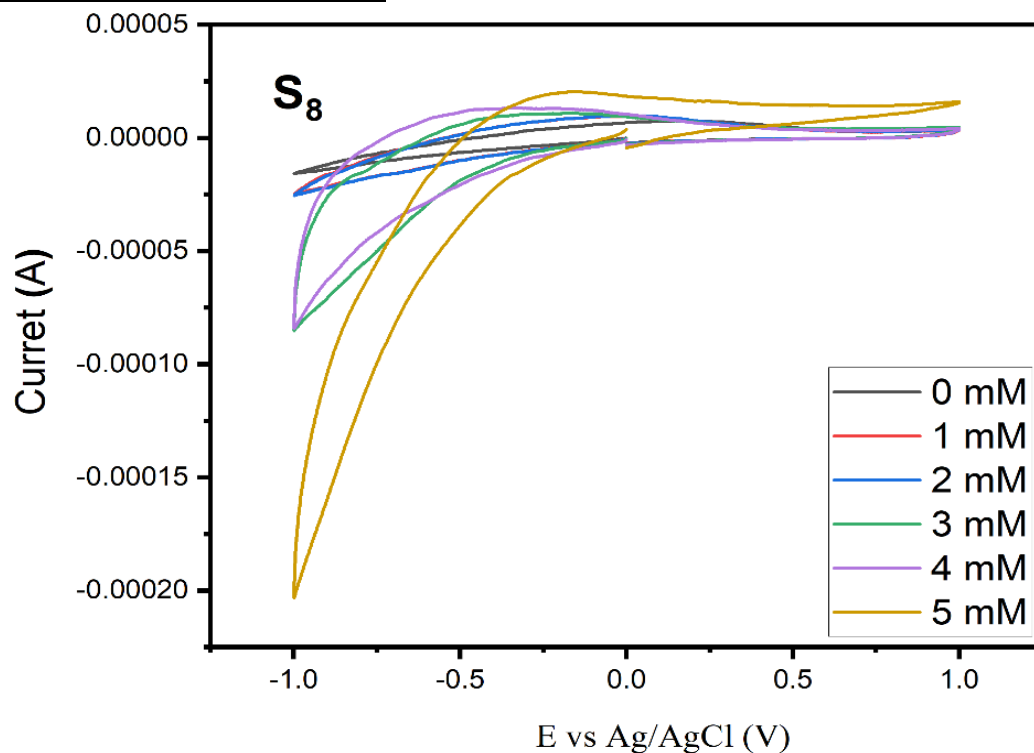


Figure 4-25b. Cyclic voltammograms of the ZnO NRs coated by Ag NPs in the presence of glucose of 0 mM- 5 mM in PBS with a scan rate of 50 mV s^{-1} of sample S₈.

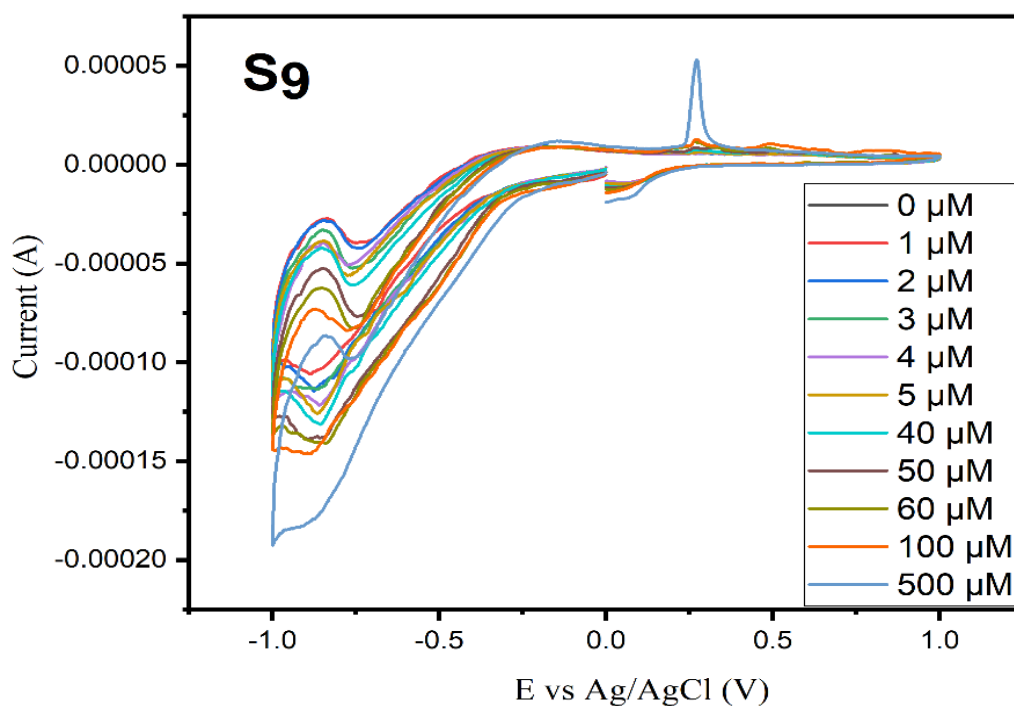


Figure 4-25c. Cyclic voltammograms of the ZnO NRs coated by Ag NPs in the presence of glucose of 0 μM- 500 μM PBS with a scan rate of 50 mV s^{-1} of sample S₉.

Chapter 4: Results and discussion

Figure 4-26 shows the relation between the increments of current as a function of glucose concentration. The calibration curve was plotted by the OriginLab program as illustrate in the figure 4-26. The optimum sample S_9 showed that the limit of detection (LOD), the sensitivity and the response time were $38.1 \mu\text{M}$, $350.1 \mu\text{A}\cdot\text{mM}^{-1}\cdot\text{cm}^2$ and 7 sec, respectively. These results summarized in table 4-8 indicated that the reaction improved and the detection limit decreased by increasing the thickness of the films and doping with Ag NPs. In addition, these results showed a detection limit less than that previously reported [135], and a sensitivity of higher than those reported elsewhere [136,137].

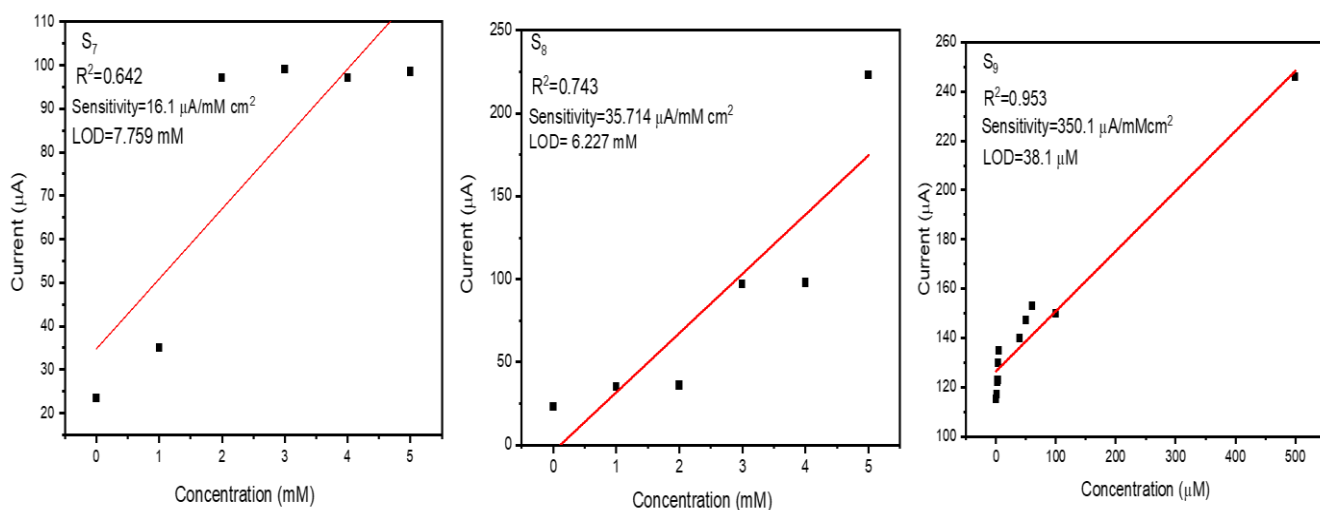


Figure 4-26. Increments of current as a function of glucose concentration of samples S_7 , S_8 , and S_9 .

Chapter 4: Results and discussion

Table 4-8 varying in data obtained from cyclic voltammetry data for S₄, S₅, S₆, S₇, S₈, and S₉.

Sample ID	R ² (from linearity)	Sensitivity $\mu\text{A}/\text{mMcm}^2$ (Eq.3-17)	LOD mM (Eq.3-18)
S ₄	0.213	9.814	15.933
S ₅	0.882	53.914	3.953
S ₆	0.682	16.51	7.14
S ₇	0.642	16.1	7.759
S ₈	0.743	35.714	6.227
S ₉	0.953	350.1	0.0381

4.6 Conclusion

Ag NPs were coated the ZnO NRs using the dip coating system to be used as glucose biosensor.

- 1- It was found that with the increase in the number of times of dipping, the thickness of the ZnO seed layer increased, as the surface became smoother and its electrical properties improved.
- 2- As for the optical properties, its transmittance decreased slightly with a decrease in the value of the energy gap. In contrast, ZnO NRs obtained a greater density and length due to the increase in the number of dipping times, in addition to an improvement in electrical properties, a decrease in transmittance and an improvement in the energy gap values, which gradually decreased. However, the voltammetric properties were not as good as the desired performance of the ZnO NRs.
- 3- When ZnO NRs were coated with Ag NPs, the optical properties improved by increasing the transmittance of the sample S₉, reducing the energy gap, increasing the electrode sensitivity and decreasing the detection limit.
- 4- The best sample is the S₉ sample due to the compatibility of the amount of Ag NPs 0.001 M with the proportion of ZnO, the improvement of electron transfer, and the improvement of its electrical properties and cyclic voltammetry, the results were matched with what was done. In addition, it is important for detection of glucose in biological systems. The manufactured electrode can be used as a glucose sensor in liquids containing human serum since the active medium is similar in its properties to human blood.

4.7 Future work

- 1- Study the effect of changing the concentration of zinc acetate solution from 0.1 M to 0.05 and 0.01 M to reduce the density of the nanorod to obtain a larger surface area.
- 2- Using spin coating method to deposit seed layer.
- 3- Converting ZnO NRs to ZnO NTs and studying the extent of their effect on the transfer of electrons and increasing the stabilization of GOx to increase the sensitivity of the prepared electrode.
- 4- Using Ag NPs at small ratio with zinc acetate concentration in the seed layer to investigate its effect on the resistance and electron transfer speed of the prepared electrode.
- 5- The use of Au NPs and Ag NPs (with the same concentration) with the zinc acetate in the seed layer to show its role in the formation of ZnO NRs and ZnO NTs and the extent of its impact on the stability of rods, diameter, and growth direction.

References

- [1] A. Ate, H. Zhu, H. Cai, X. Quan, X. Wang, X. Jia, J. Zhang, K. Wang, X. Jia, and Z. Tang, *High Performance UV Sensor Based on Individual ZnO Nanowire and Photoelectric Properties of Individual ZnO Nanowire Surface in Different Atmospheres*, in *AIP Conference Proceedings*, Vol. 1586 (2014), pp. 52–56.
- [2] R. Wang, *The Chemistry of Nanomaterials-CNR Rao, A. Müller, AK Cheetham (Eds)*, WILEY-VCH Verlag GmbH & Co. KGaA, Weinheim 2004. ISBN 3-527-30686-2, 741 Pages, *Colloid Polym Sci* **283**, 234 (2004).
- [3] I. P. Kaur, V. Kakkar, P. K. Deol, M. Yadav, M. Singh, and I. Sharma, *Issues and Concerns in Nanotech Product Development and Its Commercialization*, *J Control Release* **193**, 51 (2014).
- [4] P. Boisseau and B. Loubaton, *Nanomedicine, Nanotechnology in Medicine*, *Comptes Rendus Phys* **12**, 620 (2011).
- [5] A. P. Alivisatos, *Perspectives on the Physical Chemistry of Semiconductor Nanocrystals*, *J Phys Chem* **100**, 13226 (1996).
- [6] R. S. Rawat, *Dense Plasma Focus - From Alternative Fusion Source to Versatile High Energy Density Plasma Source for Plasma Nanotechnology*, *J Phys Conf Ser* **591**, 12021 (2015).
- [7] M. Swierczewska, G. Liu, S. Lee, and X. Chen, *High-Sensitivity Nanosensors for Biomarker Detection*, *Chem Soc Rev* **41**, 2641 (2012).
- [8] F. Santiago, K. Boulais, A. Rayms-Kelleran, V. H. Gehman Jr, K. J. Long, and H. Szu, *Nanomaterials for Sensor Applications*, in *Independent Component Analyses, Wavelets, Neural Networks, Biosystems, and Nanoengineering VII*, Vol. 7343 (2009), p. 73430P.
- [9] R. M. White, *A Sensor Classification Scheme*, *IEEE Trans Ultrason Ferroelectr Freq Control* **34**, 124 (1987).
- [10] S. Su, W. Wu, J. Gao, J. Lu, and C. Fan, *Nanomaterials-Based Sensors for Applications in Environmental Monitoring*, *J Mater Chem* **22**, 18101 (2012).
- [11] H. L. Chia, C. C. Mayorga-Martinez, and M. Pumera, *Doping and Decorating 2D Materials for Biosensing: Benefits and Drawbacks*, *Adv Funct Mater* **31**, 2102555 (2021).
- [12] A. Petersmann, D. Müller-Wieland, U. A. Müller, R. Landgraf, M. Nauck, G. Freckmann, L. Heinemann, and E. Schleicher, *Definition, Classification and Diagnosis of Diabetes Mellitus*, *Exp Clin Endocrinol & Diabetes* **127**, S1 (2019).
- [13] M. Karvonen, M. Pitkäniemi, J. Pitkäniemi, K. Kohtamäki, N. Tajima, and J. Tuomilehto, *Sex Difference in the Incidence of Insulin-Dependent Diabetes Mellitus: An Analysis of the Recent Epidemiological Data*, *Diabetes Metab Rev* **13**, 275 (1997).
- [14] N. Motahari-Tabari, M. A. Shirvani, M. Shirzad-e-Ahoodashty, E. Yousefi-Abdolmaleki, and M. Teimourzadeh, *The Effect of 8 Weeks Aerobic Exercise on Insulin Resistance in Type 2 Diabetes: A Randomized Clinical Trial*, *Glob J Health Sci* **7**, 115 (2015).

- [15] *Diabetes & Blood Sugar*, <https://www.howtorelief.com/diabetes-blood-sugar/>.
- [16] J. S. Wilson, *Sensor Technology Handbook* (Elsevier, 2004).
- [17] R. Ahmad, N. Tripathy, J. H. Kim, and Y.-B. Hahn, *Highly Selective Wide Linear-Range Detecting Glucose Biosensors Based on Aspect-Ratio Controlled ZnO Nanorods Directly Grown on Electrodes*, *Sensors Actuators B Chem* **174**, 195 (2012).
- [18] X. Feng, Y. Cheng, C. Ye, J. Ye, J. Peng, and J. Hu, *Synthesis and Ag-Content-Depended Electrochemical Properties of Ag/ZnO Heterostructured Nanomaterials*, *Mater Lett* **79**, 205 (2012).
- [19] A. Umar, M. S. Chauhan, S. Chauhan, R. Kumar, P. Sharma, K. J. Tomar, R. Wahab, A. Al-Hajry, and D. Singh, *Applications of ZnO Nanoflowers as Antimicrobial Agents for Escherichia Coli and Enzyme-Free Glucose Sensor*, *J Biomed Nanotechnol* **9**, 1794 (2013).
- [20] Y. Liu, H. Pang, C. Wei, M. Hao, S. Zheng, and M. Zheng, *Mesoporous ZnO-NiO Architectures for Use in a High-Performance Nonenzymatic Glucose Sensor*, *Microchim Acta* **181**, 1581 (2014).
- [21] R. Ahmad, N. Tripathy, and Y.-B. Hahn, *Highly Stable Urea Sensor Based on ZnO Nanorods Directly Grown on Ag/Glass Electrodes*, *Sensors Actuators B Chem* **194**, 290 (2014).
- [22] J. R. Anusha, A. T. Fleming, H.-J. Kim, B. C. Kim, K.-H. Yu, and C. J. Raj, *Effective Immobilization of Glucose Oxidase on Chitosan Submicron Particles from Gladius of Todarodes Pacificus for Glucose Sensing*, *Bioelectrochemistry* **104**, 44 (2015).
- [23] A. A. Ibrahim, A. Umar, R. Ahmad, R. Kumar, and S. Baskoutas, *Fabrication and Characterization of Highly Sensitive and Selective Glucose Biosensor Based on ZnO Decorated Carbon Nanotubes*, *Nanosci Nanotechnol Lett* **8**, 853 (2016).
- [24] J. Li, M. Lu, Z. Tan, Y. Xu, Y. Zhang, X. Hu, and Z. Yang, *One-Step Solvothermal Preparation of Silver-ZnO Hybrid Nanorods for Use in Enzymatic and Direct Electron-Transfer Based Biosensing of Glucose*, *Microchim Acta* **183**, 1705 (2016).
- [25] N. Muthuchamy, R. Atchudan, T. N. J. I. Edison, S. Perumal, and Y. R. Lee, *High-Performance Glucose Biosensor Based on Green Synthesized Zinc Oxide Nanoparticle Embedded Nitrogen-Doped Carbon Sheet*, *J Electroanal Chem* **816**, 195 (2018).
- [26] X. F. Hoo, K. Abdul Razak, N. S. Ridhuan, N. Mohamad Nor, and N. D. Zakaria, *Electrochemical Glucose Biosensor Based on ZnO Nanorods Modified with Gold Nanoparticles*, *J Mater Sci Mater Electron* 2019 308 **30**, 7460 (2019).
- [27] V. Myndrul, I. Iatsunskyi, N. Babayevska, M. Jarek, and T. Jesionowski, *Effect of Electrode Modification with Chitosan and Nafion® on the Efficiency of Real-Time Enzyme Glucose Biosensors Based on ZnO Tetrapods*, *Materials (Basel)* **15**, 4672 (2022).
- [28] P. Jood, R. J. Mehta, Y. L. Zhang, G. Peleckis, X. L. Wang, and R. W. Siegel, *TB-Tasciuc, SX Dou, and G. Ramanath*, *Nano Lett* **11**, 4337 (2011).
- [29] J. Bardeen and W. H. Brattain, *The Transistor, a Semi-Conductor Triode*, *Phys Rev* **74**, 230

- (1948).
- [30] A. R. Hutson, *Piezoelectricity and Conductivity in ZnO and CdS*, Phys Rev Lett **4**, 505 (1960).
- [31] F. S. Hickernell, *Zinc-Oxide Thin-Film Surface-Wave Transducers*, Proc IEEE **64**, 631 (1976).
- [32] K. Nomura, H. Ohta, K. Ueda, T. Kamiya, M. Hirano, and H. Hosono, *Thin-Film Transistor Fabricated in Single-Crystalline Transparent Oxide Semiconductor*, Science (80-) **300**, 1269 (2003).
- [33] S. Chaudhary, A. Umar, K. K. Bhasin, and S. Baskoutas, *Chemical Sensing Applications of ZnO Nanomaterials*, Materials (Basel) **11**, 287 (2018).
- [34] G. Murtaza, R. Ahmad, M. S. Rashid, M. Hassan, A. Hussnain, M. A. Khan, M. E. ul Haq, M. A. Shafique, and S. Riaz, *Structural and Magnetic Studies on Zr Doped ZnO Diluted Magnetic Semiconductor*, Curr Appl Phys **14**, 176 (2014).
- [35] S. Logothetidis, A. Laskarakis, S. Kassavetis, S. Lousinian, C. Gravalidis, and G. Kiriakidis, *Optical and Structural Properties of ZnO for Transparent Electronics*, Thin Solid Films **516**, 1345 (2008).
- [36] W. Xie, Z. Yang, and H. Chun, *Catalytic Properties of Lithium-Doped ZnO Catalysts Used for Biodiesel Preparations*, Ind & Eng Chem Res **46**, 7942 (2007).
- [37] M. Law, L. E. Greene, J. C. Johnson, R. Saykally, and P. Yang, *Nanowire Dye-Sensitized Solar Cells*, Nat Mater **4**, 455 (2005).
- [38] M. Willander Magnus and Nur, O and Zhao, QX and Yang, LL and Lorenz, M and Cao, BQ and P{\e}rez, J Z{\u}{\~n}iga and Czekalla, C and Zimmermann, G and Grundmann, M and others},, *Zinc Oxide Nanorod Based Photonic Devices: Recent Progress in Growth, Light Emitting Diodes and Lasers*, Nanotechnology **20**, 332001 (2009).
- [39] Ü. Özgür, Y. I. Alivov, C. Liu, A. Teke, Ma. Reshchikov, S. Doğan, V. Avrutin, S.-J. Cho, Morkoç, and H. %J J. of applied Physics, *A Comprehensive Review of ZnO Materials and Devices*, **98**, 11 (2005).
- [40] H. Morkoç and Ü. Özgür, *Zinc Oxide: Fundamentals, Materials and Device Technology* (John Wiley & Sons, 2008).
- [41] A. Ashrafi and C. Jagadish, *Review of Zincblende ZnO: Stability of Metastable ZnO Phases*, J Appl Phys **102**, 4 (2007).
- [42] P. Espitia, N. Soares, J. Coimbra, N. Andrade, R. Cruz, and E. Medeiros, *Zinc Oxide Nanoparticles: Synthesis, Antimicrobial Activity and Food Packaging Applications*, Food Bioprocess Technol **5**, (2012).
- [43] S. Hussain, *Investigation of Structural and Optical Properties of Nanocrystalline ZnO*.
- [44] X. Wang, J. Song, J. Liu, and Z. L. Wang, *Direct-Current Nanogenerator Driven by Ultrasonic Waves*, Science (80-) **316**, 102 (2007).

- [45] A. B. Djurišić, A. M. C. Ng, and X. Y. Chen, *ZnO Nanostructures for Optoelectronics: Material Properties and Device Applications*, Prog Quantum Electron **34**, 191 (2010).
- [46] Z. Li and W. Gao, *ZnO Thin Films with DC and RF Reactive Sputtering*, Mater Lett **58**, 1363 (2004).
- [47] J.-H. Lee, B.-W. Yeo, and B.-O. Park, *Effects of the Annealing Treatment on Electrical and Optical Properties of ZnO Transparent Conduction Films by Ultrasonic Spraying Pyrolysis*, Thin Solid Films **457**, 333 (2004).
- [48] H. Kashani, *Structural, Electrical and Optical Properties of Zinc Oxide Produced by Oxidation of Zinc Thin Films*, J Electron Mater **27**, 876 (1998).
- [49] P. Souletie, S. Bethke, B. W. Wessels, and H. Pan, *Growth and Characterization of Heteroepitaxial ZnO Thin Films by Organometallic Chemical Vapor Deposition*, J Cryst Growth **86**, 248 (1988).
- [50] K. L. Choy, *Chemical Vapour Deposition of Coatings*, Prog Mater Sci **48**, 57 (2003).
- [51] J. O. Williams, *Metal Organic Chemical Vapor Deposition (MOCVD) Perspectives and Prospects*, Angew Chemie Int Ed English **28**, 1110 (1989).
- [52] M. C. Vasudev, K. D. Anderson, T. J. Bunning, V. V Tsukruk, and R. R. Naik, *Exploration of Plasma-Enhanced Chemical Vapor Deposition as a Method for Thin-Film Fabrication with Biological Applications*, ACS Appl Mater Interfaces **5**, 3983 (2013).
- [53] J. Musil, *Low-Pressure Magnetron Sputtering*, Vacuum **50**, 363 (1998).
- [54] S.-H. Yi, S.-K. Choi, J.-M. Jang, J.-A. Kim, and W.-G. Jung, *Low-Temperature Growth of ZnO Nanorods by Chemical Bath Deposition*, J Colloid Interface Sci **313**, 705 (2007).
- [55] M. Vafaei and M. S. Ghamsari, *Preparation and Characterization of ZnO Nanoparticles by a Novel Sol-Gel Route*, Mater Lett **61**, 3265 (2007).
- [56] J. Cui, *Zinc Oxide Nanowires*, Mater Charact **64**, 43 (2012).
- [57] S. J. Ling, Samuel J and Sanny, Jeff and Moebis, William and Friedman, Gerald and Druger, Stephen D and Kolakowska, Alice and Anderson, David and Bowman, Daniel and Demaree, Dedra and Ginsberg, Edw., *University Physics Volume 2*, (2016).
- [58] J. Oh, G. Yoo, Y. W. Chang, H. J. Kim, J. Jose, E. Kim, J.-C. Pyun, and K.-H. Yoo, *A Carbon Nanotube Metal Semiconductor Field Effect Transistor-Based Biosensor for Detection of Amyloid-Beta in Human Serum*, Biosens Bioelectron **50**, 345 (2013).
- [59] S. S. Patil Patil, Santosh S and Mali, Mukund G and Tamboli, Mohaseen S and Patil, Deepak R and Kulkarni, Milind V and Yoon, Hyun and Kim, Hayong and Al-Deyab, Salem S and Yoon, Sam S and Kolekar, Sanjay S., *Green Approach for Hierarchical Nanostructured Ag-ZnO and Their Photocatalytic Performance under Sunlight*, Catal Today **260**, 126 (2016).
- [60] Y. Zheng, L. Zheng, Y. Zhan, X. Lin, Q. Zheng, and K. Wei, *Ag/ZnO Heterostructure Nanocrystals: Synthesis, Characterization, and Photocatalysis*, Inorg Chem **46**, 6980 (2007).

- [61] Q. Mao, W. Jing, W. Gao, Z. Wei, B. Tian, M. Liu, W. Ren, and Z. Jiang, *High-Sensitivity Enzymatic Glucose Sensor Based on ZnO Urchin-like Nanostructure Modified with Fe₃O₄ Magnetic Particles*, *Micromachines* **12**, 977 (2021).
- [62] M.-H. Hsu and C.-J. Chang, *Ag-Doped ZnO Nanorods Coated Metal Wire Meshes as Hierarchical Photocatalysts with High Visible-Light Driven Photoactivity and Photostability*, *J Hazard Mater* **278**, 444 (2014).
- [63] Z. Q. Xu, H. Deng, Y. Li, Q. H. Guo, and Y. R. Li, *Characteristics of Al-Doped c-Axis Orientation ZnO Thin Films Prepared by the Sol--Gel Method*, *Mater Res Bull* **41**, 354 (2006).
- [64] Y. Yan, M. M. Al-Jassim, and S.-H. Wei, *Doping of ZnO by Group-IB Elements*, *Appl Phys Lett* **89**, 181912 (2006).
- [65] R. Deng, Y. Zou, and H. Tang, *Correlation between Electrical, Optical Properties and Ag₂⁺ Centers of ZnO: Ag Thin Films*, *Phys B Condens Matter* **403**, 2004 (2008).
- [66] J. N. Helbert, *Handbook of VLSI Microlithography* (Cambridge University Press, 2001).
- [67] D. Perednis, *Thin Film Deposition by Spray Pyrolysis and the Application in Solid Oxide Fuel Cells*, ETH Zurich, 2003.
- [68] D. Pissuwan, S. M. Valenzuela, and M. B. Cortie, *Therapeutic Possibilities of Plasmonically Heated Gold Nanoparticles*, *TRENDS Biotechnol* **24**, 62 (2006).
- [69] Y. Wang, Z. Tang, and N. A. Kotov, *Bioapplication of Nanosemiconductors*, *Mater Today* **8**, 20 (2005).
- [70] Z. L. Wang, *ZnO Nanowire and Nanobelt Platform for Nanotechnology*, *Mater Sci Eng R Reports* **64**, 33 (2009).
- [71] D. Lončarević and Ž. Čupić, *Chapter 4 - The Perspective of Using Nanocatalysts in the Environmental Requirements and Energy Needs of Industry*, in *Industrial Applications of Nanomaterials*, edited by S. Thomas, Y. Grohens, and Y. B. Pottathara (Elsevier, 2019), pp. 91–122.
- [72] M. Maleki, M. Reyssat, F. Restagno, D. Quéré, and C. Clanet, *Landau--Levich Menisci*, *J Colloid Interface Sci* **354**, 359 (2011).
- [73] Y. Tong, S. Bohm, M. Song, and others, *Graphene Based Materials and Their Composites as Coatings*, *Austin J Nanomedicine & Nanotechnol* **1**, 1003 (2013).
- [74] D. Wang and G. P. Bierwagen, *Sol--Gel Coatings on Metals for Corrosion Protection*, *Prog Org Coatings* **64**, 327 (2009).
- [75] M. L. Zheludkevich, I. M. Salvado, and M. G. S. Ferreira, *Sol--Gel Coatings for Corrosion Protection of Metals*, *J Mater Chem* **15**, 5099 (2005).
- [76] N. S. Ramgir, Y. Yang, and M. Zacharias, *Nanowire-Based Sensors*, *Small* **6**, 1705 (2010).
- [77] B. G. Svensson, S. Pearton, and C. Jagadish, *Oxide Semiconductors* (Academic Press, 2013).

- [78] J. E. Stehr, S. L. Chen, S. Filippov, M. Devika, N. K. Reddy, C. W. Tu, W. M. Chen, and I. A. Buyanova, *Defect Properties of ZnO Nanowires Revealed from an Optically Detected Magnetic Resonance Study*, *Nanotechnology* **24**, 15701 (2012).
- [79] E. G. Assefa, *Sol-Gel Method Synthesis and Characterization of Mn Doped ZnO Semiconductor Nanostructures for Optoelectronic Devices*, ASTU, 2017.
- [80] C. Liu, F. Yun, and H. Morkoc, *Ferromagnetism of ZnO and GaN: A Review*, *J Mater Sci Mater Electron* **16**, 555 (2005).
- [81] R. P. Singh, J. W. Choi, and A. C. Pandey, *Smart Nanomaterials for Biosensors, Biochips and Molecular Bioelectronics*, *Smart Nanomater Sens Appl Bentham Sci Publ* **3** (2012).
- [82] J. Wang, *Nanomaterial-Based Electrochemical Biosensors*, *Analyst* **130**, 421 (2005).
- [83] N. Kouklin, *Cu-Doped ZnO Nanowires for Efficient and Multispectral Photodetection Applications*, *Adv Mater* **20**, 2190 (2008).
- [84] C.-H. Jin, S.-H. Park, H.-S. Kim, S.-Y. An, and C.-M. Lee, *CO Gas-Sensor Based on Pt-Functionalized Mg-Doped ZnO Nanowires*, *Bull Korean Chem Soc* **33**, 1993 (2012).
- [85] Q. Wan, Q. H. Li, Y. J. Chen, T. H. Wang, X. L. He, X. G. Gao, and J. P. Li, *Positive Temperature Coefficient Resistance and Humidity Sensing Properties of Cd-Doped ZnO Nanowires*, *Appl Phys Lett* **84**, 3085 (2004).
- [86] Y. Yang, W. Guo, J. Qi, and Y. Zhang, *Flexible Piezoresistive Strain Sensor Based on Single Sb-Doped ZnO Nanobelts*, *Appl Phys Lett* **97**, 223107 (2010).
- [87] L. C. Clark Jr, *Monitor and Control of Blood and Tissue Oxygen Tensions*, *Asaio J* **2**, 41 (1956).
- [88] L. C. Clark Jr and C. %J A. of the N. Y. A. of sciences Lyons, *Electrode Systems for Continuous Monitoring in Cardiovascular Surgery*, **102**, 29 (1962).
- [89] S. J. Updike and G. P. Hicks, *The Enzyme Electrode*, *Nature* **214**, 986 (1967).
- [90] S. Rodriguez-Mozaz, M. J. de Alda, and D. Barceló, *Biosensors as Useful Tools for Environmental Analysis and Monitoring*, *Anal Bioanal Chem* **386**, 1025 (2006).
- [91] S. K. Arya, S. Saha, J. E. Ramirez-Vick, V. Gupta, S. Bhansali, and S. P. Singh, *Recent Advances in ZnO Nanostructures and Thin Films for Biosensor Applications*, *Anal Chim Acta* **737**, 1 (2012).
- [92] P. A. Serra, *Biosensors* (BoD--Books on Demand, 2010).
- [93] M. A. Arnold and M. E. %J C. R. in A. C. Meyerhoff, *Recent Advances in the Development and Analytical Applications of Biosensing Probes*, **20**, 149 (1988).
- [94] D. Grieshaber, R. MacKenzie, J. Vörös, and E. Reimhult, *Electrochemical Biosensors - Sensor Principles and Architectures*, *Sensors* **8**, 1400 (2008).
- [95] G. Kovács and I. Popescu, PhD Thesis - Amperometric Biosensors for Detection of Analytes of Biotechnological Interest, 2012.

- [96] D. Wang, R. Kou, M. P. Gil, H. P. Jakobson, J. Tang, D. Yu, Y. %J J. of nanoscience Lu, and Nanotechnology, *Templated Synthesis, Characterization, and Sensing Application of Macroscopic Platinum Nanowire Network Electrodes*, **5**, 1904 (2005).
- [97] J. Wang, *Glucose Biosensors: 40 Years of Advances and Challenges*, *Electroanal An Int J Devoted to Fundam Pract Asp Electroanal* **13**, 983 (2001).
- [98] C. Chen, X.-L. Zhao, Z.-H. Li, Z.-G. Zhu, S.-H. Qian, and A. J. Flewitt, *Current and Emerging Technology for Continuous Glucose Monitoring*, *Sensors* **17**, 182 (2017).
- [99] D. C. Klonoff, *The Benefits of Implanted Glucose Sensors*, *Journal of Diabetes Science and Technology*.
- [100] L. R. F. Allen and J. Bard, *Electrochemical Methods Fundamental and Applications.*, John Wiley & Sons, Inc, United State Am (2001).
- [101] W. Schuhmann, *Amperometric Enzyme Biosensors Based on Optimised Electron-Transfer Pathways and Non-Manual Immobilisation Procedures*, *Rev Mol Biotechnol* **82**, 425 (2002).
- [102] S. Borgmann, A. Schulte, S. Neugebauer, and W. Schuhmann, *Advances in Electrochemical Science and Engineering*, WILEY-VCH Verlag GmbH & Co KGaA, Weinheim 32885 (2011).
- [103] T. Bailey, B. W. Bode, M. P. Christiansen, L. J. Klaff, and S. Alva, *The Performance and Usability of a Factory-Calibrated Flash Glucose Monitoring System*, *Diabetes Technol & Ther* **17**, 787 (2015).
- [104] F. C. Krebs, H. Spanggard, T. Kjær, M. Biancardo, and J. Alstrup, *Large Area Plastic Solar Cell Modules*, *Mater Sci Eng B* **138**, 106 (2007).
- [105] D. A. Castillo-Vilcatomaa, S. J. Loarte, A. A. Fernandez-Chillcea, E. C. Pastranab, and R. Y. Pastranaa, *DESIGNING AND FABRICATION OF A LOW-COST DIP-COATER FOR RAPID PRODUCTION OF UNIFORM THIN FILMS*, (n.d.).
- [106] Y. Yohandri, K. Khairunnisa, R. Ramli, and R. Zainul, *Development of a Digital Dip Coating System Based Microcontroller*, *Eksakta Berk Ilm Bid MIPA (E-ISSN 2549-7464)* **20**, 62 (2019).
- [107] M. Willander, L. L. Yang, A. Wadeasa, S. U. Ali, M. H. Asif, Q. X. Zhao, and O. Nur, *Zinc Oxide Nanowires: Controlled Low Temperature Growth and Some Electrochemical and Optical Nano-Devices*, *J Mater Chem* **19**, 1006 (2009).
- [108] U. Holzwarth and N. Gibson, *The Scherrer Equation versus the 'Debye-Scherrer Equation'*, *Nat Nanotechnol* **6**, 534 (2011).
- [109] A. Samavati, A. Awang, Z. Samavati, A. F. Ismail, M. H. D. Othman, M. Velashjerdi, A. Rostami, and others, *Influence of ZnO Nanostructure Configuration on Tailoring the Optical Bandgap: Theory and Experiment*, *Mater Sci Eng B* **263**, 114811 (2021).
- [110] R. Das, E. Ali, and S. B. Abd Hamid, *CURRENT APPLICATIONS OF X-RAY POWDER DIFFRACTION-A REVIEW.*, *Rev Adv Mater Sci* **38**, (2014).

- [111] W. Zhou and Z. L. Wang, *Scanning Microscopy for Nanotechnology: Techniques and Applications* (Springer science & business media, 2007).
- [112] Z. Chen, Zhebo and Dinh, Huyen N and Miller, Eric., *UV-Vis Spectroscopy, in Photoelectrochemical Water Splitting* (Springer, 2013), pp. 49–62.
- [113] A. Höpe, *Chapter 6 - Diffuse Reflectance and Transmittance*, in *Spectrophotometry*, edited by T. A. Germer, J. C. Zwinkels, and B. K. Tsai, Vol. 46 (Academic Press, 2014), pp. 179–219.
- [114] N. Shakti and P. S. Gupta, *Structural and Optical Properties of Sol-Gel Prepared ZnO Thin Film*, *Appl Phys Res* **2**, 19 (2010).
- [115] P. Sharma, K. Sreenivas, and K. V Rao, *Analysis of Ultraviolet Photoconductivity in ZnO Films Prepared by Unbalanced Magnetron Sputtering*, *J Appl Phys* **93**, 3963 (2003).
- [116] A. Uhler Jr, *The Potentials of Infinite Systems of Sources and Numerical Solutions of Problems in Semiconductor Engineering*, *Bell Syst Tech J* **34**, 105 (1955).
- [117] C.-S. Seok, B. K. Bae, and J.-M. Koo, *DC Potential Drop Method for Evaluating Material Degradation*, *KSME Int J* **18**, 1368 (2004).
- [118] D. A. Bernards, D. J. Macaya, M. Nikolou, J. A. DeFranco, S. Takamatsu, and G. G. Malliaras, *Enzymatic Sensing with Organic Electrochemical Transistors*, *J Mater Chem* **18**, 116 (2008).
- [119] K. Khun, Z. H. Ibupoto, J. Lu, M. S. AlSalhi, M. Atif, A. A. Ansari, and M. Willander, *Potentiometric Glucose Sensor Based on the Glucose Oxidase Immobilized Iron Ferrite Magnetic Particle/Chitosan Composite Modified Gold Coated Glass Electrode*, *Sensors Actuators B Chem* **173**, 698 (2012).
- [120] A. Amine, H. Mohammadi, I. Bourais, and G. Palleschi, *Enzyme Inhibition-Based Biosensors for Food Safety and Environmental Monitoring*, *Biosens Bioelectron* **21**, 1405 (2006).
- [121] G. L. Turdean, *Design and Development of Biosensors for the Detection of Heavy Metal Toxicity*, *Int J Electrochem* **2011**, (2011).
- [122] J. Shi, J. C. Claussen, E. S. McLamore, A. ul Haque, D. Jaroch, A. R. Diggs, P. Calvo-Marzal, J. L. Rickus, and D. M. Porterfield, *A Comparative Study of Enzyme Immobilization Strategies for Multi-Walled Carbon Nanotube Glucose Biosensors*, *Nanotechnology* **22**, 355502 (2011).
- [123] A. Shrivastava, V. B. Gupta, and others, *Methods for the Determination of Limit of Detection and Limit of Quantitation of the Analytical Methods*, *Chron Young Sci* **2**, 21 (2011).
- [124] H. B. A. Kadhim, N. J. Ridha, F. K. M. Alosfur, N. M. Umran, R. Madlol, K. J. Tahir, and R. T. Ahmed, *Ablation of ZnO in Liquid by Nanosecond Laser*, in *Journal of Physics: Conference Series*, Vol. 1032 (2018), p. 12039.
- [125] N. J. Ridha, F. K. M. Alosfur, H. B. A. Kadhim, L. H. Aboud, and N. Al-Dahan, *Novel*

Method to Synthesis ZnO Nanostructures via Irradiation Zinc Acetate with a Nanosecond Laser for Photocatalytic Applications, J Mater Sci Mater Electron **31**, 9835 (2020).

- [126] N. J. Ridha, A. A. Umar, F. Alosfur, M. H. H. Jumali, and M. M. Salleh, *Microwave Assisted Hydrothermal Method for Porous Zinc Oxide Nanostructured-Films*, J Nanosci Nanotechnol **13**, 2667 (2013).
- [127] K. J. Chen, T. H. Fang, F. Y. Hung, L. W. Ji, S. J. Chang, S. J. Young, and Y. J. Hsiao, *The Crystallization and Physical Properties of Al-Doped ZnO Nanoparticles*, Appl Surf Sci **254**, 5791 (2008).
- [128] K. Farmer, P. Hari, and K. Roberts, *PH Study of Zinc Oxide Nanorods Grown on Indium Tin Oxide Coated Substrate*, Can J Phys **92**, 838 (2014).
- [129] S. Pokai, P. Limnonthakul, M. Horprathum, P. Eiamchai, V. Pattantsetakul, S. Limwichean, N. Nuntawong, S. Porntheeraphat, and C. Chitichotpanya, *Influence of Seed Layer Thickness on Well-Aligned ZnO Nanorods via Hydrothermal Method*, Mater Today Proc **4**, 6336 (2017).
- [130] E. Muchuweni, T. S. Sathiaraj, and H. Nyakoty, *Effect of Annealing on the Microstructural, Optical and Electrical Properties of ZnO Nanowires by Hydrothermal Synthesis for Transparent Electrode Fabrication*, Mater Sci Eng B **227**, 68 (2018).
- [131] J. Yi, J. M. Lee, and W. Il Park, *Vertically Aligned ZnO Nanorods and Graphene Hybrid Architectures for High-Sensitive Flexible Gas Sensors*, Sensors Actuators B Chem **155**, 264 (2011).
- [132] S. Aly and A. A. Akl, *INFLUENCE OF FILM THICKNESS ON OPTICAL ABSORPTION AND ENERGY GAP OF THERMALLY EVAPORATED CdS 0.1 Se...*, Chalcogenide Lett **12**, 489 (2015).
- [133] A. F. Abdulrahman, S. M. Ahmed, N. M. Ahmed, and M. A. Almessiere, *Enhancement of ZnO Nanorods Properties Using Modified Chemical Bath Deposition Method: Effect of Precursor Concentration*, Crystals **10**, 386 (2020).
- [134] N. Lavanya, C. Sekar, S. Ficarra, E. Tellone, A. Bonavita, S. G. Leonardi, and G. Neri, *A Novel Disposable Electrochemical Sensor for Determination of Carbamazepine Based on Fe Doped SnO₂ Nanoparticles Modified Screen-Printed Carbon Electrode*, Mater Sci Eng C **62**, 53 (2016).
- [135] V. Fidal, S. Inguva, S. Krishnamurthy, E. Marsili, J.-P. Mosnier, and T. S. Chandra, *Mediator-Free Interaction of Glucose Oxidase, as Model Enzyme for Immobilization, with Al-Doped and Undoped ZnO Thin Films Laser-Deposited on Polycarbonate Supports*, Enzyme Microb Technol **96**, 67 (2017).
- [136] X. Chu, X. Zhu, Y. Dong, T. Chen, M. Ye, and W. Sun, *An Amperometric Glucose Biosensor Based on the Immobilization of Glucose Oxidase on the Platinum Electrode Modified with NiO Doped ZnO Nanorods*, J Electroanal Chem **676**, 20 (2012).
- [137] Z. W. Zhao, X. J. Chen, B. K. Tay, J. S. Chen, Z. J. Han, and K. A. Khor, *A Novel Amperometric Biosensor Based on ZnO: Co Nanoclusters for Biosensing Glucose*, Biosens Bioelectron **23**, 135 (2007).

الخلاصة

تحولت العلوم البحثية والجمعيات الطبية مؤخرًا إلى استخدام أجهزة استشعار حيوية فعالة من حيث التكلفة لاختبار ملوثات الطعام والمياه ، والتحكم في العمليات البيولوجية البشرية ، وتقييم التشخيص الصحي الدقيق ، والمزيد. يحتاج الباحثون والممارسون الطبيون إلى وسائل آمنة وأرخص تكلفة لإجراء أبحاثهم ، وضمان السلامة العامة ، وتقديم خيارات صحية مخصصة للمرضى. يمكن تنفيذ أحد هذه الحلول بسهولة باستخدام أجهزة الاستشعار الحيوية. تم تطوير نظام الطلاء بالغمر لتحضير الاغشية الرقيقة لأكسيد الزنك التي تم ترسيبها بنجاح على ركيزة اوكسيد القصدير الانديوم (ITO). تم دراسة تأثير عدد مرات الغمر، مرة الى ثلاث مرات بتركيز 0.1 مولار من خلاات الزنك لحصول على غشاء رقيق متجانس. في هذا العمل قضبان اوكسيد الزنك النانوية حضرت بالطريقة المائية الحرارية و تم طلاؤها بجسيمات الفضة النانوية لاستخدامها كمستشعر حيوي للسكر. تتضمن طريقة التحضير ثلاث خطوات، البذور، التنمية، والطلاء. الخطوة الاولى هي طلاء الركيزة بطبقة البذور. الخطوة الثانية هي تنمية قضبان اوكسيد الزنك النانوية باستخدام نترات الزنك بتركيز 0.050 مولار. اخيرا طلاء قضبان اوكسيد الزنك النانوية بطبقة من جسيمات الفضة النانوية باستخدام نترات الفضة بتركيز 0.001 مولار. تم اجراء الفحوصات التركيبية ومورفولوجيا السطح والبصرية والمقاومة الكهربائية وخواص الجهد الدوري لدراسة تأثير الطلاء بجسيمات الفضة النانوية على هذه العينات. كذلك معرفة الخواص التحفيزية لانزيم الجلوكوز (GOx) ووظيفة مستشعر الجلوكوز. اظهرت فحوصات حيود الاشعة السينية بان العينات المحضرة لها تركيب بلوري جيد سداسي اوكسيد الزنك wurtzite ونقاوة عالية. ان حجم البلورات لهذا الغشاء الرقيق بمدى 20 – 50 نانومتر. اما بالنسبة الى فحوصات FESEM وجد تشكل تطبيقات متجانسة عند زيادة عدد مرات الطلاء للغشاء المحضر. بينت الفحوصات البصرية والكهربائية ان الغشاء الرقيق المحضر له شفافية جيدة بحدود 60 – 87 % حسب نوع التركيب البلوري للغشاء المحضر مع انخفاض في قيمة فجوة الطاقة والمقاومة السطحية بزيادة السمك والطلاء بجسيمات الفضة النانوية. اظهرت النتائج ان خواص الجهد الدوري تحسنت عند الطلاء بجسيمات الفضة النانوية بتركيز 0.001 مولاري للعيينة S₉. كان معد المسح 50 ملي فولت \ ثا ومدى الفولتية من (-1) فولت – (1) فولت وتركيز الجلوكوز من 0 مولار - 500 مايكرو مولار. تحسنت نتائج فحوصات الجهد الدوري عند انخفاض تركيز الطلاء بالتدرج للعينات (S₇, S₈, and S₉) وكانت العينة الافضل هي العينة S₉، لان حساسيتها $350 \mu A \text{ mM}^{-1} \text{ cm}^{-2}$ وحده الكشف 38.1 mM وزمن الاستجابة 7 ثانية. وكانت الزيادة خطية للتيار المقاس عند تغير التراكيز للجلوكوز.



جامعة كربلاء

كلية العلوم

قسم الفيزياء

تصنيع المتحسس الحيوي للسكر باستخدام تركيب اوكسيد الزنك النانوية

المطلي بجسيمات الفضة النانوية

رسالة

مقدمة الى مجلس كلية العلوم / جامعة كربلاء

كجزء من متطلبات نيل درجة الماجستير في علوم الفيزياء

من قبل

اسعد صبار ياسر

باشراف

أ.د. نور جواد رضا